Behaviour of radiation detectors in various field sizes

Sakhile P. T. Msibi

925312

Research report in partial fulfilment of an MSc in Physics by coursework

and research report in the field of Medical Physics

School of Physics
University of the Witwatersrand

2020

DECLARATION

I declare that this research report is my unaided work. It is being submitted for the Degree of Master of Science at the University of the Witwatersrand, Johannesburg. It has not been submitted before for any degree or examination at any other Tertiary Institution.

....

Student's Name Signature of a student

Date: ....

ABSTRACT

Firstly, this study investigates the effect of the detector orientation and the detector sensitive volume size on the response of a detector in various radiation beam field sizes. Secondly, to investigates whether results should be reported in geometric field sizes or irradiation field sizes. Finally, to investigates which detector is suitable for small field dosimetry.

A PTW 30013 Farmer ionisation chamber, a PTW 31010 semi-flex ionisation chamber and a PTW 60019 synthetic single-crystal diamond detector were irradiated with a 6 MV photon beam, produced by a Siemens Oncor linear accelerator and an Elekta Versa HD linear accelerator, in various field sizes from 0.6 cm x 0.6 cm to 25 cm x 25 cm. These detectors were oriented parallel to the beam and perpendicular to the beam. Current was collected to investigate the effect of the detector orientation and the detector sensitive volume size in the central region of a beam profile and the penumbra region of a beam profile. Charges were collected to calculate tissue phantom ratios, ranges of charged particles and output factors.

Firstly, the results indicate that the Siemens Oncor linear accelerator and the Elekta Versa HD linear accelerator used in this study have different beam qualities. The results indicate that the ranges of charged particles are dependent on the beam quality of the radiation beam. The results show that the ranges of charged particles obtained using the Siemens Oncor linear accelerator and the Elekta Versa HD linear accelerator were 0.4 cm and 1.3 cm, respectively. Secondly, the results show that the beam profiles and percentage depth doses are dependent on radiation beam field sizes. The output factors are dependent on radiation beam field sizes that are less than 6 cm x 6 cm. Thirdly, beam profiles show that there is strong detector response dependency on detector orientation in beam field sizes that are less than 6 cm x 6 cm obtained using the Siemens Oncor linear accelerator. There is strong detector response dependency on detector orientation in beam field sizes that are less than 4 cm x 4 cm obtained using the Elekta Versa HD linear accelerator. Finally, the results indicate that there is difference between the calculated irradiation field sizes and geometric field sizes, however there is no discernible difference in reporting results in geometric field sizes or irradiation field sizes.

The study concludes that a PTW 30013 Farmer ionisation chamber and a PTW 31010 semi-flex ionisation chamber are not suitable to be used in dosimetry using a Siemens Oncor linear accelerator. The PTW 30013 Farmer ionisation chamber is not suitable to be used in small field dosimetry in an Elekta Versa HD linear accelerator. The study recommends that beam quality of a linear accelerator should be determined to check which detector is suitable to be used in small field dosimetry. This study also recommends that Medical Physicist should use a PTW 60019 synthetic single-crystal diamond detector for dosimetry.

To my son, Thando, for your patience with your farther who seemed to always be working on the research report and to everyone else who supported me throughout my studies.

ACKNOWLEDGEMENTS

I would like to thank the Charlotte Maxeke Johannesburg Academic Hospital for allowing me to use their facilities. Furthermore, I would like to thank Lazola, Sonwabile, Nkosi, Eddie, Thulani and Lehlabile for assisted me in collecting the data that my research is based on. I really appreciate the financial assistance I received from the National Research Foundation, Wits Bursaries and the Department of Higher Education and Training Gap funding.

TABLE OF CONTENTS

LIST OF FIGURES

LIST OF TABLES

CHAPTER 1

GENERAL INTRODUCTION

4.3 **Introduction**

Radiation beams are used medically to kill cancer cells. However, these beams can also kill healthy cells if they are not used properly. Therefore, to produce positive outcomes, accurate amount of radiation dose must be given to a patient. Many factors must be considered to achieve these desired outcomes, including radiation field size, the energy of the radiation beam and positioning of a patient to minimise exposure of healthy cells to radiation during radiotherapy. The field size of radiation beams must be chosen according to the size and location of the tumour or area to be irradiated. In consultation with an oncologist an appropriate amount of radiation beam dose must be selected to treat a patient.

Field sizes can be classified as small and large. Small fields of radiation are defined as fields that are small compared to the lateral range of charged particles, are produced by a source that is partially blocked by the collimators of a Linear Accelerator (LINAC) and are either smaller or equal to the sensitive dimensions of a radiation detector (Alfonso et al., 2008; Das, Ding and Ahnesjö, 2007; International Atomic Energy Agency, 2017). Field sizes that do not meet these conditions are classified as large fields.

Radiation detectors are used to determine the amount of radiation dose absorbed by a medium or a patient. There are various types of detectors, including air-filled ionisation chambers, radiographic films, thermoluminescent detectors (TLDs), silicon diode dosimeters, Metal Oxide Semiconductor Field Effect Transistor (MOSFET) detectors, alanine detectors and diamond detectors.

This study used air-filled ionisation chambers and a diamond detector to determine beam profiles, tissue phantom ratios, and output factors. Beam profiles are a two-dimensional graph representation of dose distribution from the central axis at a certain depth in a medium (Patatoukas et al., 2018). Tissue-phantom ratios are defined as ratios of the absorbed dose in water at an arbitrary point of measurement in a field size of 10 cm x 10 cm to the absorbed dose in water at a reference depth of 10 cm in a field size of 10 cm x 10 cm (Khan, 1994; Podgorsak, 2005). Output factors are defined as the ratios of absorbed dose in water at a point of measurement in a specific field size to the absorbed dose at the same point of measurement in field size 10 cm x 10 cm (Khan, 1994; Podgorsak, 2005).

This study argues that radiation detectors that have different sensitive volume sizes and materials measure different amount of absorbed dose for the same field sizes. A 0.6 cm^3 and 0.125 cm^3 air-filled ionisation chamber in a 1 cm $\times$ 1 cm field size do not measure the same amount of absorbed dose. Understanding this will help medical physicists to easily identify small field sizes when calibrating the beam output of a LINAC and easily determine when to use a suitable detector for small field dosimetry.

1.2 Significance of the study

In South Africa, as a developing country, there has been an increase in public and private institutions that use radiation to treat cancer patients using varying technologies. Including LINACs that can produce both small and large fields of radiation. The results of this study will assist in determining a suitable detector for small field dosimetry in a clinical environment. A suitable detector for small field dosimetry will help medical physicists in reducing uncertainty in measurements when calibrating the beam output of a LINAC. This will ultimately help to produce favourable outcomes when patients are treated using small field techniques, such as Intensity Modulated Radiation Therapy (IMRT).

1.3 Aims of the study

The study aims to investigate the behaviour of various detectors in different field sizes. Investigating the effect of detector orientation, size of the sensitive volume and detection material on the amount of absorbed dose measured by a detector in various field sizes.

1.4 Objectives of the study

The objectives of this study are firstly to calculate the tissue phantom ratios using a PTW 30013 Farmer ionisation chamber, PTW 31010 semi-flex ionisation chamber and PTW 60019 synthetic single-crystal diamond detector oriented perpendicular and parallel to the beam. These tissue phantom ratios are then used to calculate the ranges of charged particles. The ranges of charged particles are used to determine small field sizes of radiation. The ranges of charged particles are compared to the sensitive volume lengths of the detectors under investigation to determine whether they are suitable to be used in small field dosimetry.

Secondly, to calculate output factors using the detectors oriented perpendicular and parallel to the beam in different field sizes. The output factors are compared to each other to determine how much they vary with each other.

Finally, to measure the 6 MV photon beam profiles using the detectors oriented perpendicular and parallel to the beam in different field sizes. Beam profiles obtained when the detectors are oriented perpendicular and parallel to the beam are compared to each other to determine how much they vary with each other. The beam profiles are also used to determine the irradiation field sizes. These irradiation field sizes are then compared to the geometric field sizes.

1.5 Problem statement

Cancer is one of the leading causes of death in South Africa and the world. There are different ways to treat cancer. Cancerous cells can be removed by surgery, brachytherapy or radiotherapy. The selected treatment depends on the type of cancer a patient is diagnosed with.

In radiotherapy, a LINAC can produce high energy radiation beams that can kill the targeted cancer cells. However, if the radiation beam output produced by a LINAC is not correctly calibrated it can lead to either under or overexposure of a patient to radiation. This will lead to a patient either receiving insufficient radiation to kill cancer cells or excessive doses that may kill normal and healthy cells in the patient.

It is essential that the amount of absorbed dose of radiation produced by a LINAC, is measurable and known before treatment. A radiation detector is used to measure the amount of absorbed dose that a patient would receive if treated with a LINAC.

Since the materials that are used to make the sensitive volume of a detector are not the same as that found in the human body. The characteristics of a detector that are used to measure the absorbed dose must be better understood. Additionally it is important to study the effect of the detector orientation, the size of the sensitive volume and the detection material of a detector on the absorbed dose measured. This will lead to an improved understanding of which detector is suitable for large and small field dosimetry.

1.6 Hypothesis

In radiotherapy, a beam of radiation incident on a medium, deposits a known amount of energy per unit mass to that medium. The determination of an accurate amount of absorbed dose to the medium can be achieved by using appropriate radiation detectors.

1.7 Research questions

Research question 1: How do radiation detectors behave in small and large fields?

- Research sub-question 1: Does a signal obtained by a detector depend on the radiation field size?
- Research sub-question 2: Does a signal obtained by a detector depend on the sensitive material of a detector?
- Research sub-question 3: Does a signal obtained by a detector depend on the orientation of a detector to the beam?
- Research sub-question 4: Which detector is suitable for small field dosimetry?

1.8 Assumptions

Radiation detectors used in this study have been calibrated against detectors at a Primary Standard Dosimetry Laboratory (PSDL) at reference conditions of 20 ^{o}C, 101.33 kPa and 50% relative humidity. Each detector is given a calibration certificate containing a calibration coefficient that links the radiation dosimetry measurements of the detector to international standards.

1.9 Format of study

The structure of this research report is as follows:

CHAPTER 1 GENERAL INTRODUCTION,

CHAPTER 2 LITERATURE REVIEW OF RADIATION DOSIMETRY,

CHAPTER 3 METHODOLOGY OF RADIATION MEASUREMENTS,

CHAPTER 4 RESULTS,

CHAPTER 5 DISCUSSION,

CHAPTER 6 CONCLUSIONS AND RECOMMENDATIONS,

REFERENCES

CHAPTER 2
LITERATURE REVIEW OF RADIATION DOSIMETRY

2.1 Introduction

Four modalities are widely used for cancer treatment (Abbas and Rehman, 2020). These modalities are brachytherapy, radiotherapy, chemotherapy and surgery. Brachytherapy can be divided into two types, i.e., intracavitary and interstitial brachytherapy (Podgorsak, 2005). Intracavitary brachytherapy uses radionuclide sources that are placed inside body cavities near the area to be treated. Whereas, in interstitial brachytherapy, radionuclide sources are placed within the area to be treated. Radionuclide sources that can be used in brachytherapy include ^{60}Co, ^{137}Cs, ^{99}Mo and others that are artificially produced by institutions. The sources used in brachytherapy can emit either photons, beta or neutron particles. Radiotherapy uses machines to create external radiation beams that are used to treat a patient. These beams can be made of photons, electrons or other heavy particles, such as neutrons. Chemotherapy uses anti-cancer drugs to kill cancerous cells. These drugs can be taken as pills, injections, intravenously or directly into a body cavity. Surgery is the removal of cancerous cells from the body by a surgeon.

Radiation is used to kill cancer cells without damaging healthy cells because the energy that can be absorbed by tissue can be quantified and the place where the energy should be deposited can be determined before a patient is irradiated with a photon beam. This is done by calibrating the beam output, following proper procedures of dose measurement, treatment planning and patient set-up on the treatment couch (Podgorsak, 2005).

2.2 Absorbed dose

Absorbed dose (D) is defined as the biological effects caused by radiation. Mathematically, the absorbed dose (D) is defined as $\frac{d\bar{\varepsilon}}{dm}$ with units (J/kg or Gy), where $d\bar{\varepsilon}$ is the average value of the energy imparted by photons in a medium with a mass d_m (International Commission on Radiation Units and measurements, 2011).

.

2.3 Absorbed dose to a medium

Absorbed dose to a medium (D_{med}) is defined as the biological effects caused by radiation on a medium. Mathematically, the absorbed dose to a medium (D_{med}) is defined as

$$D_{med} = X\left(\frac{\overline{W}}{e}\right)\frac{\left(\frac{\bar{\mu}_{en}}{\rho}\right)_{med}}{\left(\frac{\bar{\mu}_{en}}{\rho}\right)_{air}}\Psi_{med,air} \quad (2.1)$$

where X is the exposure defined as $\frac{dQ}{dm}$ with units (C/kg), where d_Q is the absolute sum of all ion charge values of the same sign created in the air when all the electrons and positrons liberated by photons in an air of small mass d_m are completely stopped in the air. This quantity can be used to only measure ions that are produced by x-rays and γ-rays. $\overline{W} = 5.44 \times 10^{-18}$ J/ion is the average value of the energy required to produce an ion pair in dry air and e is the electron unit charge value (Boutillon and Perroche-Roux, 1987). $\frac{\overline{M}_{en}}{\rho}$ is the mass energy absorption coefficient. $\Psi_{med,air}$ is the ratio of the energy fluence in a medium to the energy fluence in air.

Photon radiation ionizes the medium by first transferring energy to orbital electrons in a medium and secondly, the energetic electrons proceed to eject other electrons in a medium by colliding with them or interact with other charged particles through electromagnetic interaction. The energy imparted to the electrons by photons is lost through collisions and radiation production, such as bremsstrahlung and pair production (Podgorsak, 2005). Therefore, the Kinetic Energy Released per Mass KERMA (K) defined as $\frac{dE_{tr}}{dm}$ with units (J/kg or Gy), where dE_{tr} is a small amount of energy transferred by photons to charged particles as kinetic energy in a medium with a small mass d_m, can be divided into two parts, the collision KERMA

$$K_{col} = \Psi\left(\frac{\bar{\mu}_{en}}{\rho}\right) \tag{2.2}$$

and radiative KERMA

$$K_{rad} = \Psi\left(\frac{\bar{\mu}_{en}}{\rho}\right)\left(\frac{g}{1-g}\right) \tag{2.3}$$

The collision KERMA in the air ($K_{col,air}$) is related to exposure (X) by the equation

$$K_{col,air} = X\left(\frac{\overline{W}}{e}\right) \tag{2.4}$$

To determine the absorbed dose to air from collision KERMA in the air at a volume of interest, the condition of Charged Particle Equilibrium (CPE) must be achieved at the volume of interest. To achieve CPE the number of charged particles leaving the volume of interest must equal to the number of charged particles entering the volume of interest. Under the condition of CPE, the absorbed dose to air is equal to the collision KERMA in air

$$D_{air} = K_{col,air} = X\left(\frac{\overline{W}}{e}\right) \tag{2.5}$$

To determine the absorbed dose to a medium from collision KERMA at a volume of interest the condition of CPE must be achieved at the volume of interest. Under the condition of CPE, the absorbed dose to a medium is equal to the collision KERMA

$$D_{med} = K_{col,med} = \Psi_{med}\left(\frac{\bar{\mu}_{en}}{\rho}\right)_{med} \tag{2.6}$$

Suppose a volume of air with a different medium inserted at the middle is irradiated with a beam of photons. The ratio of D_{med} to D_{air} is given by

$$\frac{D_{med}}{D_{air}} = \frac{\left(\frac{\bar{\mu}_{en}}{\rho}\right)_{med}}{\left(\frac{\bar{\mu}_{en}}{\rho}\right)_{air}} \Psi_{med,air} \tag{2.7}$$

where $\Psi_{med,air} = {}^{\Psi_{med}}/_{\Psi_{air}}$. Substituting equation (2.5) into equation (2.7) gives equation (2.1).

2.4 Cavity theories

Energy deposited in a medium by ionizing radiation and absorbed by a medium is measured using radiation detectors. This medium could be a water phantom. The radiation detectors are inserted at certain depths in a water phantom. Thus, displacing the volume of water at the point of absorbed dose measurement. The detector measures the energy deposited at the point of measurement that would have been absorbed by the displaced water if the detector were not present at the point of measurement. The detector does this by converting energy absorbed into electrical current that can be measured by the detector and displayed by the electrometer.

The Bragg-Gray and Spencer-Attix cavity theories relate how energies deposited by electrons are absorbed inside an air-filled ionisation chamber and the medium surrounding the detector. The Bethe theory relates how energies deposited by secondary electrons are absorbed inside a diamond detector and the medium surrounding the detector.

2.4.1 Bragg-Gray cavity theory

(Bragg, 1912; Gray, 1936) argues that the absorbed dose in an air-filled cavity of an ionisation chamber is related to the absorbed dose in the medium surrounding the air by

$$D_{med} = D_{cav}\left(\frac{\bar{S}}{\rho}\right)_{med,cav} \tag{2.8}$$

where the unrestricted mass collision stopping power ratio is $\left(\frac{\bar{S}}{\rho}\right)_{med,cav} = \frac{\left(\frac{\bar{S}}{\rho}\right)_{med}}{\left(\frac{\bar{S}}{\rho}\right)_{cav}}$.

This is true if the cavity of the ionisation chamber is small compared to the range of electrons crossing the cavity and the energy absorbed in the cavity is only deposited by electrons crossing the cavity.

2.4.2 Spencer-Attix cavity theory

Bragg-Gray cavity theory does not consider the energy deposited by secondary electrons and absorbed by the medium. (Attix, 1958) argues that a small variation of the separation distance of the parallel plate of the parallel-plate detector influences the dose measured by the detector, which should not be the case for a Bragg-Gray cavity detector. (Spencer and Attix, 1955) correct this by arguing that the absorbed dose in an air-filled cavity of an ionisation chamber is related to the absorbed dose in the medium by

$$D_{med} = D_{cav}S_{med,cav} \tag{2.9}$$

where the restricted mass collision stopping power ratio is

$$S_{med,cav} = \frac{\int_{\Delta}^{E_{max}} \Phi_E^{tot}(L_{\Delta}\copyright/\rho)_{med}dE + [\Phi_E^{tot}\Delta(S_{col}(\Delta)/\rho)_{med}\Delta]}{\int_{\Delta}^{E_{max}} \Phi_E^{tot}(\copyright(E)/\rho)_{cav}dE + [\Phi_E^{tot}\Delta(S_{col}(\Delta)/\rho)_{cav}\Delta]} \tag{2.10}$$

This is also true provided the cavity of the ionisation chamber is small compared to the range of electrons (primary and secondary) crossing the cavity and the energy absorbed in the cavity is only deposited by electrons crossing the cavity.

2.4.3 Bethe theory

Ionisation chambers use air-filled cavities as their sensitive medium, whereas, semiconductor detectors use diamond and silicon as their sensitive medium. The absorbed dose in a semiconductor of a solid-state detector is related to the absorbed dose in the medium by

$$D_{med1} = D_{med2} S_{med1,med2} \qquad (2.11)$$

where D_{med1} and D_{med2} are the absorbed dose in the medium surrounding the detector and the absorbed dose in the sensitive medium of the detector, respectively. The mass stopping power ratio

$$S_{med1,med2} = -\frac{1}{\rho}\frac{dE}{dx} = 4\pi N_A r_e^2 m_e c^2 z^2 \frac{Z}{A}\frac{1}{\beta^2}\left[\frac{1}{2}\ln\left(\frac{2m_e c^2\beta^2\gamma^2 T_{max}}{I^2}\right) - \beta^2 - \frac{\delta(\beta\gamma)}{2}\right] (2.12)$$

This is valid under the assumption that the charged particle interacts only through electromagnetic forces and energy loss through bremsstrahlung is negligible.

The (International Atomic Energy Agency, 2017) Code of Practice (CoP) states that the dose that exists in a medium in the absence of a radiation detector differs from the dose measured by a detector. This is due to the radiation detector size, detector shape and radiation detector material. To apply the Bragg-Gray cavity theory to radiation detectors it is necessary to introduce perturbation correction factors to correct for the detector response. When a radiation detector with a thin wall is inserted in a medium to measure the absorbed dose produced by high energy photons it disturbs the electron fluence in the medium, thus causing fluence perturbation. Therefore, using the Spencer-Attix cavity theory to calculate the absorbed dose in a medium give

$$D_{med} = X\left(\frac{\overline{W}}{e}\right) S_{med,cav} P_{TP} P_{pol} P_{ion} \qquad (2.13)$$

where P_{TP}, $P_{pol,}$ and P_{ion} are the air temperature and pressure, ionisation chamber polarity and ion recombination correction factors, respectively. These correction factors are described below. (Podgorsak, 2005) argues that the cavity fluence perturbation factor is unity at high energy photon beams.

i. Air temperature, pressure, and humidity correction factor

The sensitive air volume in ionisation chambers is dependent on atmospheric pressure, temperature and humidity. It is assumed the ionisation chambers are calibrated under reference conditions of 20 ^{o}C, 101.33 kPa and 50% relative humidity (Podgorsak, 2005). Since deviation from these reference conditions affects the ion collection efficiency, air temperature, and the pressure, a correction factor is used to correct for the deviation. The air temperature and pressure correction factor are given as

$$P_{TP} = \frac{(273.2 + T)}{(273.2 + T_o)} \frac{P_o}{P} \qquad (2.14)$$

where T and P are the water phantom temperature and air pressure, respectively, whereas T_o and P_o are the reference condition when the chamber was calibrated at the PSDL.

ii. Ionisation chamber polarity correction factor

The polarizing potential of an ionisation chamber can either be set to positive or negative. However, these polarities can give different current readings when applied under the same irradiation conditions. Thus, the equation

$$P_{pol} = \frac{|M_+| + |M_-|}{2M} \quad (2.15)$$

must be used to correct the polarity effect. Where M_+ and M_- are charge readings for positive and negative, respectively. M is the charge reading for the polarity that is used frequently.

iii. Ion recombination correction factor

The efficiency of ionisation chambers to collect ions also depends on the potential difference applied in the sensitive volume of the chamber. The range of the potential difference used in ionisation chambers is the one in the saturation region of a charge vs voltage curve. In this region, all the ion pairs are collected, but if the potential difference is below this saturation region some ion pairs recombine. For LINACs, ion recombination can be corrected using

$$P_{ion} = \frac{1 - \frac{V_N}{V_L}}{\frac{M_N}{M_L} - \frac{V_N}{V_L}} \quad (2.16)$$

where by M_N is the charge reading obtained when the normal operating potential difference V_N is applied across the chamber and M_L is the charge reading obtained when a lower potential difference V_L is applied across the chamber.

If a radiation detector has a calibration factor N_x and the electrometer reading is M, equation (2.13) can be written as

$$D_{med} = N_x M \left(\frac{\overline{W}}{e}\right) S_{med,cav} P_{TP} P_{pol} P_{ion} \quad (2.17)$$

To ensure safe and accurate delivery of prescribed doses to patients International Code of Practices (CoPs), such as the American Association of Physicists in Medicine report of Task Group No. 51 (AAPM TG-51) and International Atomic

Energy Agency Technical Report Series No. 398 (IAEA TRS-398) have been developed for institutions that use radiation to treat cancer patients, to follow when performing dosimetry (International Atomic Energy Agency, 2000; Almond et al., 1999). The AAPM TG-51 and IAEA TRS-398 report gives the same equation for absorbed dose to water as

$$D_w^Q = MN_{D,w}^{^{60}Co} k_Q \quad (2.18)$$

where D_w^Q is the absorbed dose to water from a radiation beam of quality Q, M is the ionisation chamber charge readings in Coulombs corrected for the standard pressure, temperature, ionisation chamber polarity, and ion recombination, $N_{D,w}^{^{60}Co}$ is the absorbed dose to water calibration factor for an ionisation chamber in a Cobalt-60 (^{60}Co) beam of quality Q and k_Q is the beam quality correction factor.

2.5 Radiation dosimetry

Radiation dosimetry deals with the measurement of energy deposited by radiation in a medium. Radiation dosimetry can be divided into two types, i.e., 2.6 Reference dosimetry and 2.7 Relative dosimetry.

2.6 Reference dosimetry

Reference dosimetry is defined as the measurement of absorbed dose according to its definition, as described in section 2.2 (Podgorsak, 2005). In reference dosimetry absorbed dose is measured using radiation detectors known as primary standards for absorbed dose determination. Primary standards for absorbed dose determination are not always suitable to be used routinely in clinics. This is due to difficulties in measuring quantities that determine absorbed dose from its definition, e.g., small changes in temperature. Others are difficulties in determining physical quantities of reference detectors, e.g., the sensitive volume of ionisation chambers and some of the reference dosimetry procedures are time-consuming to be used in clinics. Therefore, relative dosimeters are used to routinely calibrate a photon beam that is used for radiation therapy in clinics.

2.7 Relative dosimetry

Relative dosimeters are radiation detectors that have been calibrated at a PSDL or Secondary Standard Dosimetry Laboratory (SSDL). Relative detectors are used to determine absorbed dose, not from its definition. This is possible because each relative detector is given a calibration certificate containing a calibration coefficient that links the radiation dosimetry measurements of the detector to international or national standards.

2.8 Radiation field sizes

Relative dosimetry can be performed in different radiation field sizes. These field sizes of radiation can be described as small fields of radiation and large fields of radiation. Small fields of radiation are defined as fields that are small compared to the lateral range of charged particles, are produced by a source that is partially blocked by the collimators of a LINAC and are either smaller or equal to the sensitive dimensions of a radiation detector (Alfonso et al., 2008; Das, Ding and Ahnesjö, 2007; International Atomic Energy Agency, 2017). The above-mentioned conditions show that a field size can be considered small depending on the size of a radiation detector or the size of a radiation beam used to irradiate a medium.

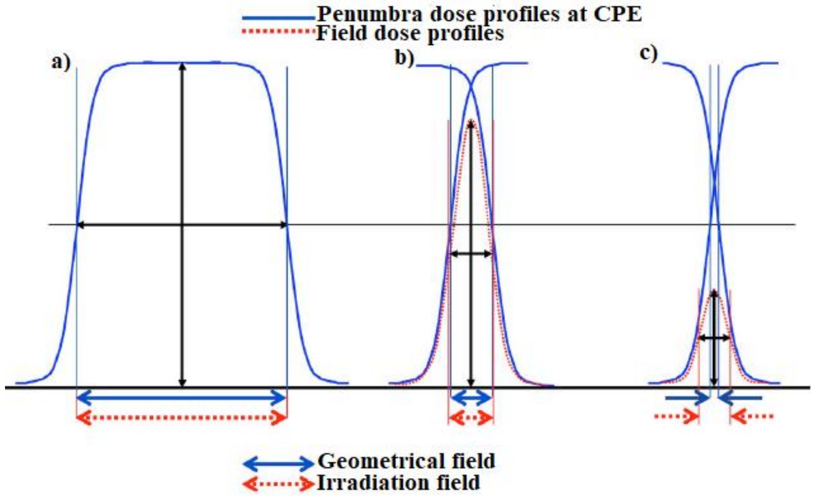

Figure 2.1 Schematic diagram comparing the geometric field and irradiation field. (a) When both field sizes are larger than the range of charged particles, (b) When both field sizes are approximately equal to the range of charged particles and (c) When both field sizes are smaller than the range of charged particles. Modified from (Das, Ding and Ahnesjö, 2007).

2.8.1 Determination of a small field

Radiation field sizes can be determined in two ways. One way is to use a light field produced by LINAC collimators in one axis and Multi-Leaf Collimators (MLCs) in another axis. Field sizes determined in this way are known as geometrical field sizes. The other way is to use the Full Width at Half Maximum (FWHM) of the beam profile. Field sizes determined in this way are known as irradiation field sizes. Irradiation field sizes are determined using

$$\mathrm{FS_{eff}} = \sqrt{\mathrm{A} \times \mathrm{B}} \qquad (2.19)$$

whereby A and B are the in-plane and cross-plane values of the FWHM of the beam profile (International Atomic Energy Agency, 2017). The geometrical field size is measured on the surface of the phantom, whereas the irradiation field size is measured at the depth of measurement (International Atomic Energy Agency, 2017).

These methods do not always produce the same field sizes (International Atomic Energy Agency, 2017). (Das, Ding and Ahnesjö, 2007) argues that for large fields the irradiation field size and the geometrical field size are the same. However, this relationship breaks down when both the irradiation field size and the geometrical field size are smaller than the charged particle range, as shown in Figure 2.1 (International Atomic Energy Agency, 2017).

The range of lateral charged particle equilibrium (r_{LCPE}) is given as

$$r_{LCPE} = 8.369 \times TPR_{20,10}(10) - 4.382 \quad (cm) \qquad (2.20)$$

where $TPR_{20,10}(10)$ is the tissue-phantom ratio measured at depth of 20 cm and 10 cm in a water phantom at a reference field size 10 cm x 10 cm (International Atomic Energy Agency, 2017). This study proposes that equation (2.20) be used to determine if a radiation field size can be described as a small field of radiation.

(Cranmer-Sargison, Charles et al, 2013) performs simulations that show that irradiation field sizes are larger than geometric field sizes for field sizes less than 0.8 cm x 0.8 cm. However, the publication does not show the amount of the difference between the irradiation field sizes and geometric field sizes and whether this difference has material impact on the reported results. This research determines the difference between irradiation field sizes and geometric field sizes and whether this difference has material impact on the reported results. Furthermore, (International Atomic Energy Agency, 2017; Alfonso et al., 2008; Das, Ding and Ahnesjö, 2007) do not specify which field sizes should be considered as small fields of radiation, although they cover an extensive theory on how to perform relative dosimetry in small field of radiations. This research investigates which filed sizes should be considered as a small field.

2.8.2 Problems in small field dosimetry

There are various factors that causes challenges when performing small field dosimetry that are not encountered in large field dosimetry. These factors are the hardening of the beam, loss of charged particle equilibrium and radiation source size occlusion.

Modern LINACs produces polychromatic energy beams. When a field size is reduced to small fields of radiation the collimators block low energy photons. This results in a small field of radiation consisting of high energy photons. This is called hardening of the beam and as a result changes the spectrum of the beam. Changing the photon fluence spectrum leads to a change in the stopping power ratio of water and detector material (International Atomic Energy Agency, 2017). However, (Eklund and Ahnesjö, 2008) show that the variation of stopping power ratios with decreasing field size from 10 cm x 10 cm to 0.3 cm x 0.3 cm is less than 1%. (Sánchez-Doblado et al., 2003) also show similar results, with the variation of stopping power ratios not more than 0.5%.

When a radiation field size is made smaller only a part of the source can be viewed from the radiation detector’s point of view. This result in a lower beam output when compared to the beam output when the complete source is visible from the radiation detector’s point of view. This led to the overlap of geometric penumbra and loss of CPE (Das, Ding and Ahnesjö, 2007).

Radiation dose measurement using ionisation chambers depends on the assumptions of the Bragg-Gray cavity theory and the Spencer-Attix cavity theory. When the ionisation chambers air cavity is smaller than the range of charged particles, the cavity is considered as nonperturbing. In small fields of radiation, the conditions of cavity theory are not fulfilled due to the range of lateral charged particles (Das, Ding and Ahnesjö, 2007).

2.9 Beam profiles

Beam profiles are a two-dimensional graph representation of dose distribution from the central axis at a certain depth (Patatoukas et al., 2018). Beam profiles consist of central region and physical penumbra. The central region is a portion of a beam profile from the central axis to within 1 cm from the geometric field size or irradiation field size (Podgorsak, 2005). The physical penumbra is a portion of a beam profile where the dose changes rapidly (Podgorsak, 2005). The physical penumbra consists of transmission penumbra, geometric penumbra and scatter penumbra. The transmission penumbra become present due to the dose being transmitted through the collimator jaws. The geometric penumbra become present due to the finite source size. The scatter penumbra become present due to in-patient x-ray scatter (Podgorsak, 2005).

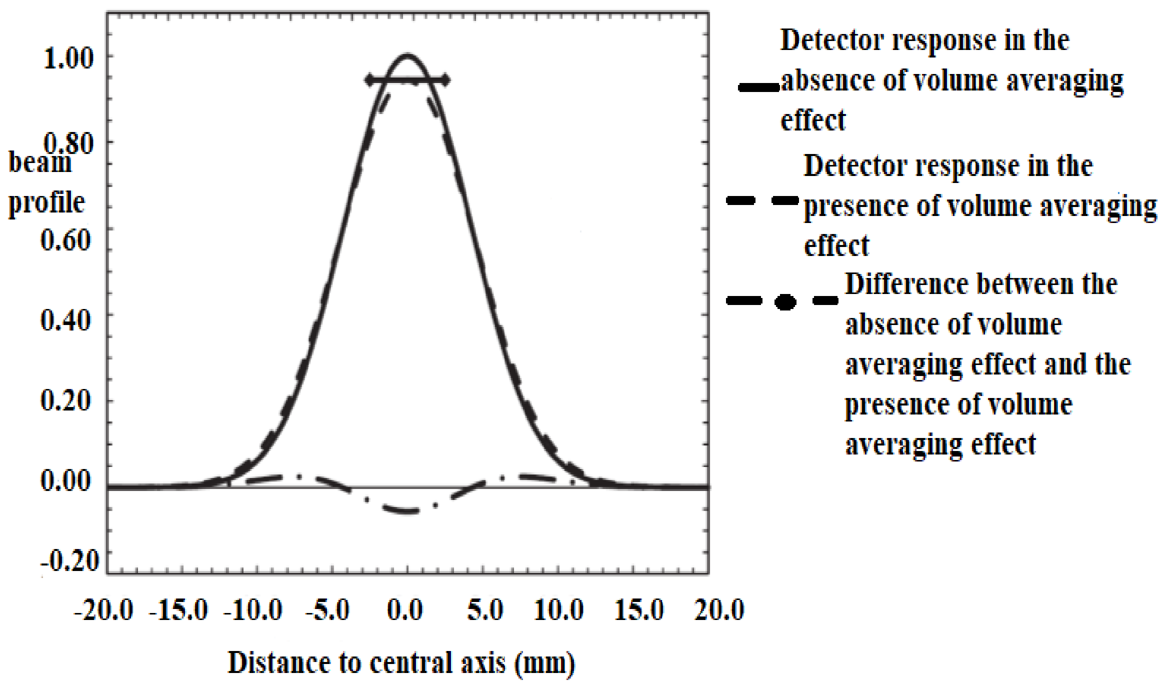

Figure 2.2 Schematic diagram showing volume averaging effect. The dashed black curve represents a detector response when volume averaging effect is present (International Atomic Energy Agency, 2017).

2.9.1 Volume averaging effect

Large sensitive volume size of radiation detectors leads to volume averaging effect and fluence perturbation (Ciancaglioni et at., 2012). (International Atomic Energy Agency, 2017) state that these effects are always entangled with each other. Volume averaging effect is characterised by under-estimation of the detector response at the central axis and over-estimation of the detector response at the physical penumbra (Wuerfel, 2013), as shown in Figure 2.2. The literature is not clear about whether the volume averaging effect is field size dependent, detector orientation dependent and detector material dependent.

2.9.2 Beam flatness and beam symmetry

When the beam flatness is measured at a depth of 10 cm in a water phantom and the largest field size possible the LINAC specification requires that the beam flatness be less than 3% (Khan, 1994; Podgorsak, 2005). To determine the precision of beam profiles the above specification must be met by the beam profiles.

The beam symmetry compares two points on the beam profile that are equidistance from the central axis. A beam profile should not differ more than 2% at these points (Khan, 1994; Podgorsak, 2005).

2.10 Output factors

Output factors are defined as ratios of absorbed dose D(A), in water at a point of measurement in a field size A to the absorbed dose D(10) at the same point of measurement in field size 10 cm x 10 cm. The point of measurement is usually set to depth of 10 cm. Output factor can be calculated as

$$\mathrm{OF} = \frac{\mathrm{D(A)}}{\mathrm{D(10)}} \tag{2.21}$$

or

$$OF = \frac{M(A)}{M(10)} \tag{2.22}$$

where M (A) are charge readings in Coulombs at a point of measurement in a field size A and M (10) are charge readings in Coulombs at the same point of measurement in field size 10 cm x 10 cm. Output factors are a dimensionless quantity.

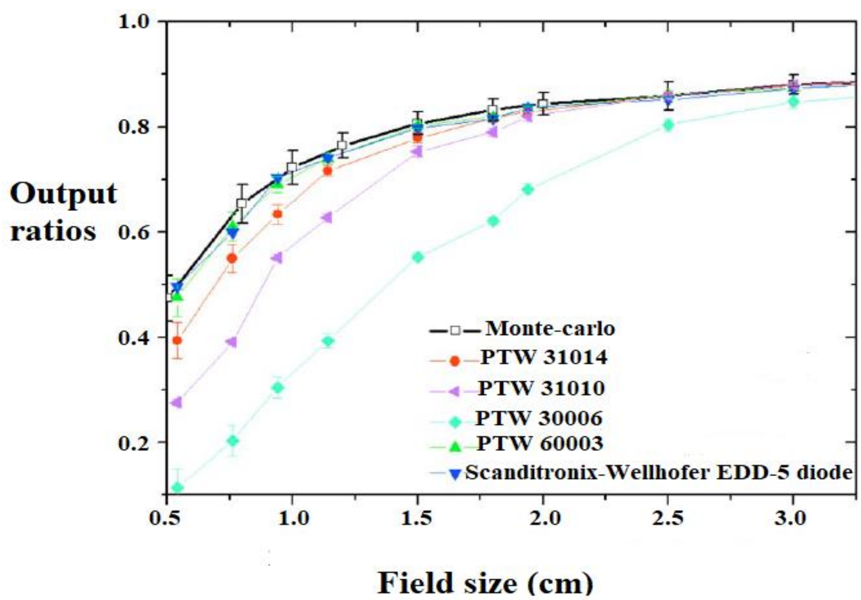

Figure 2.3 Output factors obtained by (Alfonso et al., 2008).

(Das, Ding and Ahnesjö, 2007) shows that output factors measured using different detectors demonstrate a constant decrease of output factors in field sizes 10 cm x 10 cm to 3 cm x 3 cm. There is a sharp drop of output factors for field sizes smaller than 3 cm x 3 cm, with the PTW 30006 Farmer ionisation chamber demonstrating the sharpest drop, shown in Figure 2.3. (Cranmer-Sargison et al, 2013; Ciancaglioni et at., 2012; Das et al, 2000; Haryanto, 2002; Pasquino et at., 2016; Alfonso et al., 2008) shows similar results. This study investigates the output obtained by various detectors in various field sizes and compares the output factors measured to the output factors found in literature.

2.11 Tissue-Phantom Ratio

Tissue-phantom ratios are defined as ratios of the absorbed dose D(10) in water at an arbitrary point (P) of measurement in a field size of 10 cm x 10 cm to the absorbed dose D(10) in water at a reference depth of 10 cm in a field size of 10 cm x 10 cm. $TPR_{20,\,10}(10)$ is defined as tissue-phantom ratios in a water phantom at depth 20 cm and 10 cm. Tissue-phantom ratios can be calculated as

$$\mathrm{TPR}_{20,10}(10) = \frac{\mathrm{D_P}(10)}{\mathrm{D}(10)} \qquad (2.23)$$

or

$$\mathrm{TPR}_{20,10}(10) = \frac{\mathrm{M_P}(10)}{\mathrm{M}(10)} \qquad (2.24)$$

where M_p (10) are charge readings in Coulombs at an arbitrary point (P) of measurement in a field size of 10 cm x 10 cm and M (10) are charge readings in Coulombs at a reference depth of 10 cm in a field size of 10 cm x 10 cm. Tissue-phantom ratios are a dimensionless quantity. Tissue-phantom ratios at depth 20 cm and 10 cm are used in equation (2.20) to determine the range of charged particles. The range of charged particles is compared to the size of detectors.

2.12 Percentage Depth Dose

Percentage depth dose is defined as a ratio of the absorbed dose in water at an arbitrary depth (P) to the maximum absorbed dose (D_{max}) at a depth of dose maximum multiplied by 100. The percentage depth dose can be calculated as

$$\mathrm{PDD} = \frac{\mathrm{D_P}}{\mathrm{D_{max}}} \times 100\% \qquad (2.25)$$

The depth of dose maximum largely depends on the radiation beam energy however it does also show a small dependence of the radiation beam field size (Podgorsak, 2005). The depth of dose maximum for a 6 MV photon beam is 1.5 cm (Podgorsak, 2005).

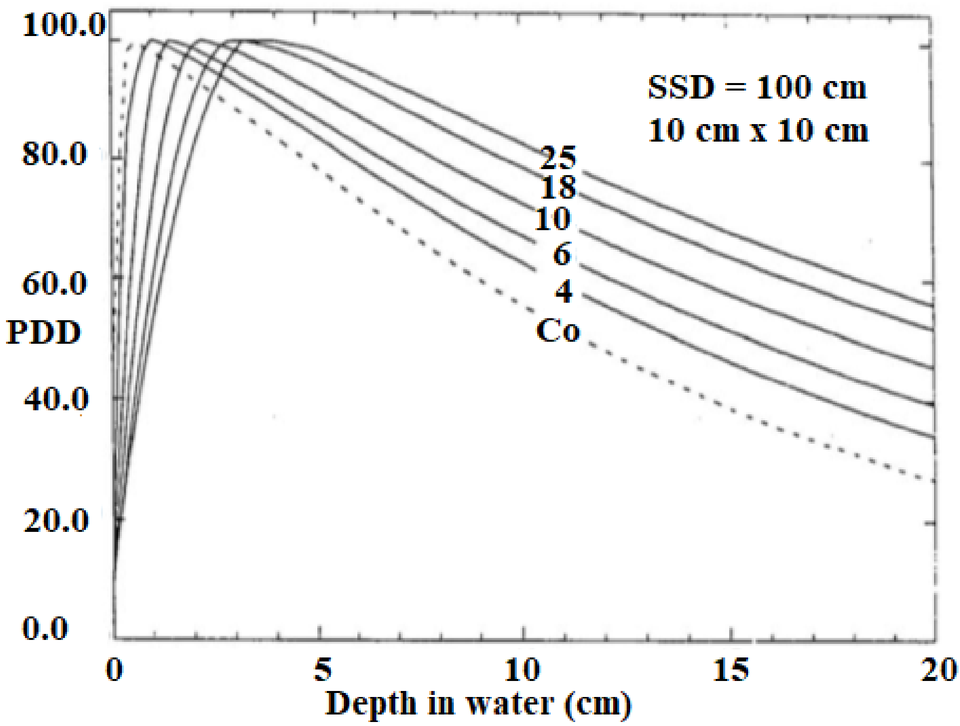

Figure 2.4 Percentage depth dose graphs obtained in a 10 cm x 10 cm beam field sizes for different beam energies.

Percentage depth dose are a two-dimensional graph that are characterized by a build-up region before the depth of dose maximum where the percentage depth increases and after the depth of dose maximum the percentage depth decreases, shown in Figure 2.4. (Ciancaglioni et at., 2012; Haryanto, 2002) shows that percentage depth dose obtained using different detectors demonstrate negligible difference to each other. The study investigates percentage depth doses obtained by various detectors and compares the percentage depth doses measured to the percentage depth doses found in literature.

CHAPTER 3

METHODOLOGY OF RADIATION MEASUREMENT

3.1 Introduction

Beam profiles, output factors, tissue phantom ratios and percentage depth dose values were used to investigate the dependency of radiation detectors to radiation field sizes, detector orientation and to determine a suitable detector for small field dosimetry. The beam profiles, output factors and percentage depth dose values were used to determine whether the detector is dependent on the radiation field sizes and detector orientation. These quantities were chosen because they can be obtained in different field sizes and different orientations following established methods in relative dosimetry (Ciancaglioni et at., 2012; Das, Ding and Ahnesjö, 2007; Haryanto, 2002; Cranmer-Sargison et al, 2013; Pasquino et at., 2016; Alfonso et al., 2008). The tissue phantom ratios were used to determine the range of charged particle and compare them to the size of detectors (International Atomic Energy Agency, 2017). This was done because the rang of charge particles must be smaller than the length of the detector, for that detector to be suitable to be used in relative dosimetry.

3.2 Methodological approach

The aim of the study was to investigate whether the detector response depends on the detector sensitive volume size, detector material and the orientation of the detector with respect to the beam. To also investigate whether the detector response depends on the radiation field size in which the measurements were taken.

Charge readings in Coulombs were collected to calculate tissue-phantom ratios $TPR_{20,10}(10)$ using equation (2.24). Beam profiles were measured to investigate whether the detector response depends on the detector sensitive volume size, detector material and the orientation of the detector with respect to the beam. Beam profiles were used to measure the in-plane and cross-plane values of the FWHM. The in-plane and cross-plane values were used in equation (2.19) to calculate the irradiation field sizes. Percentage depth doses were also measured to investigate whether the detector response depends on the detector sensitive volume size, detector material and the orientation of the detector with respect to the beam. Secondary data from literature was used to compare the percentage depth doses. Charge readings in Coulombs were collected to calculate output factors using equation (2.22). Secondary data from literature was used to compare the output factors.

3.3 Equipment

Radiation detectors used in this study is a PTW 30013 Farmer ionisation chamber, a PTW 31010 semi-flex ionisation chamber radiation and a PTW 60019 synthetic single-crystal diamond detector. These radiation detectors have been calibrated at a PSDL and have calibration certificates issued by PTW-Freiburg. A PTW MP3 water phantom and a PTW BEAMSCAN water phantom were used as irradiated medium. A 6 MV photon beam was produced by four Siemens Oncor LINACs that are synchronized together and a Elekta Versa HD LINAC.

3.3.1 Ionisation chambers

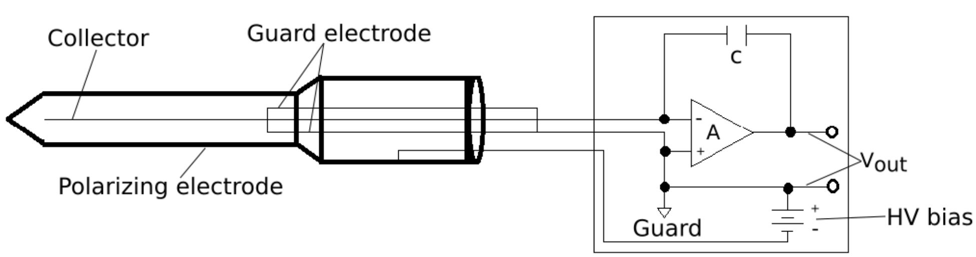

Figure 3.1 Schematic diagram of a dosimetry system, consisting of an ionisation chamber and electrometer.

The ionisation chambers used to collect the data were cylindrical in shape. The material of the sensitive volume of the ionisation chambers are an air-filled cavity with a central collecting electrode sealed by a wall that forms an outer polarizing electrode, shown in Figure 3.1. An insulator is inserted between a central collecting electrode and an outer polarizing electrode to minimise current leakage between the electrodes. Figure 3.1 shows a central electrode connected to an electro-meter that measures charge in the sensitive volume, the polarizing electrode is connected to a power supply and the guard electrode is grounded to minimise measurement of charge leakage between a central electrode and polarizing electrode. The guard electrode also determines the size of the collecting electrode. The two ionisation chambers used in this study are manufactured by PTW-Freiburg. These ionisation chambers are a PTW 30013 Farmer ionisation chamber and a PTW 31010 semi-flex ionisation chamber.

3.3.1.1 PTW 30013 Farmer ionisation chamber

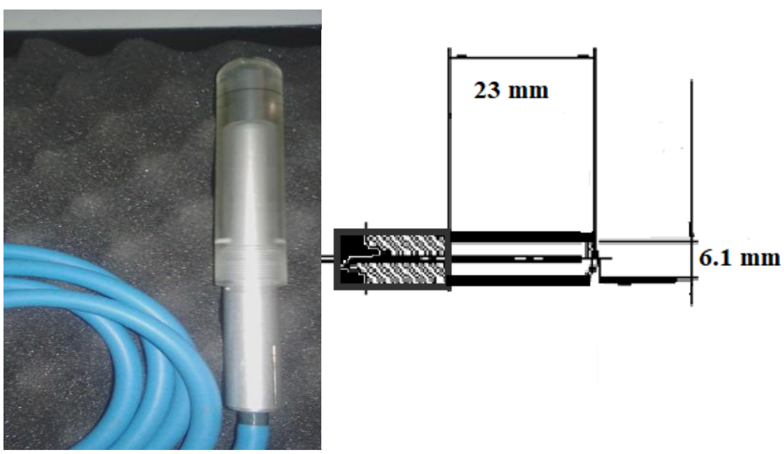

(a) (b)

Figure 3.2 (a) A picture of a PTW 30013 Farmer ionisation chamber used in this study to collect data. (b) Sensitive volume dimensions of a PTW 30013 Farmer ionisation chamber (Ptw.de, 2018).

A PTW 30013 Farmer ionisation chamber, shown in Figure 3.2 (a), was used in this study to collect the data. The sensitive volume dimensions of the ionisation chamber are shown in Figure 3.2 (b). The sensitive volume wall of the ionisation chamber is made of Poly Methyl Methacrylate PMMA and graphite. The central collecting electrode is made of 99.98% of aluminium. This ionisation chamber was calibrated in a Cobalt-60 beam. The ionisation chamber is waterproof.

Table 3.1 Specification of a PTW 30013 Farmer ionisation chamber (Ptw.de, 2018).

Ionisation chamber sensitive volume	0.6 cm^3
Wall of sensitive volume material	PMMA: length–- 0.335 mm : density–- 1.19 g/cm^3 Graphite: length - 0.09 mm : density–- 1.85 g/cm^3
Total wall area density	56.5 mg/cm^2
Dimensions of sensitive volume	Radius–- 3.05 mm Length–- 23.0 mm
Central collecting electrode material	Aluminium: diameter – 1.1 mm
Reference point of measurement	13 mm from ionisation chamber tip
Ionisation chamber voltage	400 V nominal ± 500 V maximal
Radiation energy range	Photons: 30 kV – 50 MV
Ion collection time	140 µs

Specifications of the ionisation chamber are shown in Table 3.1. This ionisation chamber is used routinely at Charlotte Maxeke Johannesburg Academic Hospital (CMJAH) to perform relative dosimetry in a 6 MV photon beam and Cobalt-60 beam. The ionisation chamber exhibit less than 0.5 % polarity effect in a Cobalt-60 beam, current leakage of not more than ± 4 fA and cable leakage of not more than 1 $\frac{pC}{Gy.cm}$. The cable attached to the ionisation chamber is approximately 1 m.

3.3.1.2 PTW 31010 semi-flex ionisation chamber

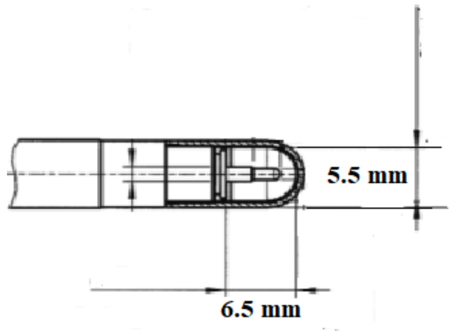

(a) (b)

Figure 3.3 (a) A picture of a PTW 31010 semi-flex ionisation chamber used to in this study to collect data. (b) Sensitive volume dimensions of a PTW 31010 semi-flex ionisation chamber (Ptw.de, 2018).

A PTW 31010 semi-flex ionisation chamber, shown in Figure 3.3 (a), was used in this study to collect the data. The sensitive volume dimensions of the ionisation chamber are shown in Figure 3.3 (b). The sensitive volume wall of the ionisation chamber is made of Poly Methyl Methacrylate PMMA and graphite. The central collecting electrode is made of 99.98% of aluminium. This ionisation chamber was calibrated in a Cobalt-60 beam. The ionisation chamber is waterproof.

Table 3.2 Specification of a PTW 31010 semi-flex ionisation chamber (Ptw.de, 2018)

Ionisation chamber sensitive volume	0.125 cm^3
Wall of sensitive volume material	PMMA: length–- 0.55 mm : density–- 1.19 g/cm^3 Graphite: length - 0.15 mm : density–- 0.82 g/cm^3
Total wall area density	78 mg/cm^2

Dimensions of the sensitive volume	Radius–- 2.75 mm Length–- 6.5 mm
The central collecting electrode material	Aluminium: diameter – 1.1 mm
The reference point of measurement	4.5 mm from ionisation chamber tip
Ionisation chamber voltage	400 V nominal ± 500 V maximal
Radiation energy range	Photons: 140 kV – 50 MV
Ion collection time	100 µs

Specifications of the ionisation chamber are shown in Table 3.2. This ionisation chamber is used routinely at CMJAH to perform relative dosimetry in a 6 MV photon beam and ^{60}Co beam. The ionisation chamber exhibit less than 2 % polarity effect in a ^{60}Co beam, current leakage of not more than ± 4 fA and cable leakage of not more than 1 $\frac{\text{pC}}{\text{Gy.cm}}$. The cable attached to the ionisation chamber is approximately 1 m.

3.3.2 Diamond detector

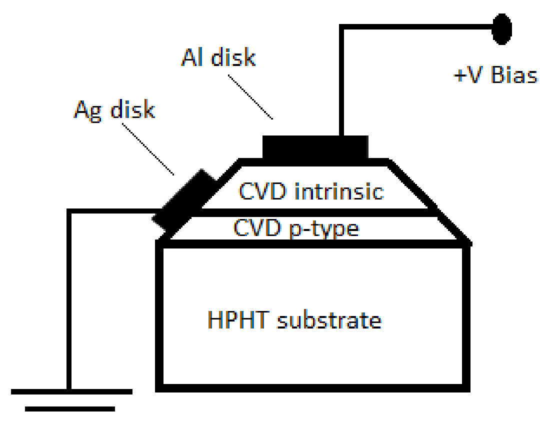

Figure 3.4 Schematic diagram of a CVD synthetic single-crystal diamond detector sensitive materials.

A PTW 60019 synthetic single-crystal diamond detector manufactured by PTW-Freiburg was used to collect the data. The micro-diamond detector was constructed by a two-step microwave plasma enhanced-Chemical Vapour Deposition (CVD) method (Di Venanzio et al., 2013; Ciancaglioni et at., 2012). A high-pressure high-temperature (HPHT) single-crystal diamond substrate was used to grow a p-type diamond layer and an intrinsic diamond layer, as shown in Figure 3.4 (Hei et al., 2016). An aluminium (Al) layer connects the intrinsic diamond layer and a positive voltage supplying terminal. This allows the diamond detector to work in a photodiode mode. A silver (Ag) layer connects the p-type diamond layer and the ground terminal. Generally, a (1.0 ± 0.1) µm thick intrinsic diamond layer is grown as the sensitive layer of the diamond detector.

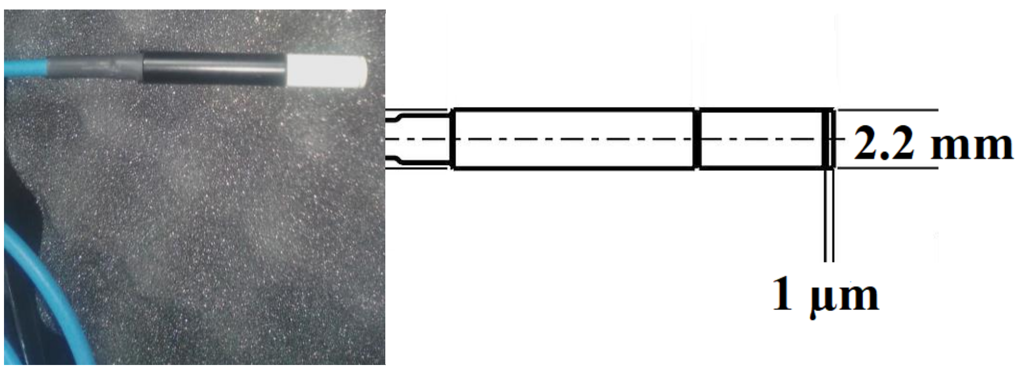

(a) (b)

Figure 3.5 (a) A picture of a PTW 60019 synthetic single-crystal diamond detector used in this study to collect data. (b) Sensitive volume dimensions of a PTW 60019 synthetic single-crystal diamond detector (Ptw.de, 2018).

Figure 3.5 (a) shows a picture of a PTW 60019 synthetic single-crystal diamond detector used in this study to collect the data. The sensitive volume dimensions of the diamond detector are shown in Figure 3.5 (b). The enclosure of the sensitive volume of the synthetic single-crystal diamond detector is made of Poly Methyl Methacrylate PMMA. This enclosure is cylindrical in shape. This diamond detector was calibrated in a Cobalt-60 beam. The diamond detector is waterproof.

Table 3.3 Specification of a PTW 60019 synthetic single-crystal diamond detector (Ptw.de, 2018).

Diamond detector sensitive volume	0.004 mm^3
Entrance window material	RW3 : 0.3 mm Epoxy : 0.6 mm Aluminium: 0.01 mm
Total window area density	101 mg/cm^2
Dimensions of the sensitive volume	Radius–- 1.1 mm Length–- 1 μm
The reference point of measurement	1 mm from detector tip
detector voltage	0 V
Radiation energy range	Photons: 100 kV – 25 MV

Specifications of the diamond detector are shown in Table 3.3. This diamond detector is used routinely at CMJAH to perform relative dosimetry in a 6 MV photon beam and ^{60}Co beam. The diamond detector exhibits leakage current of not more than ± 20 fA and cable leakage of less than 200 $\frac{\mathrm{fC}}{\mathrm{Gy.cm}}$. The cable attached to the diamond detector is approximately 1 m.

3.3.3 Water phantoms

3.3.3.1 PTW MP3 water phantom

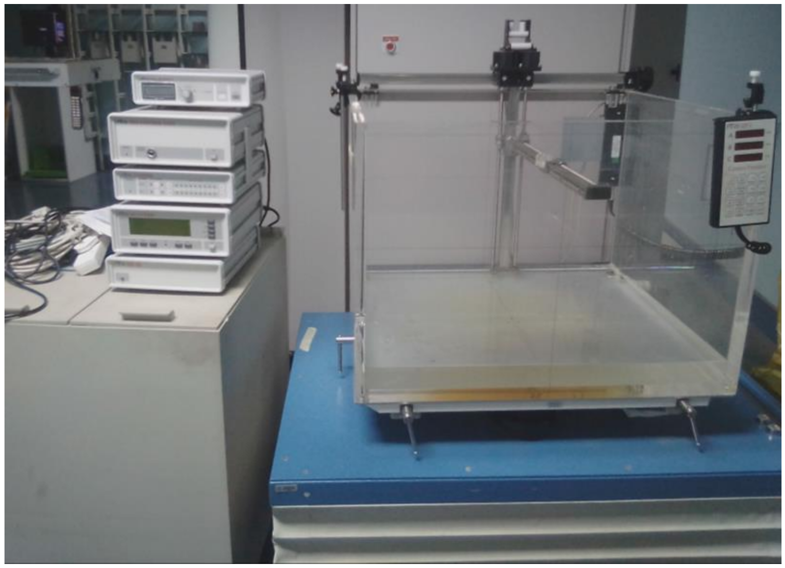

Figure 3.6 A picture of a PTW MP3 water phantom used in this study to collect data.

A PTW MP3 water phantom consists of a water tank, a detector positioning system, a water tank lifting carriage, a water reservoir carriage, dual-channel electrometer TANDEM, MEPHYSTO software and a TBA control pendant, shown in Figure 3.6. The water tank has a scanning range of 60 cm $\times$ 50 cm $\times$ 40.8 cm. The walls of the water tank are made of approximately 20 mm thick PMMA. A 3-dimension movable detector positioning system is attached to the water tank. The detector positioning system is used to mount radiation detectors inside the water tank and to accurately position them to the point of measurement. Radiation detector holders for each detector type are used to attach radiation detectors to the positioning system. The water tank lifting carriage is used to accurately position the water tank vertically. The water reservoir carriage stores approximately 220 L of deionized water.

3.2.3.2 PTW BEAMSCAN water phantom

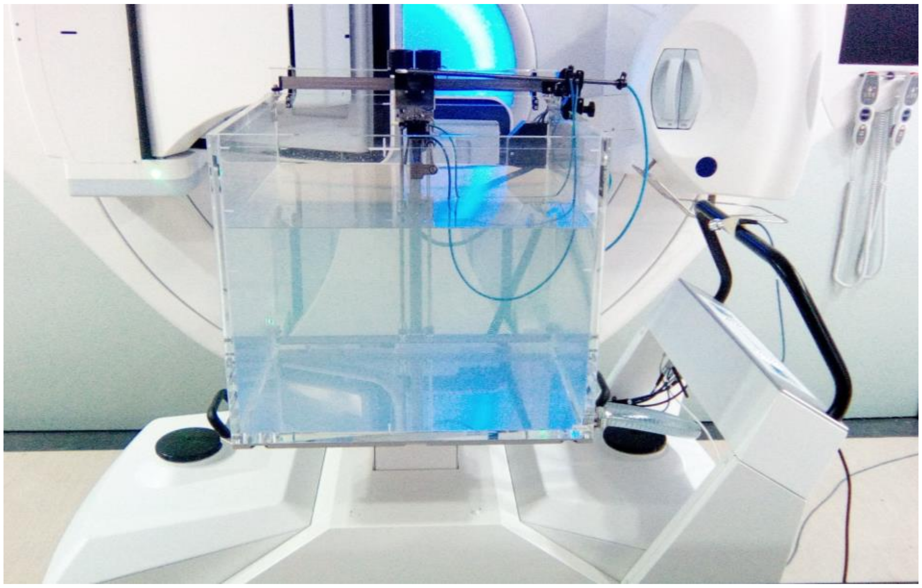

Figure 3.7 A picture of a PTW BEAMSCAN water phantom used in this study to collect data.

A PTW BEAMSCAN water phantom is an all-in-one water scanning system that consist of a water tank, a clip-in detector mounting and positioning system, a water tank lifting carriage with a built-in water reservoir, a click-fix source-to-surface-distance (SSD) adjustment tool, BEAMSCAN software, built-in web server, Wi-Fi and LAN connectivity, shown in Figure 3.7. The water tank has a scanning range of 50 cm $\times$ 50 cm $\times$ 41.5 cm. The walls of the water tank are made of approximately 15 mm thick PMMA. The positioning system is controlled with any mobile device connected to the BEAMSCAN web server. The BEAMSCAN web server allow a mobile device to use the BEAMSCAN Wizard application.

3.3.4 Linear accelerators

(a) (b)

Figure 3.8 (a) A Siemens Oncor LINAC that was used in this study to produce radiation fields. (b) A control console that was used that with a Siemens Oncor LINAC.

(a) (b)

Figure 3.9 (a) An Elekta Versa HD LINAC that was used in this study to produce radiation fields. (b) A control console that was used with an Elekta Versa HD LINAC.

A Siemens Oncor LINAC, shown in Figure 3.8 and an Elekta Versa HD LINAC, shown in Figure 3.9 were used in this study to produce a 6 MV photon beam. The LINACs consists of a gantry, a gantry stand, a treatment couch, and a control console located in a separate room that has thick shielding walls.

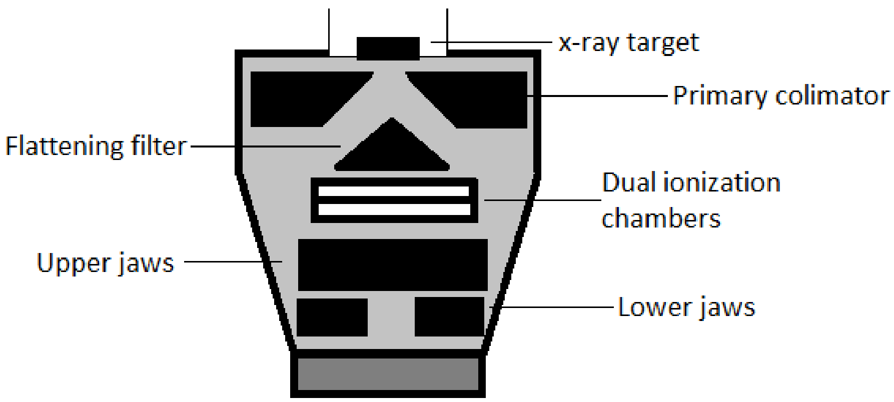

Figure 3.10 Schematic diagram of a LINAC head.

The gantry has x-ray targets, flattening filters, primary and adjustable secondary collimators, transmission ionisation chambers, field-defining light, and range finder. The x-ray target is responsible for producing photon beams in a LINAC. The flattening filters flatten the beam produced by the x-ray target. Primary collimators produce circular fields that are further reshaped by movable secondary collimators consisting of two upper and two lower independent jaws, as shown in Figure 3.10. The collimators can produce field sizes of 0 cm x 0 cm to 40 cm x 40 cm with a positioning accuracy of 0.1 cm. They also capable of producing rectangular field sizes at the isocentre. The LINAC has two transmission ionisation chambers that monitor the radiation beam output in monitor unit (MU), beam energy, radial, and transverse beam flatness and beams symmetry. These ionisation chambers are found between the flattening filters and secondary collimators, as shown in Figure 3.10. The field-defining light displays field size produced by collimators on the surface of the water phantom. Whereas the range finder determines and display the distance from the photon radiation source to the water surface. The field size and source to surface distance is displayed by a light beam on the surface of the water phantom. The gantry can rotate 180° around the treatment couch. The gantry stand houses the power source of the LINAC. The treatment couch is used to position patients, however, it was not used in this study to collect data.

3.3.5 Electrometer

Figure 3.11 A PTW-Freiburg UNIDOS E universal electrometer used in this study to record charge readings.

The responses of the radiation detectors when they were irradiated with a photon radiation beam produced by a LINAC were displayed in a PTW-Freiburg UNIDOS E universal electrometer. The electrometer can be operated in dose/charge and dose rate/current mode. The electrometer is placed in an operating room with the control console, as shown in Figure 3.11. The electrometer is capable of reading charge units.

3.4 Methods of data collection

The study was conducted at CMJAH oncology department. The study was conducted from February 2018 to April 2019. Additional readings were taken from July 2020 to August 2020 at CMJAH oncology department. The Siemens Oncor LINACs were used between February 2018 to April 2019 to collect data. An Elekta Versa HD LINAC and a PTW BEAMSCAN water phantom were used between July 2020 to August 2020 to collect data.

3.5 Charge readings and beam profile measurements

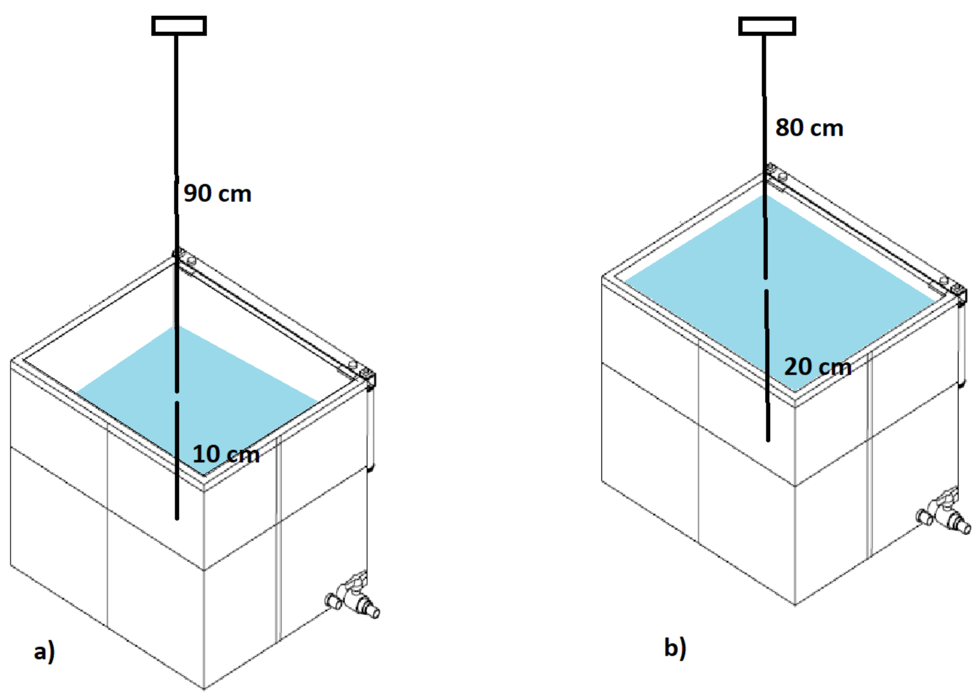

Figure 3.12 Schematic diagram showing different SAD method set-up.

Charge readings and beam profiles data was collected in 0.6 cm x 0.6 cm, 1 cm x 1 cm, 2 cm x 2 cm, 4 cm x 4 cm, 6 cm x 6 cm, 10 cm x 10 cm, 15 cm x 15 cm, 20 cm x 20 cm and 25 cm x 25 cm field sizes. Charge readings were collected in a 10 cm x 10 cm field size in order to calculate tissue-phantom ratios. A Source-to-Axis-Distance (SAD) method was used to collect charge readings and beam profiles. The SAD was set to 100 cm. The distance from the beam source to the surface of the water was set to 90 cm and the distance from the surface of the water to the point of measurement in water was set to 10 cm in order to calculate output factors and beam profiles, as shown in Figure 3.12. The distance from the beam source to the surface of the water was set to 80 cm and the distance from the surface of the water to the point of measurement in water was set to 20 cm in order to calculate tissue-phantom ratios Figure 3.12.

3.6 Collection of charge readings and beam profiles using a PTW 31010 semi-flex ionisation chamber

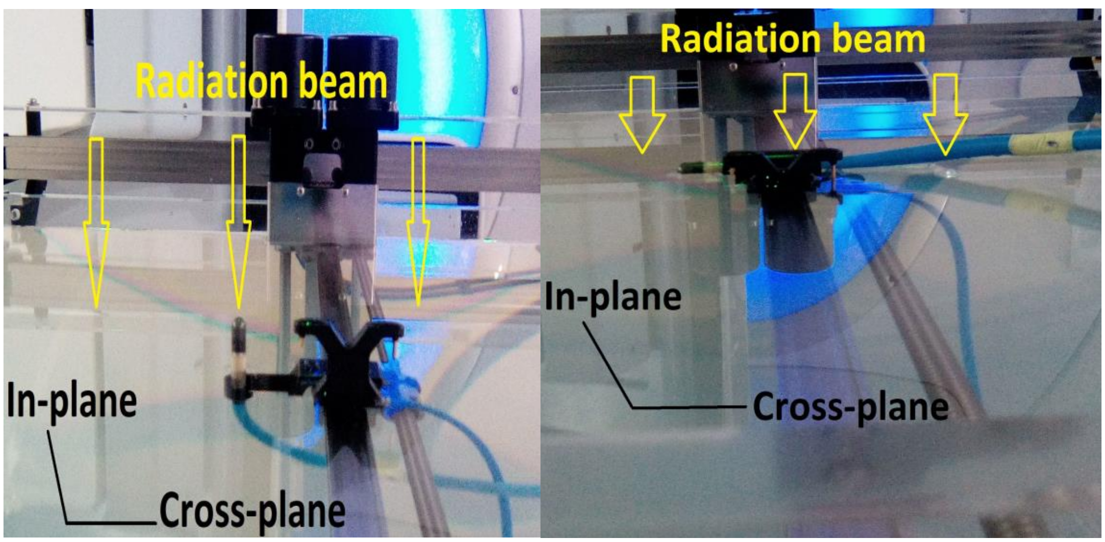

(4) (b)

Figure 3.13 (a) A PTW 31010 semi-flex ionisation chamber oriented parallel to the beam. (b) A PTW 31010 semi-flex ionisation chamber oriented perpendicular to the beam.

Charge readings and beam profiles were collected using a PTW 31010 semi-flex ionisation chamber oriented parallel to the beam and perpendicular to the beam as shown in Figure 3.13.

3.6.1 Collection of charge readings and beam profiles in a MP3 water phantom

(a) (b)

Figure 3.14 (a) A PTW TRUFIX 391 detector holder. (b) A PTW TRUFIX 441 detector holder.

The PTW MP3 water phantom was positioned such that the single detector cross wires were aligned with the laser beams produced by laser devices fitted in the treatment room. There are two laser devices in the treatment room that produce laser beams that are perpendicular to each other, along the in-plane direction and cross-plane direction. The water tank was then filled with deionized water from the water reservoir carriage. The PTW 31010 semi-flex ionisation chamber was mounted on the control arms perpendicular to the radiation beam direction using a PTW TRUFIX 391 detector holder shown in Figure 3.14 (a). In order to collect charge readings, the dual-channel electrometer TANDEM was connected to the water tank and the PTW-Freiburg UNIDOS E universal electrometer in the control room. In order to collect data for beam profiles the dual-channel electrometer TANDEM was connected to the water tank and a laptop with the MEPHYSTO software in the control room.

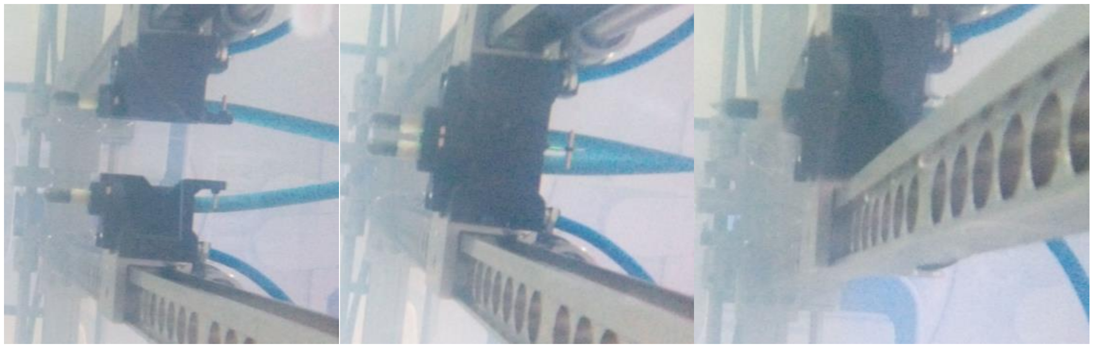

Figure 3.15 A procedure to position the sensitive volume of a detector oriented perpendicular to the beam at the point of measurement.

The scan limits were set to 40 cm x 40 cm using the control pendant. The control pendant was used to position the PTW 31010 semi-flex ionisation chamber such that the laser beam along the cross-plane was at the middle of the ionisation chamber. The front tip of the ionisation chamber was placed such that it touches the laser beam along the in-plane direction. The control pendant was used to make that position a reference point by zeroing the direction measurements displayed on the control pendant. The ionisation chamber was moved by 0.45 cm along the cross-plane. The control pendant was used to make that position a reference point by zeroing the direction measurements displayed on the control pendant. The ionisation chamber was lowered into the water using the control pendant. Looking from below the water the ionisation chamber was raised such that its reflection and the chamber overlap and appeared to be a single ionisation chamber, as shown in Figure 3.15. The control pendant was used to make that position a reference point by zeroing the direction measurements displayed on the control pendant. The ionisation chamber was lowered by 0.17 cm to align the sensitive volume with the surface of the water. The control pendant was used to make that position a reference point by zeroing the direction measurements displayed on the control pendant. The ionisation chamber was lowered by 10 cm to the point of measurement. The control consoles shown in Figure 3.8 (b) and Figure 3.9 (b) were used to set up the field sizes. The x-axis component and the y-axis component were given the length of the field size along the cross-plane and in-plane, respectively.

The PTW-Freiburg UNIDOS E universal electrometer was turned on and switched to charge mode in order to record charge readings. The electrometer was reset by pressing the STA button before a 6 MV photon beam was turned on. Three charge readings in Coulombs were recorded for each field size from the electrometer. The PTW TRUFIX 391 detector holder was removed from the control arms. The same procedure was repeated on a different day to collect another three charge values.

On the MEPHYSTO navigator under the relative dosimetry option the water tank scans option was selected to set-up the beam profile field sizes. The detector that was used to take the measurements of the beam profiles was also selected in the water tank scans option. The beam energy and the type of particles produced by the beam were selected, i.e., photons. Current readings in Amperes were recorded for each field size on the laptop. The PTW TRUFIX 391 detector holder was removed from the control arms.

The PTW 31010 semi-flex ionisation chamber was mounted on the controlled arms parallel to the radiation beam direction using a PTW TRUFIX 441 detector holder shown in Figure 3.14 (b). The control pendant was used to position the ionisation chamber where the cross wires cross each other. The ionisation chamber was lowered into the water using the control pendant. Looking from below the water the PTW 31010 semi-flex ionisation chamber was raised such that the reflection of the sensitive volume and the chamber sensitive volume overlap and appeared to be one sensitive volume. The PTW 31010 semi-flex ionisation chamber was further raised by 0.45 cm to align the sensitive volume with the surface of the water. The PTW 31010 semi-flex ionisation chamber was lowered by 10 cm to the point of measurement. The control consoles were used to set up the field sizes. Three charge readings in Coulombs were recorded for each field size from the PTW-Freiburg

UNIDOS E universal electrometer. The same procedure was repeated on a different day to collect another three charge values.

Current readings in Amperes were recorded for each field size on the laptop.

3.6.2 Collection of charge readings in a PTW BEAMSCAN water phantom

(a) (b)

Figure 3.16 (a) A PTW TRUFIX^{BS} 150 detector holder. (b) A PTW TRUFIX^{BS} 510 detector holder.

The PTW BEAMSCAN water phantom was positioned such that the cross wires were aligned with the laser beams produced by laser devices fitted in the treatment room. The water tank was then filled with deionized water from the water reservoir. The PTW 31010 semi-flex ionisation chamber was mounted on the control arms perpendicular to the radiation beam direction using a PTW TRUFIX^{BS} 150 detector holder shown in Figure 3.16 (a). The PTW 31010 semi-flex ionisation chamber was mounted on the control arms parallel to the radiation beam direction using a PTW TRUFIX^{BS} 510 detector holder shown in Figure 3.16 (b). In order to collect charge readings, the water tank was connected to the PTW-Freiburg UNIDOS E universal electrometer in the control room. In order to collect current, the water tank was connected to a laptop with the MEPHYSTO software in the control room. The scan limits were set to 40 cm x 40 cm using a mobile phone. A mobile phone was used to position the PTW 31010 semi-flex ionisation chamber to the point of measurement as described in section 3.6.1.

3.7 Collection of charge readings and beam profiles using a PTW 60019 synthetic single-crystal diamond detector

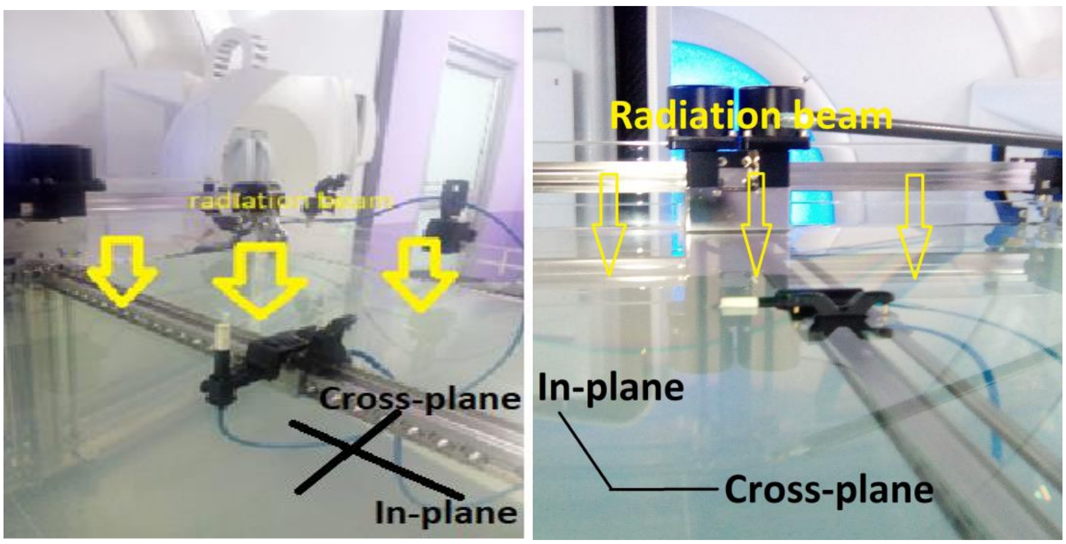

(4) (b)

Figure 3.17 (a) A PTW 60019 synthetic single-crystal diamond detector oriented parallel to the beam. (b) A PTW 60019 synthetic single-crystal diamond detector oriented perpendicular to the beam.

Charge readings and beam profiles were collected using a PTW 60019 synthetic single-crystal diamond detector oriented parallel to the beam and perpendicular to the beam as shown in Figure 3.17.

The PTW 60019 synthetic single-crystal diamond detector was mounted on the control arms perpendicular to the radiation beam direction using a PTW TRUFIX 391 detector holder shown in Figure 3.14 (a). The control pendant was used to position the diamond detector such that the laser beam along the cross-plane was at the middle of the diamond detector. The black line circling the diamond detector was aligned with the laser beam along the in-plane direction. The control pendant was used to make that position a reference point by zeroing the direction measurements displayed on the control pendant. The diamond detector was lowered into the water using the control pendant. Looking from below the water the diamond detector was raised such that its reflection and the detector overlap and appeared to be a single diamond detector. The control pendant was used to make that position a reference point by zeroing the direction measurements displayed on the control pendant. The diamond detector was lowered by 10 cm to the point of measurement. Charge readings were recorded from the PTW-Freiburg UNIDOS E universal electrometer and beam profiles were recorded on the laptop with the MEPHYSTO software, as described in section 3.6.1.

Figure 3.18 A procedure to position the sensitive volume of a detector oriented parallel to the beam to the point of measurement.

The PTW 60019 synthetic single-crystal diamond detector was mounted on the control arms parallel to the radiation beam direction using a TRUFIX 441 detector holder shown in Figure 3.14 (b). The TBA control pendant was used to position the diamond detector were the cross wires cross each other. The diamond detector was lowered into the water using the control pendant. Looking from below the water the diamond detector was raised such that the reflection of the sensitive volume and the detector sensitive volume overlap and appeared to be one sensitive volume. The diamond detector was further raised such that the black line circling the detector was position at the level of the water surface, as shown in Figure 3.18. The diamond detector was lowered by 10 cm to the point of measurement. The control consoles were used to set up the field sizes. Three charge readings in Coulombs were recorded for each field size from the electrometer. The same procedure was repeated on a different day to collect another three charge values.

Current readings in Amperes were recorded for each field size on the laptop. The PTW BEAMSCAN water phantom was setup as described in section 3.6.2 but using a diamond detector setup as described above.

3.8 Collection of charge readings and beam profiles using a PTW 30013 Farmer ionisation chamber

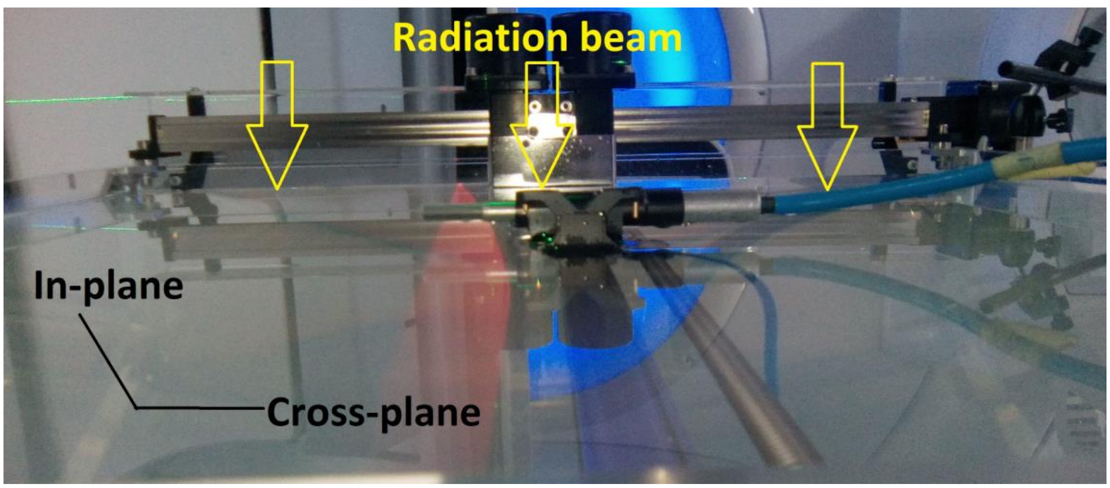

Figure 3.19 A PTW 30013 Farmer ionisation chamber oriented perpendicular to the beam.

Charge readings and beam profiles were collected using a PTW 30013 Farmer ionisation chamber oriented perpendicular to the beam as shown in Figure 3.19.

The PTW 30013 Farmer ionisation chamber was mounted on the control arms perpendicular to the radiation beam direction using a PTW TRUFIX 391 detector holder shown in Figure 3.14 (a). The control pendant was used to position the ionisation chamber such that the laser beam along the cross-plane and the in-plane was at the middle of the ionisation chamber sensitive volume. The control pendant was used to make that position a reference point by zeroing the direction measurements displayed on the control pendant. The ionisation chamber was lowered into the water using the control pendant. Looking from below the water the ionisation chamber was raised such that its reflection and the detector overlap and appeared to be a single ionisation chamber. The control pendant was used to make that position a reference point by zeroing the direction measurements displayed on the control pendant. The ionisation chamber was lowered by 10 cm to the point of measurement. Charge readings were recorded from the PTW-Freiburg UNIDOS E universal electrometer. The PTW BEAMSCAN water phantom was setup as described in section 3.6.2 but using a ionisation chamber setup as described above.

3.9 Percentage depth dose measurements

Percentage depth dose data was collected in 0.6 cm x 0.6 cm, 1 cm x 1 cm, 2 cm x 2 cm, 4 cm x 4 cm, 6 cm x 6 cm, 10 cm x 10 cm, 15 cm x 15 cm and 25 cm x 25 cm field sizes. A Source-to-Surface-Distance (SSD) method was used to collect percentage depth dose data. The SSD was set to 100 cm. The percentage depth dose data was collected using a PTW 31010 semi-flex ionisation chamber oriented perpendicular to the beam, a PTW 60019 synthetic single-crystal diamond detector oriented parallel to the beam and a PTW 30013 Farmer ionisation chamber oriented perpendicular to the beam. The setup for a PTW 31010 semi-flex ionisation chamber, a PTW 60019 synthetic single-crystal diamond detector and a PTW 30013 Farmer ionisation chamber was like the one described in section 3.6.1, section 3.6 and section 3.7 respectively, except that the detectors were not lowered to depth 10 cm.

On the MEPHYSTO navigator under the relative dosimetry option the water tank scans option was selected to set-up the percentage depth dose field sizes. The detector that was used to take the measurements of the percentage depth dose was also selected in the water tank scans option. The beam energy and the type of particles produced by the beam were selected as., i.e., photons. Current readings in Amperes were recorded for each field size on the laptop.

3.10 Methods of analysis

The data obtained was charges in Coulombs (C) and current in Amperes (A). No data was discarded during analysis. Charge readings obtained from a PTW-Freiburg UNIDOS E universal electrometer were recorded on Microsoft Excel software. The statistical error analysis and output factor graphs were done using Microsoft Excel software. Six charge values were used to calculate the standard deviation of the tissue phantom ratios and range of charged particle values. The standard deviation was calculated using Microsoft Excel STDEV.S() internal equation. The equation takes the range of cells with charge values as arguments. Current readings were analysed using MEPHYSTO software. Beam profile graphs and percentage depth dose graphs were done using Microsoft Excel software.

CHAPTER 4

RESULTS

4.1 Range of charged particles

Equation (2.20) was used to calculate the range of charged particles. Equation (2.20) required the measurements of tissue-phantom ratios TPR20, 10(10). The tissue phantom ratios were calculated using equation (2.24). Six charge values obtained at a depth of 10 cm and six charge values obtained at a depth of 20 cm were recorded. The average of charge readings obtained at a depth of 10 cm and at a depth of 20 cm were calculated and used to calculate the tissue phantom ratios.

Table 4.1 Tissue phantom ratios obtained using a PTW 31010 semi-flex ionisation chamber and a PTW 60019 synthetic single-crystal diamond detector irradiated with a photon beam produced by Siemens Oncor LINACs.

	Perpendicular orientation	Parallel orientation	Difference
PTW 31010 semi-flex ionisation chamber	0.5670 ± 0.0002	0.5640 ± 0.0029	0.0029 ± 0.0029
PTW 60019 synthetic single-crystal diamond detector	0.5688 ± 0.0001	0.5686 ± 0.0003	0.0003 ± 0.0003
Difference	0.0017 ± 0.0002	0.0045 ± 0.0029	

Table 4.2 Ranges of charged particles obtained using a PTW 31010 semi-flex ionisation chamber and a PTW 60019 synthetic single-crystal diamond detector irradiated with a photon beam produced by Siemens Oncor LINACs.

	Perpendicular orientation	Parallel orientation (cm)	Difference (cm)

	(cm)		
PTW 31010 semi-flex ionisation chamber	0.3632 ± 0.0002	0.3384 ± 0.0028	0.0248 ± 0.0029
PTW 60019 synthetic single-crystal diamond detector	0.3786 ± 0.0001	0.3762 ± 0.0003	0.0024 ± 0.0003
Difference	0.0154 ± 0.0002	0.0378 ± 0.0029	

The ranges of charged particles were calculated using equation (2.20). The difference between the range of charged particles, shown in Table 4.2, obtained using a PTW 31010 semi-flex ionisation chamber oriented parallel and perpendicular to the photon beam produced by a Siemens Oncor LINAC was found to be 0.0248. The standard deviation shows that the difference between the range of charged particles obtained using a PTW 31010 semi-flex ionisation chamber oriented parallel and perpendicular to the photon beam lies within 0.0029 of the estimated value of 0.0248 with about 68% confidence. The difference between the range of charged particles obtained using a PTW 60019 synthetic single-crystal diamond detector oriented parallel and perpendicular to the photon beam was found to be 0.0024. The standard deviation shows that the difference between the range of charged particles obtained using a PTW 60019 synthetic single-crystal diamond detector oriented parallel and perpendicular to the photon beam lies within 0.0003 of the estimated value of 0.0024 with about 68% confidence. The difference between the range of charged particles obtained using a PTW 31010 semi-flex ionisation chamber and a PTW 60019 synthetic single-crystal diamond detector oriented perpendicular to the photon beam was found to be 0.0154. The standard deviation shows that the difference between the range of charged particles obtained using a PTW 31010 semi-flex ionisation chamber and a PTW 60019 synthetic single-crystal diamond detector oriented perpendicular to the photon beam lies within 0.0002 of the estimated value of 0.0154 with about 68% confidence. The difference between the range of charged particles obtained using a

PTW 31010 semi-flex ionisation chamber and a PTW 60019 synthetic single-crystal diamond detector oriented parallel to the photon beam was found to be 0.0378. The standard deviation shows that the difference between the range of charged particles obtained using a PTW 31010 semi-flex ionisation chamber and a PTW 60019 synthetic single-crystal diamond detector oriented parallel to the photon beam lies within 0.0029 of the estimated value of 0.0378 with about 68% confidence.

Table 4.3 The difference between the ranges of charged particles obtained using a PTW 31010 semi-flex ionisation chamber and a PTW 60019 synthetic single-crystal diamond detector and the diameter, and the length of the detectors irradiated with a photon beam produced by Siemens Oncor LINACs.

	Perpendicular orientation (cm)	Parallel orientation (cm)
PTW 31010 semi-flex ionisation chamber	0.3632–- 0.5500 = -0.1868 ± 0.0002 0.3632–- 0.6500 = -0.2868 ± 0.0002	0.3384–- 0.5500 = -0.2116 ± 0.003 0.3384–- 0.6500 = -0.3116 ± 0.003
PTW 60019 synthetic single-crystal diamond detector	0.3786 - 0.2200 = 0.1586 ± 0.0001 0.3786 - 0.0001 = 0.3779 ± 0.0001	0.3763 - 0.2200 = 0.1563 ± 0.0003 0.3762 - 0.0001 = 0.3759 ± 0.0003

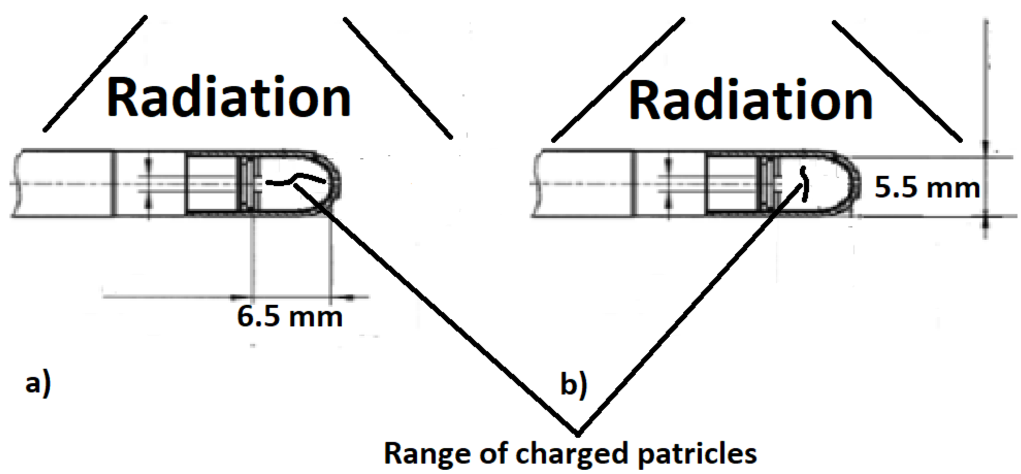

Figure 4.1 Schematic diagram comparing the range of charged particles to, a) the length of the PTW 31010 semi-flex ionisation chamber oriented perpendicular to the beam and b) the diameter of the PTW 31010 semi-flex ionisation chamber oriented perpendicular to the beam.

The diameter and the length of the PTW 31010 semi-flex ionisation chamber oriented perpendicular to the beam was found to be 0.1868 cm and 0.2868 cm longer than the range of charge particles, respectively, shown in Table 4.3. Figure 4.1 show a schematic diagram comparing the range of charged particles to the length and diameter of the PTW 31010 semi-flex ionisation chamber oriented perpendicular to the beam.

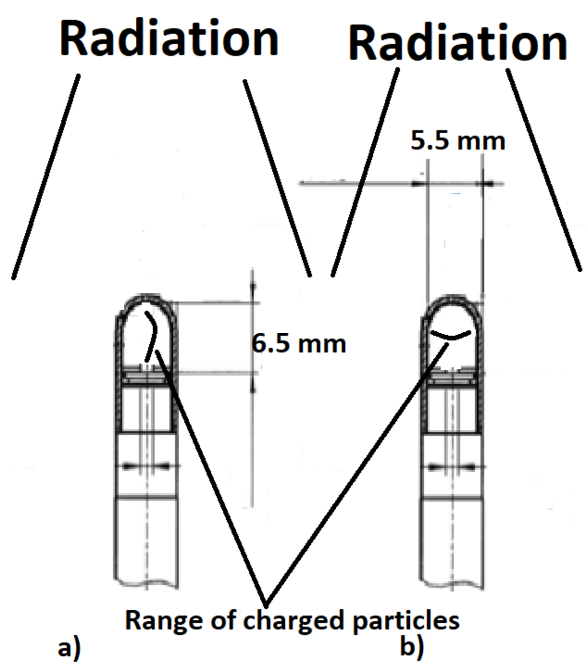

Figure 4.2 Schematic diagram comparing the range of charged particles to, a) the length of the PTW 31010 semi-flex ionisation chamber oriented parallel to the beam and b) the diameter of the PTW 31010 semi-flex ionisation chamber oriented parallel to the beam.

The diameter and the length of the PTW 31010 semi-flex ionisation chamber oriented parallel to the beam was found to be 0.2116 cm and 0.3116 cm longer than the range of charge particles, respectively. Figure 4.2 show a schematic diagram comparing the range of charged particles to the length and diameter of the PTW 31010 semi-flex ionisation chamber oriented parallel to the beam.

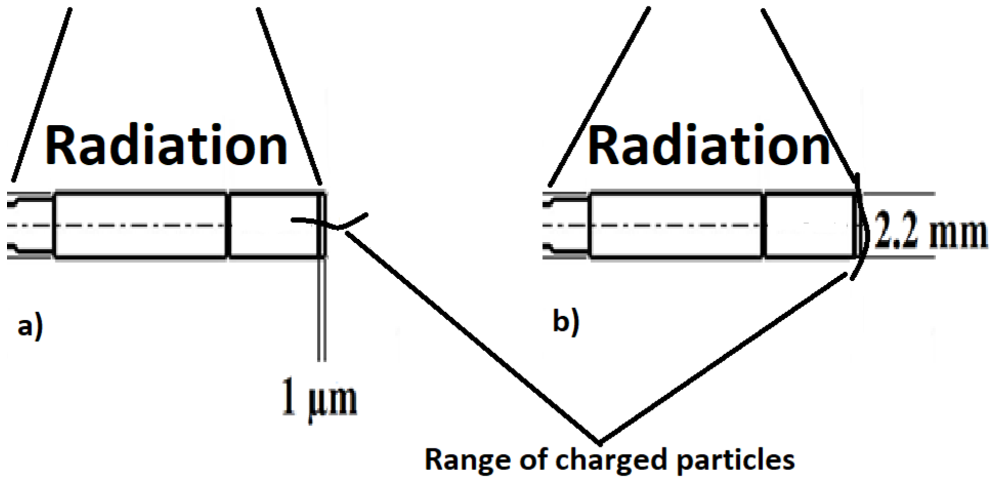

Figure 4.3 Schematic diagram comparing the range of charged particles to, a) the length of the PTW 60019 synthetic single-crystal diamond detector oriented perpendicular to the beam and b) the diameter of the PTW 60019 synthetic single-crystal diamond detector oriented perpendicular to the beam.

The diameter and the length of the PTW 60019 synthetic single-crystal diamond detector oriented perpendicular to the beam was found to be 0.1586 cm and 0.3779 cm shorter than the range of charge particles, respectively. Figure 4.3 show a schematic diagram comparing the range of charged particles to the length and diameter of the PTW 60019 synthetic single-crystal diamond detector oriented perpendicular to the beam.

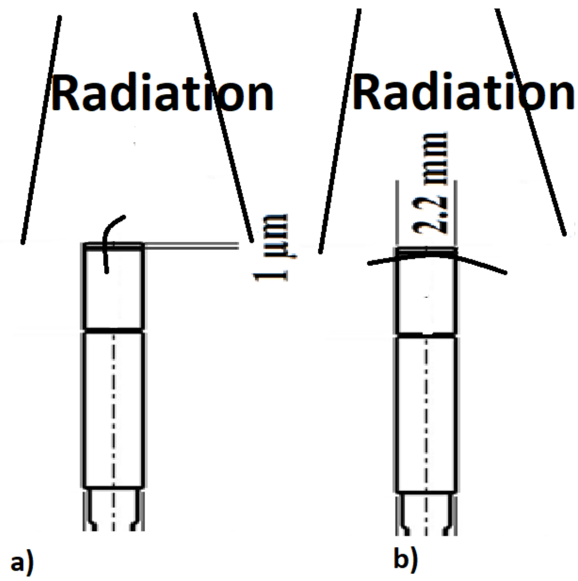

Figure 4.4 Schematic diagram comparing the range of charged particles to, a) the length of the PTW 60019 synthetic single-crystal diamond detector oriented parallel to the beam and b) the diameter of the PTW 60019 synthetic single-crystal diamond detector oriented parallel to the beam.

The diameter and the length of the PTW 60019 synthetic single-crystal diamond detector oriented parallel to the beam was found to be 0.1563 cm and 0.3759 cm shorter than the range of charge particles, respectively. Figure 4.4 show a schematic diagram comparing the range of charged particles to the length and diameter of the PTW 60019 synthetic single-crystal diamond detector oriented parallel to the beam.

Table 4.4 Tissue phantom ratios obtained using a PTW 31010 semi-flex ionisation chamber and a PTW 60019 synthetic single-crystal diamond detector irradiated with a photon beam produced by an Elekta Versa HD LINAC.

	Perpendicular orientation	Parallel orientation	Difference
PTW 31010 semi-flex ionisation chamber	0.6839 ± 0.0003	0.6792 ± 0.0012	0.0047 ± 0.0013

PTW 60019 synthetic single-crystal diamond detector	0.6787 ± 0.0005	0.6801 ± 0.0005	0.0016 ± 0.0007
Difference	0.0052 ± 0.0006	0.0011 ± 0.0013	

Table 4.5 Ranges of charged particles obtained using a PTW 31010 semi-flex ionisation chamber and a PTW 60019 synthetic single-crystal diamond detector irradiated with a photon beam produced by an Elekta Versa HD LINAC.

	Perpendicular orientation (cm)	Parallel orientation (cm)	Difference (cm)
PTW 31010 semi-flex ionisation chamber	1.3419 ± 0.0003	1.3022 ± 0.0012	0.0397 ± 0.0013
PTW 60019 synthetic single-crystal diamond detector	1.2984 ± 0.0005	1.3118 ± 0.0005	0.0134 ± 0.0007
Difference	0.0436 ± 0.0006	0.0096 ± 0.0013	

The difference between the range of charged particles, shown in Table 4.5, obtained using a PTW 31010 semi-flex ionisation chamber oriented parallel and perpendicular to the photon beam produced by an Elekta Versa HD LINAC was found to be 0.0397. The difference between the range of charged particles obtained using a PTW 60019 synthetic single-crystal diamond detector oriented parallel and perpendicular to the photon beam was found to be 0.0134. The difference between the range of charged particles obtained using a PTW 31010 semi-flex ionisation chamber and a PTW 60019 synthetic single-crystal diamond detector oriented perpendicular to the photon beam was found to be 0.0436. The difference between the range of charged particles obtained using a PTW 31010 semi-flex ionisation chamber and a PTW 60019 synthetic single-crystal diamond detector oriented perpendicular to the photon beam was found to be 0.0096.

Table 4.6 The difference between the ranges of charged particles obtained using a PTW 31010 semi-flex ionisation chamber and a PTW 60019 synthetic single-crystal diamond detector irradiated with a photon beam produced by an Elekta Versa HD LINAC.

	Perpendicular orientation (cm)	Parallel orientation (cm)
PTW 31010 semi-flex ionisation chamber	1.3419 - 0.5500 = 0.7919 ± 0.0003 1.3419 - 0.6500 = 0.6919 ± 0.0003	1.3022 - 0.5500 = 0.7522 ± 0.0012 1.3022 - 0.6500 = 0.6522 ± 0.0012
PTW 60019 synthetic single-crystal diamond detector	1.2984 - 0.2200 = 1.0784 ± 0.0005 1.2984 - 0.0001 = 1.2979 ± 0.0005	1.3118 - 0.2200 = 1.0918 ± 0.0005 1.3118 - 0.0001 = 1.3119 ± 0.0005

The diameter and the length of the PTW 31010 semi-flex ionisation chamber oriented perpendicular to the beam was found to be 0.7919 cm and 0.6919 cm shorter than the range of charge particles, respectively, shown in Table 4.6. The diameter and the length of the PTW 31010 semi-flex ionisation chamber oriented parallel to the beam was found to be 0.7522 cm and 0.6522 cm shorter than the range of charge particles, respectively. The diameter and the length of the PTW 60019 synthetic single-crystal diamond detector oriented perpendicular to the beam was found to be 1.0784 cm and 1.2978 cm shorter than the range of charge particles, respectively. The diameter and the length of the PTW 60019 synthetic single-crystal diamond detector oriented parallel to the beam was found to be 1.0918 cm and 1.3119 cm shorter than the range of charge particles, respectively. The diameter and the length of the PTW 30013 Farmer ionisation chamber oriented perpendicular to the beam was found to be

0.6986 cm shorter than the range of charge particles and 0.9914 cm longer than the range of charge particles, respectively.

4.2 Beam profile results

Beam profile data was normalised to 100% using Microsoft Excel software. The beam profile graphs were also plotted using Microsoft Excel software.

4.2.1 Beam profiles obtained using a PTW 31010 semi-flex ionisation chamber irradiated by a photon beam produced a Siemens Oncor LINAC

The in-plane beam profile flatness and the cross-plane beam profile flatness obtained when the detector was oriented perpendicular to the beam was found to be 105.90 % and 103.70%, respectively. The in-plane beam profile symmetry and the cross-plane beam profile symmetry obtained when the detector was oriented perpendicular to the beam was found to be 102.57 % and 100.93%, respectively. The in-plane beam profile was found to have deviated by -0.97 mm from the CAX. Whereas the cross-plane beam profile was found to have deviated by -0.36 mm from the CAX. The in-plane beam profile flatness and the cross-plane beam profile flatness obtained when the detector was oriented parallel to the beam was found to be 105.35 % and 104.06%, respectively. The in-plane beam profile symmetry and the cross-plane beam profile symmetry obtained when the detector was oriented parallel to the beam was found to be 102.16% and 101.53%, respectively. The in-plane beam profile was found to have deviated by -0.40 mm from the CAX. Whereas the cross-plane beam profile was found to have deviated by -1.34 mm from the CAX. The beam profiles for 1 cm x 1 cm, 2 cm x 2 cm, 4 cm x 4 cm, 6 cm x 6 cm and 15 cm x 15 cm are presented in APPENDIX A.

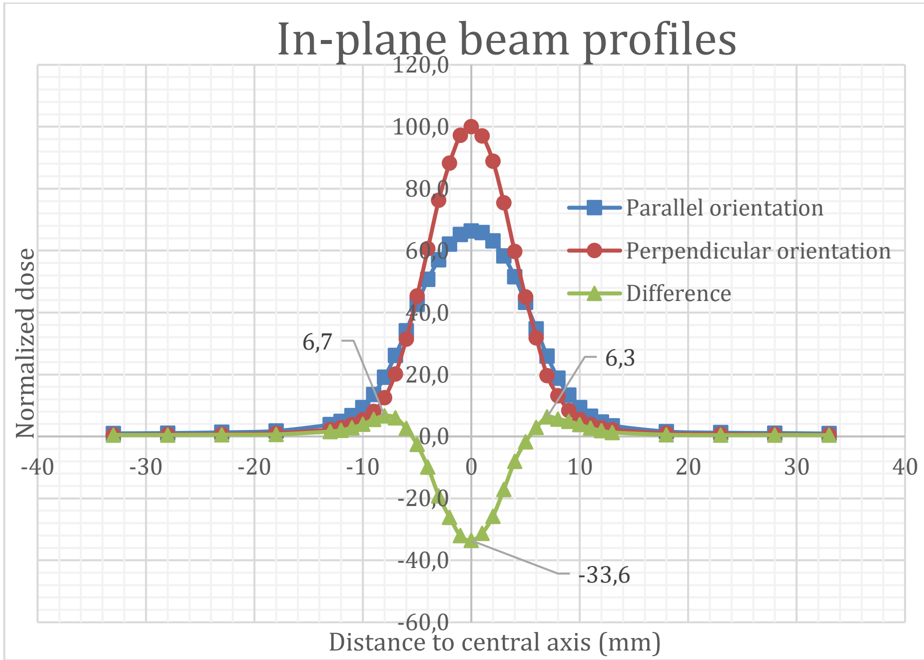

Figure 4.5 In-plane beam profiles for parallel and perpendicular orientation of a PTW 31010 semi-flex ionisation chamber in a 0.6 cm $\times$ 0.6 cm photon beam field size produced by a Siemens Oncor LINAC.

The percentage difference between the in-plane beam profiles at the central axis (CAX) of the beam, shown in Figure 4.5, obtained using a PTW 31010 semi-flex ionisation chamber oriented parallel to the photon beam and perpendicular to the photon beam produced by a Siemens Oncor LINAC was found to be -33.6%. The percentage difference between the in-plane beam profiles at distances -8 mm and +8 mm in the penumbra was found to be 6.7% and 6.3%, respectively. A negative percentage means that the detector recorded a higher current when it was oriented perpendicular to the beam than when it was oriented parallel to the beam. Whereas the positive percentage means that the detector recorded a higher current when it was oriented parallel to the beam than when it was oriented perpendicular to the beam. Figure 4.5 shows that more current was collected in the central region when the chamber was orientated perpendicular to the beam than when is orientated parallel to the beam. It also shows that more current was collected in the penumbra region when the chamber was orientated parallel to the beam than when it was orientated perpendicular to the beam.

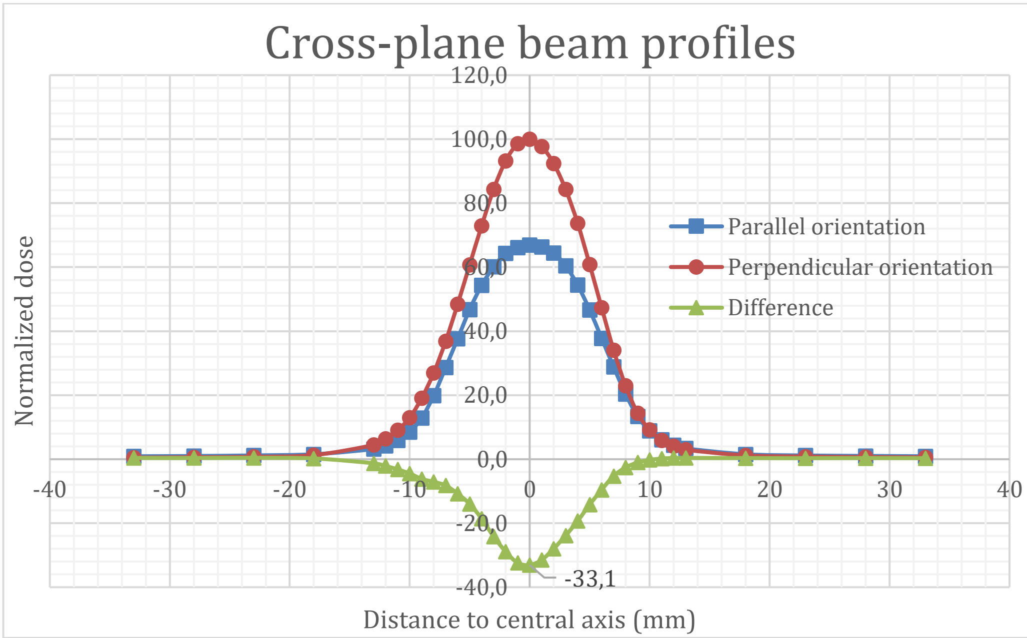

Figure 4.6 Cross-plane beam profiles for parallel and perpendicular orientation of a PTW 31010 semi-flex ionisation chamber in a 0.6 cm $\times$ 0.6 cm photon beam field size produced by a Siemens Oncor LINAC.

The percentage difference between the cross-plane beam profiles at the CAX of the beam, shown in Figure 4.6, obtained using a PTW 31010 semi-flex ionisation chamber oriented parallel to the photon beam and perpendicular to the photon beam was found to be -33.1%. Figure 4.6 shows that more current was collected when the chamber was orientated perpendicular to the beam than when it was orientated parallel to the beam along the cross-plane.

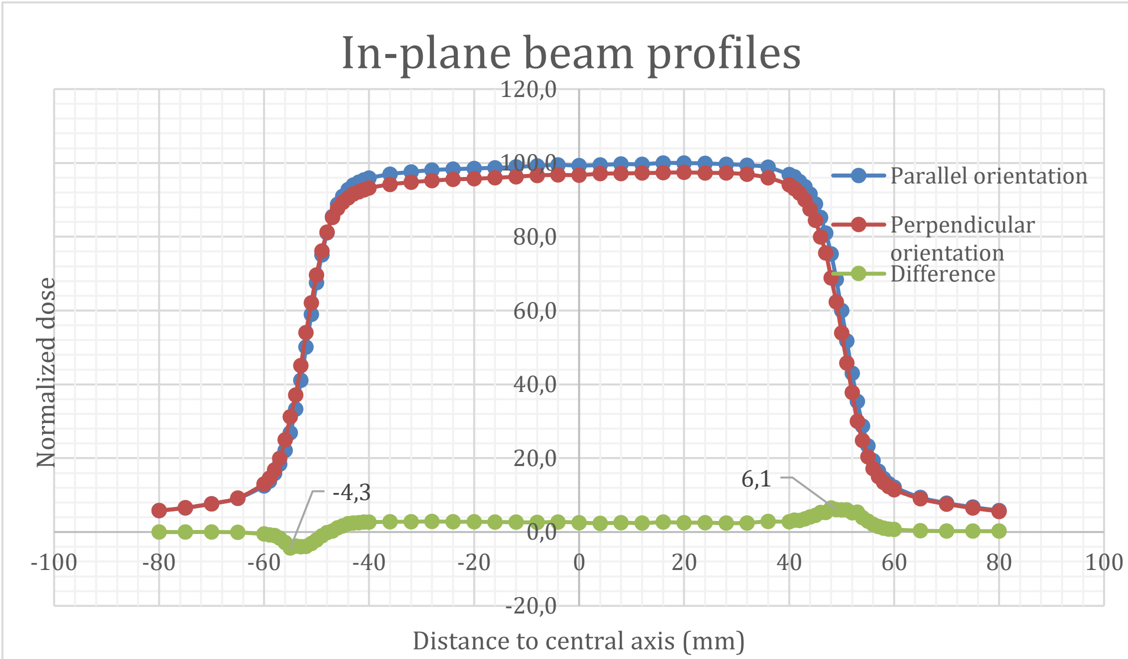

Figure 4.7 In-plane beam profiles for parallel and perpendicular orientation of a PTW 31010 semi-flex ionisation chamber in a 10 cm × 10 cm photon beam field size produced by a Siemens Oncor LINAC.

The percentage difference between the in-plane beam profiles at distances -55 mm and +49 mm in the penumbra, shown in Figure 4.7, obtained using a PTW 31010 semi-flex ionisation chamber oriented parallel to the photon beam and perpendicular to the photon beam was found to be -4.3% and +6.1%, respectively. Figure 4.7 shows that more current was collected in the central region when the chamber was orientated parallel to the beam than when it was orientated perpendicular to the beam.

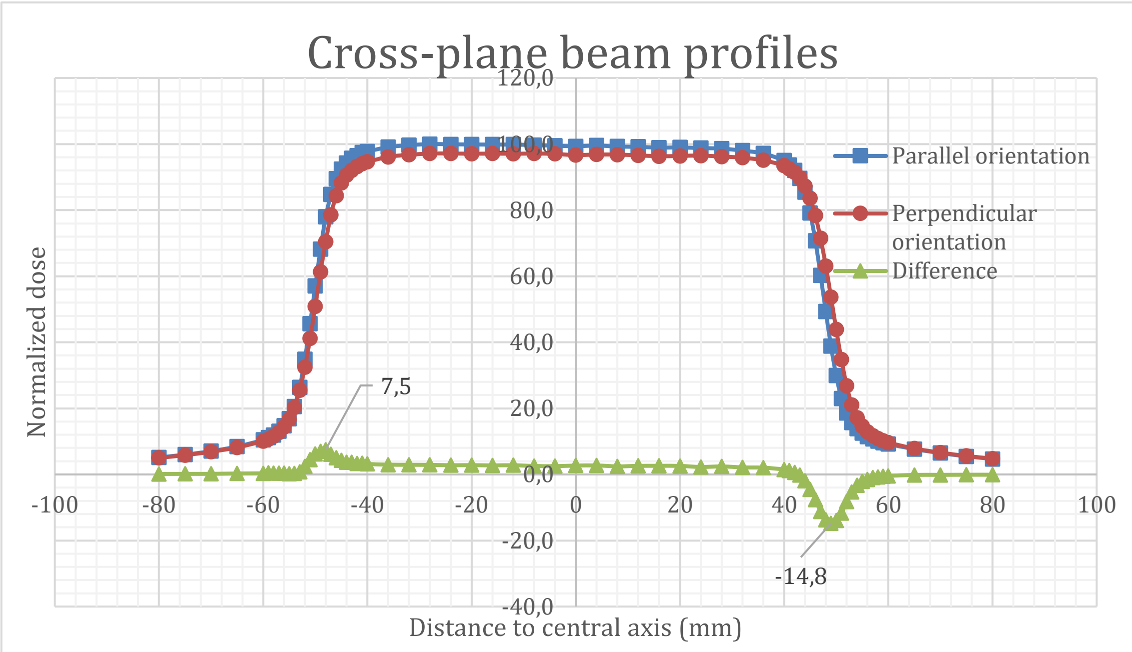

Figure 4.8 Cross-plane beam profiles for parallel and perpendicular orientation of a PTW 31010 semi-flex ionisation chamber in a 10 cm × 10 cm photon beam field size produced by a Siemens Oncor LINAC.

The percentage difference between the cross-plane beam profiles at distances -48 mm and +49 mm in the penumbra, shown in Figure 4.8, obtained using a PTW 31010 semi-flex ionisation chamber oriented parallel to the photon beam and perpendicular to the photon beam was found to be +7.5% and -14.8%, respectively. Figure 4.8 shows that more current was collected in the central region when the chamber was orientated parallel to the beam than when it was orientated perpendicular to the beam.

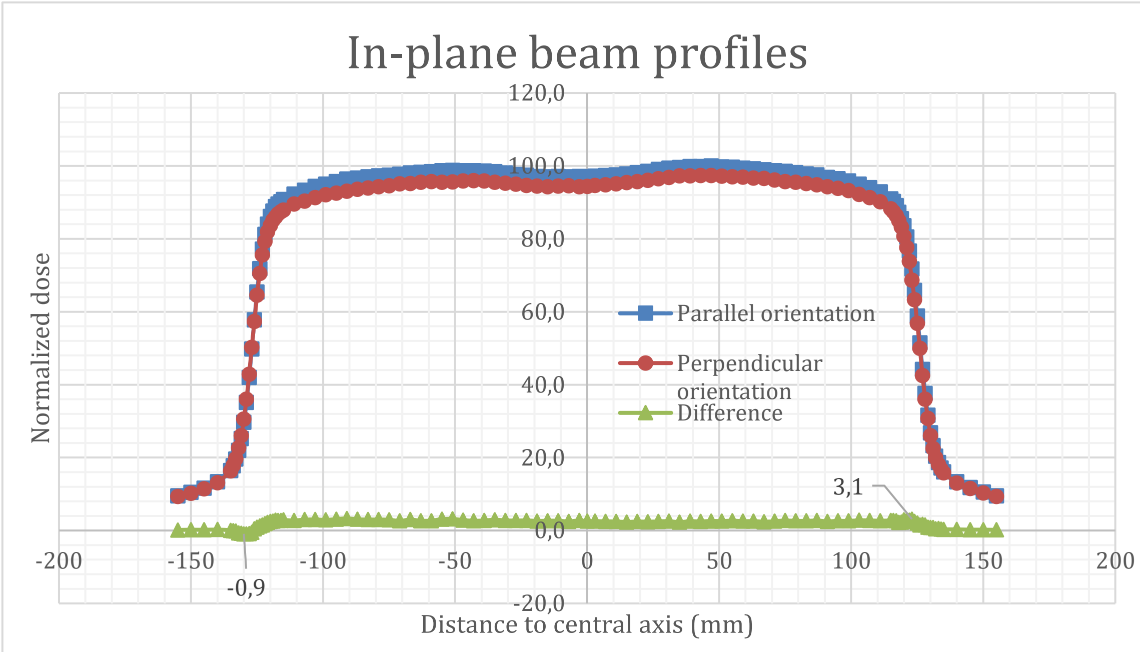

Figure 4.9 In-plane beam profiles for parallel and perpendicular orientation of a PTW 31010 semi-flex ionisation chamber in a 25 cm × 25 cm photon beam field size produced by a Siemens Oncor LINAC.

The percentage difference between the in-plane beam profiles at distances -130 mm and +123 mm in the penumbra, shown in Figure 4.9, obtained using a PTW 31010 semi-flex ionisation chamber oriented parallel to the photon beam and perpendicular to the photon beam was found to be -0.9% and +3.1%, respectively. Figure 4.9 shows that more current was collected in the central region when the chamber was orientated parallel to the beam than when it was orientated perpendicular to the beam.

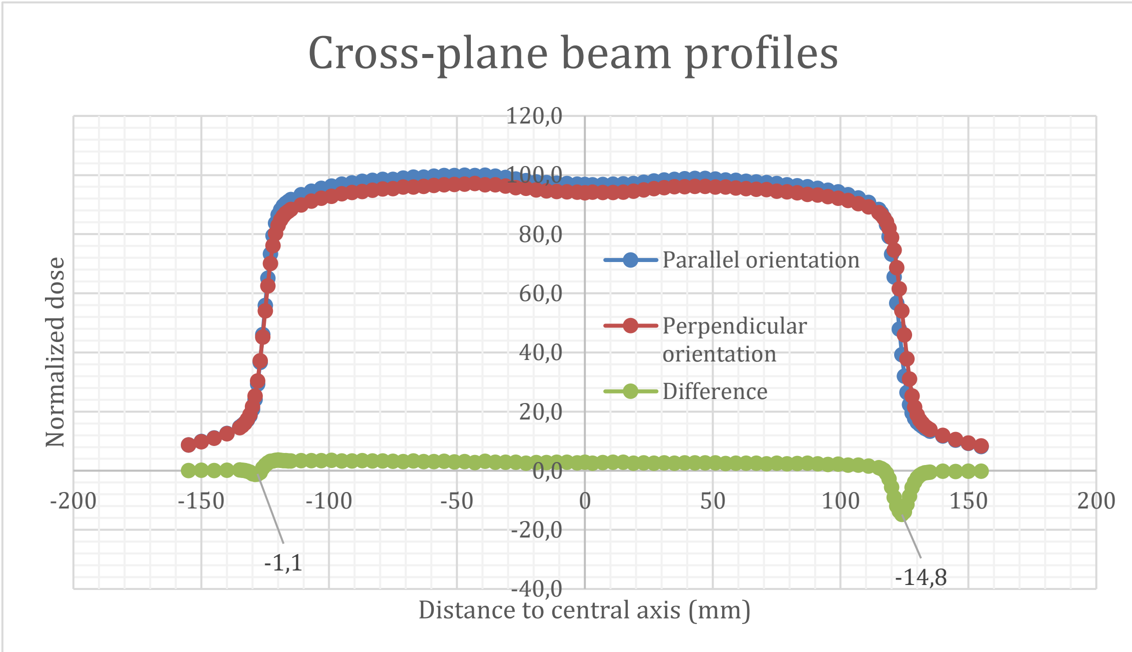

Figure 4.10 Cross-plane beam profiles for parallel and perpendicular orientation of a PTW 31010 semi-flex ionisation chamber in a 25 cm × 25 cm photon beam field size produced by a Siemens Oncor LINAC.

The percentage difference between the cross-plane beam profiles at distances -128 mm and +124 mm in the penumbra, shown in Figure 4.10, obtained using a PTW 31010 semi-flex ionisation chamber oriented parallel to the photon beam and perpendicular to the photon beam was found to be -1.1% and -14.8%, respectively. Figure 4.10 shows that more current was collected in the central region when the chamber was orientated parallel to the beam than when it was orientated perpendicular to the beam.

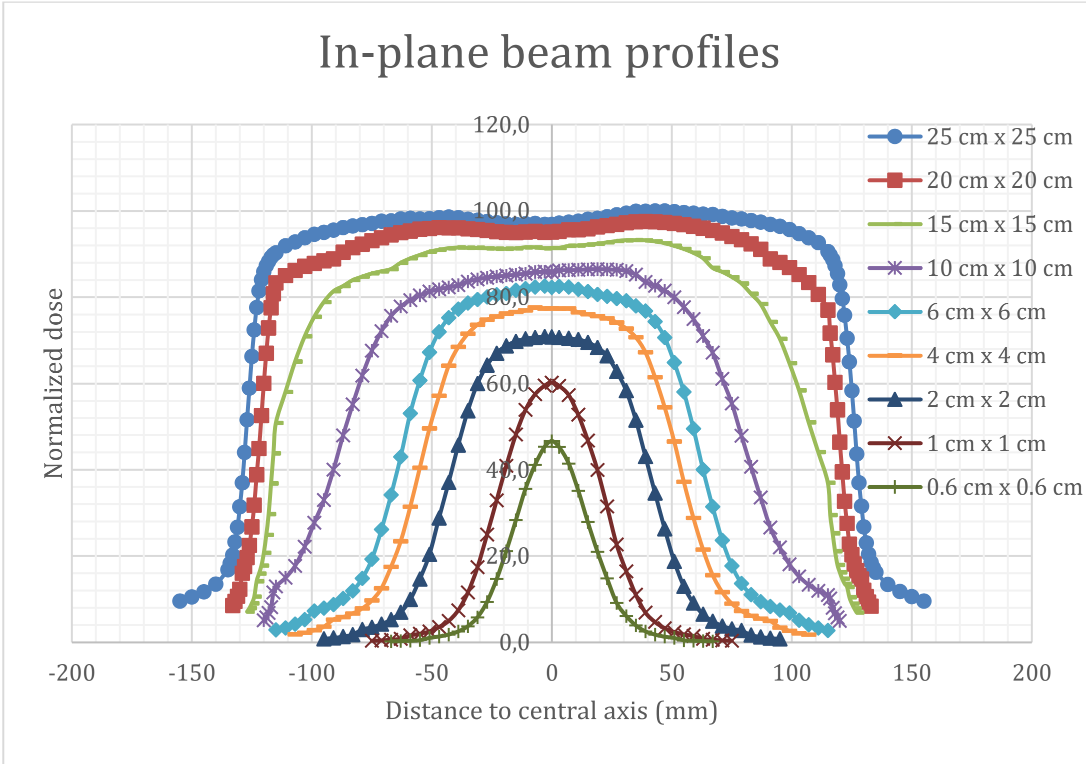

Figure 4.11 In-plane beam profiles for perpendicular orientation of a PTW 31010 semi-flex ionisation chamber in different field sizes produced by a Siemens Oncor LINAC.

Figure 4.11 shows that the amount of current collected by a detector decreases with the field sizes. The in-plane beam profiles graphs, shown in Figure 4.11, for field sizes 0.6 cm x 0.6 cm and 1 cm x 1 cm are like a normal distribution curve.

4.2.2 Beam profiles obtained using a PTW 60019 synthetic single-crystal diamond detector irradiated by a photon beam produced a Siemens Oncor LINAC

The in-plane beam profile flatness and the cross-plane beam profile flatness obtained when the detector was oriented perpendicular to the beam was found to be 103.10 % and 102.52%, respectively. The in-plane beam profile symmetry and the cross-plane beam profile symmetry obtained when the detector was oriented perpendicular to the beam was found to be 100.25 % and 100.57%, respectively. The in-plane beam profile was found to have deviated by -0.01 mm from the CAX. Whereas the cross-plane beam profile was found to have deviated by +0.06 mm from the CAX. The in-plane beam profile flatness and the cross-plane beam profile flatness obtained when the detector was oriented parallel to the beam was found to be 105.83 % and 103.92%, respectively. The in-plane beam profile symmetry and the cross-plane beam profile symmetry obtained when the detector was oriented parallel to the beam was found to be 102.22 % and 102.03%, respectively. The in-plane beam profile was found to have deviated by +0.19 mm from the CAX. Whereas the cross-plane beam profile was found to have deviated by +0.15 mm from the CAX. The beam profiles for 1 cm x 1 cm, 2 cm x 2 cm, 4 cm x 4 cm, 6 cm x 6 cm and 15 cm x 15 cm are presented in APPENDIX B.

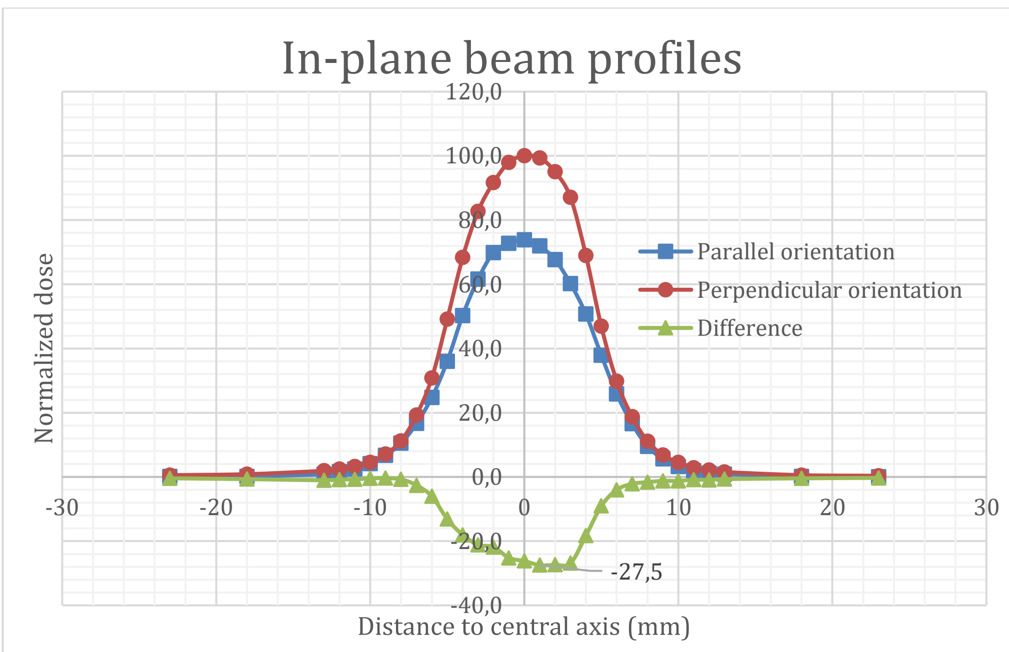

Figure 4.12 In-plane beam profiles for parallel and perpendicular orientation of a PTW 60019 synthetic single-crystal diamond detector in a 0.6 cm × 0.6 cm photon beam field size produced by a Siemens Oncor LINAC.

The percentage difference between the in-plane beam profiles at distances +1 mm in the central region, shown in Figure 4.12, obtained using a PTW 60019 synthetic single-crystal diamond oriented parallel to the photon beam and perpendicular to the photon beam was found to be -27.5%. Figure 4.12 shows that more current was collected when the detector was orientated perpendicular to the beam than when it was orientated parallel to the beam.

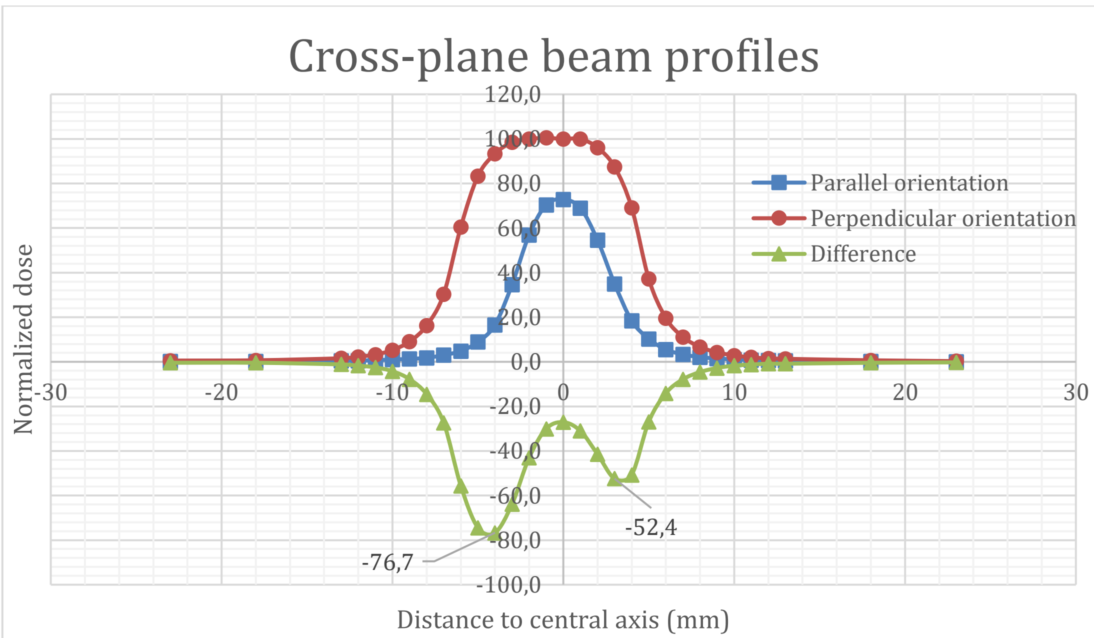

Figure 4.13 Cross-plane beam profiles for parallel and perpendicular orientation of a PTW 60019 synthetic single-crystal diamond detector in a 0.6 cm × 0.6 cm photon beam field size produced by a Siemens Oncor LINAC.

The percentage difference between the cross-plane beam profiles at distances -4 mm and +3 mm in the penumbra, shown in Figure 4.13, obtained using a PTW 60019 synthetic single-crystal diamond detector oriented parallel to the photon beam and perpendicular to the photon beam was found to be -76.7% and -52.4%, respectively. Figure 4.13 shows that more current was collected when the detector was orientated perpendicular to the beam than when it was orientated parallel to the beam.

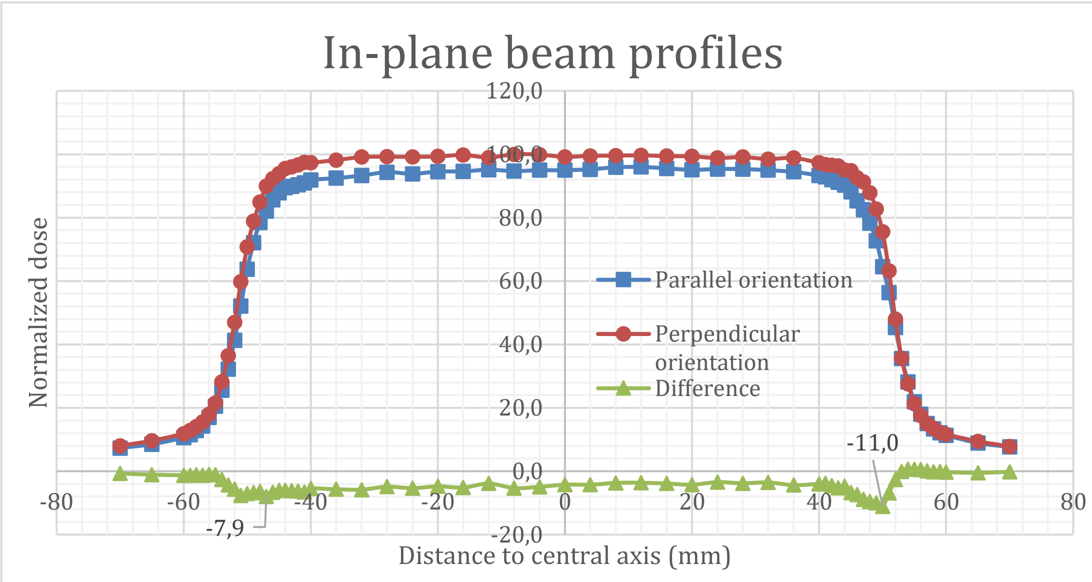

Figure 4.14 In-plane beam profiles for parallel and perpendicular orientation of a PTW 60019 synthetic single-crystal diamond detector in a 10 cm × 10 cm photon beam field size produced by a Siemens Oncor LINAC.

The percentage difference between the in-plane beam profiles at distances -47 mm and +50 mm in the penumbra, shown in Figure 4.14, obtained using a PTW 60019 synthetic single-crystal diamond detector oriented parallel to the photon beam and perpendicular to the photon beam was found to be -7.9% and -11.0%, respectively. Figure 4.14 shows that more current was collected in the central region when the chamber was orientated perpendicular to the beam than when it was orientated parallel to the beam.

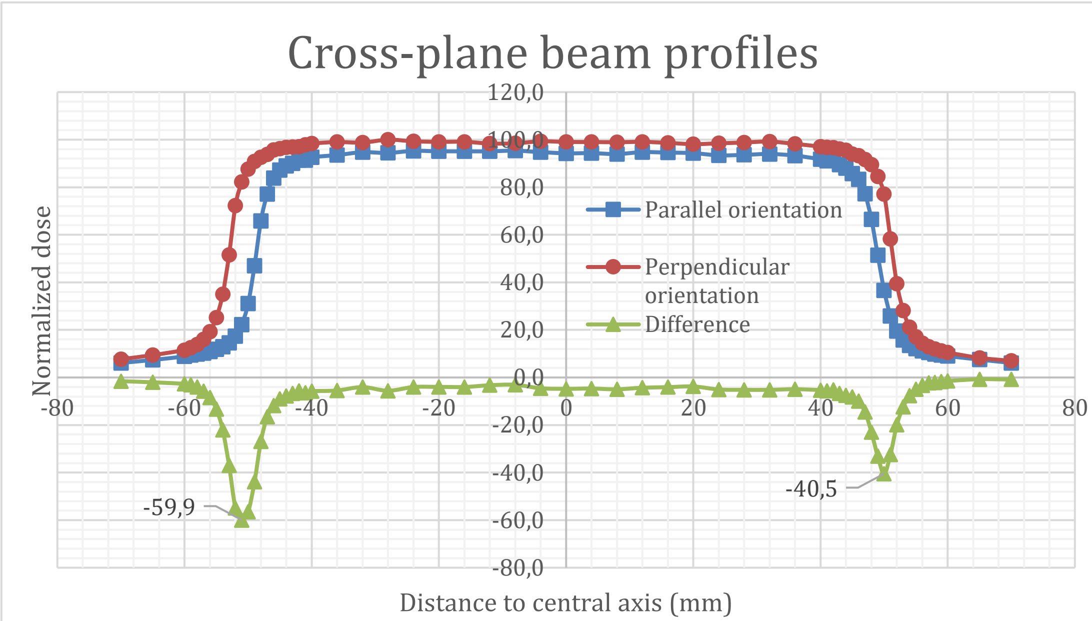

Figure 4.15 Cross-plane beam profiles for parallel and perpendicular orientation of a PTW 60019 synthetic single-crystal diamond detector in a 10 cm × 10 cm photon beam field size produced by a Siemens Oncor LINAC.

The percentage difference between the cross-plane beam profiles at distances -51 mm and +50 mm in the penumbra, shown in Figure 4.15, obtained using a PTW 60019 synthetic single-crystal diamond detector oriented parallel to the photon beam and perpendicular to the photon beam was found to be -59.9% and -40.5%, respectively. Figure 4.15 shows that more current was collected when the detector was orientated perpendicular to the beam than when it was orientated parallel to the beam.

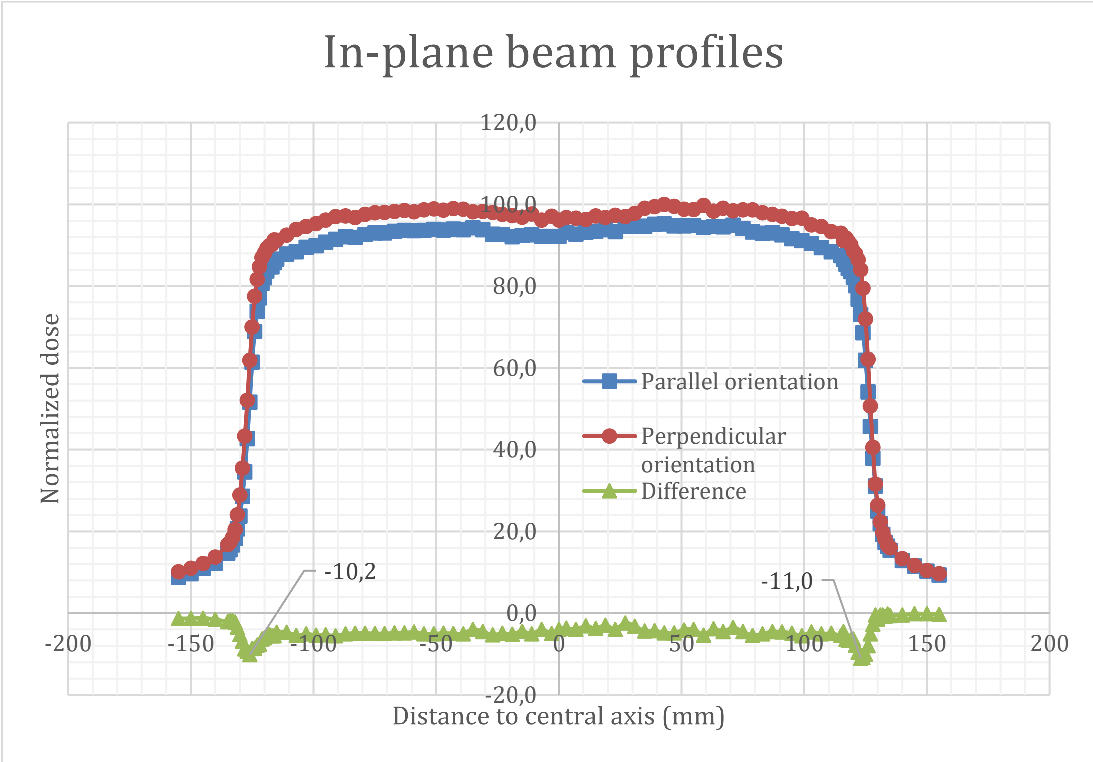

Figure 4.16 In-plane beam profiles for parallel and perpendicular orientation of a PTW 60019 synthetic single-crystal diamond detector in a 25 cm × 25 cm photon beam field size produced by a Siemens Oncor LINAC.

The percentage difference between the in-plane beam profiles at distances -126 mm and +123 mm in the penumbra, shown in Figure 4.16, obtained using a PTW 60019 synthetic single-crystal diamond detector oriented parallel to the photon beam and perpendicular to the photon beam was found to be -10.2% and -11.0%, respectively. Figure 4.16 shows that more current was collected in the central region when the chamber was orientated perpendicular to the beam than when it was orientated parallel to the beam.

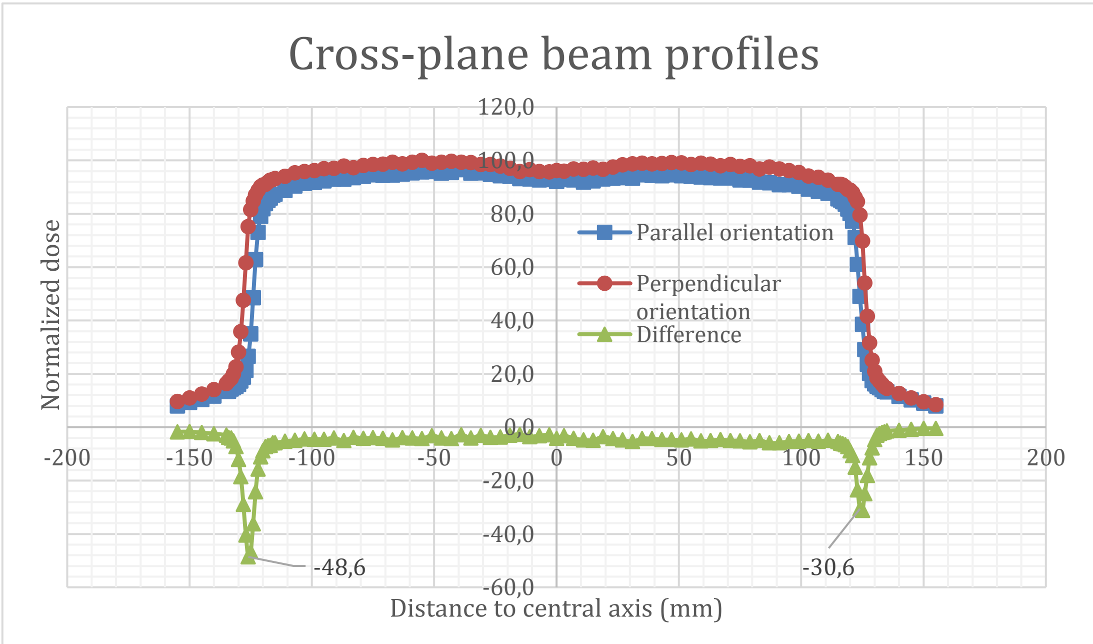

Figure 4.17 Cross-plane beam profiles for parallel and perpendicular orientation of a PTW 60019 synthetic single-crystal diamond detector in a 25 cm × 25 cm photon beam field size produced by a Siemens Oncor LINAC.

The percentage difference between the cross-plane beam profiles at distances -126 mm and +124 mm in the penumbra, shown in Figure 4.17, obtained using a PTW 60019 synthetic single-crystal diamond detector oriented parallel to the photon beam and perpendicular to the photon beam was found to be -48.6% and -30.6%, respectively. Figure 4.17 shows that more current was collected when the detector was orientated perpendicular to the beam than when it was orientated parallel to the beam.

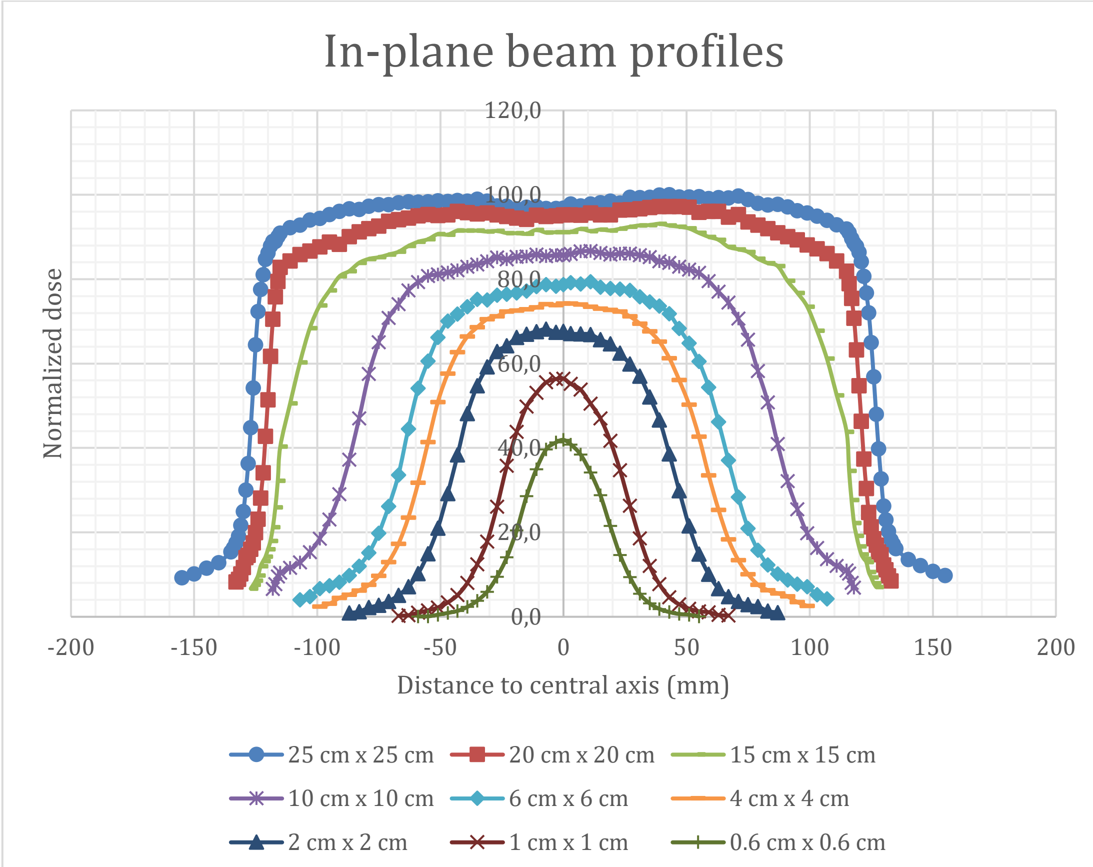

Figure 4.18 In-plane beam profiles for perpendicular orientation of a PTW 60019 synthetic single-crystal diamond detector in different field sizes produced by a Siemens Oncor LINAC.

Figure 4.18 shows that the amount of current collected by a detector decreases with decreasing field sizes. The in-plane beam profiles graphs, shown in Figure 4.18, for field sizes 0.6 cm x 0.6 cm and 1 cm x 1 cm are like a normal distribution curve.

4.2.3 Beam profiles obtained using a PTW 60019 synthetic single-crystal diamond detector irradiated by a photon beam produced an Elekta Versa HD LINAC.

The in-plane beam profile flatness and the cross-plane beam profile flatness obtained when the detector was oriented perpendicular to the beam was found to be 103.22 % and 104.53%, respectively. The in-plane beam profile symmetry and the cross-plane beam profile symmetry obtained when the detector was oriented perpendicular to the beam was found to be 100.37 % and 100.73%, respectively. The in-plane beam profile was found to have deviated by -0.01 mm from the CAX. Whereas the cross-plane beam profile was found to have deviated by -0.16 mm from the CAX. The in-plane beam profile flatness and the cross-plane beam profile flatness obtained when the detector was oriented parallel to the beam was found to be 104.06 % and 104.32%, respectively. The in-plane beam profile symmetry and the cross-plane beam profile symmetry obtained when the detector was oriented parallel to the beam was found to be 100.72 % and 100.49%, respectively. The in-plane beam profile was found to have deviated by -0.11 mm from the CAX. Whereas the cross-plane beam profile was found to have deviated by -0.11 mm from the CAX. The beam profiles for 1 cm x 1 cm, 2 cm x 2 cm, 4 cm x 4 cm and 15 cm x 15 cm are presented in APPENDIX C.

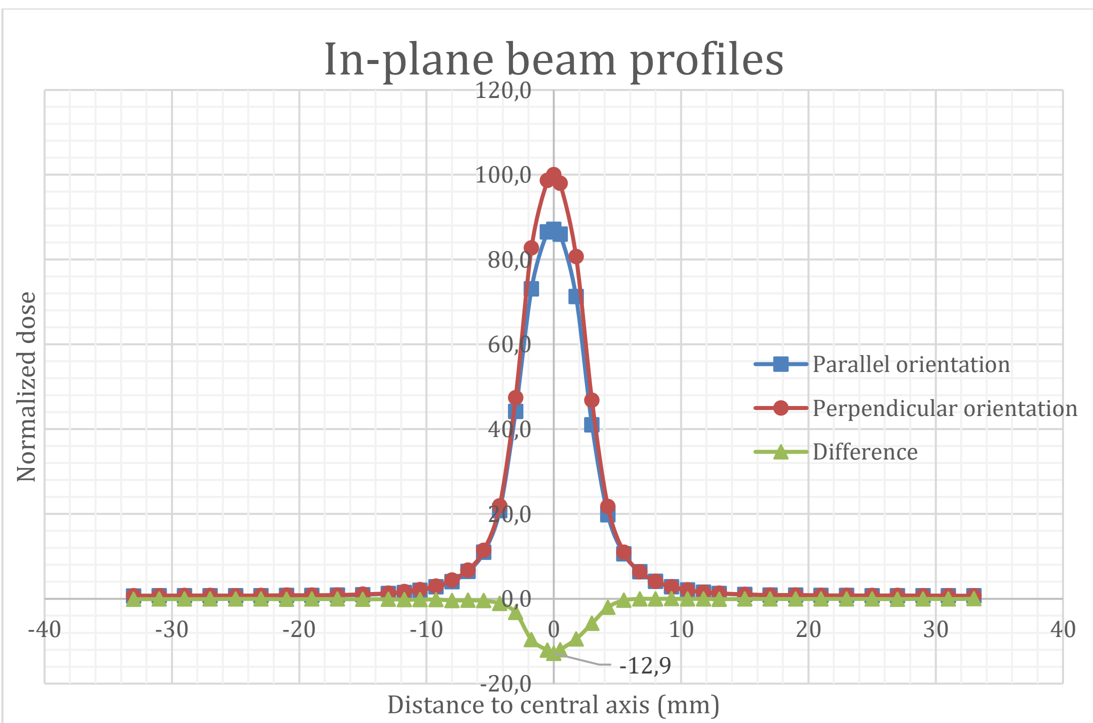

Figure 4.19 In-plane beam profiles for parallel and perpendicular orientation of a PTW 60019 synthetic single-crystal diamond detector in a 0.6 cm × 0.6 cm photon beam field size produced by an Elekta Versa HD LINAC.

The percentage difference between the in-plane beam profiles at the CAX, shown in Figure 4.19, obtained using a PTW 60019 synthetic single-crystal diamond oriented parallel to the photon beam and perpendicular to the photon beam was found to be -12.9%. Figure 4.19 shows that more current was collected when the detector was orientated perpendicular to the beam than when it was orientated parallel to the beam.

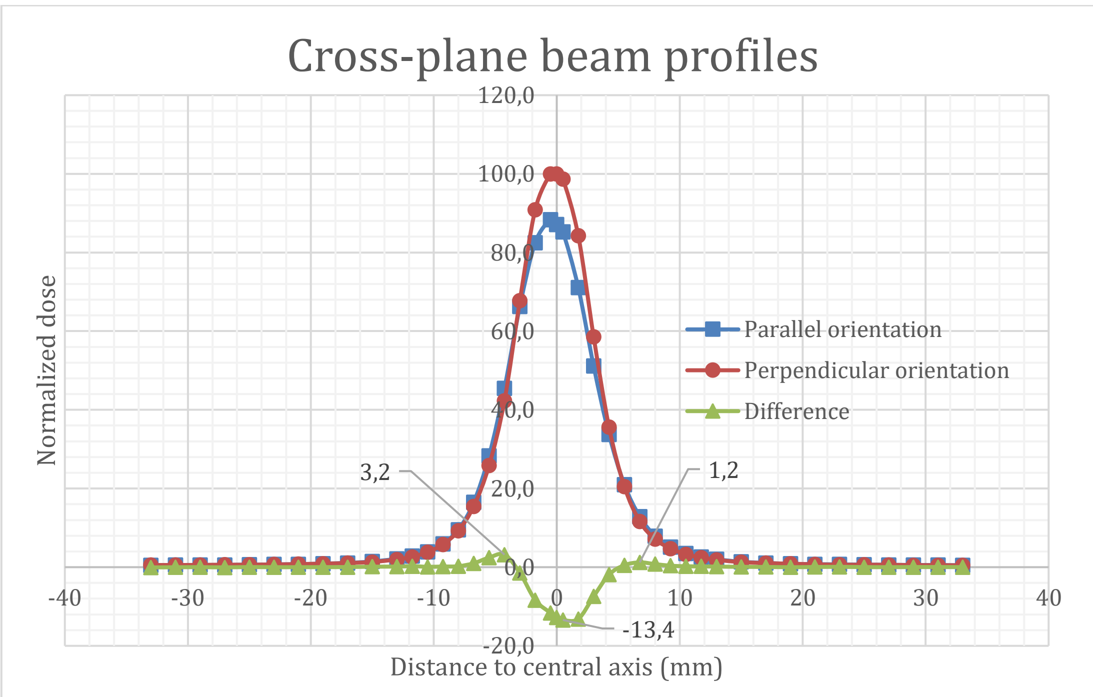

Figure 4.20 Cross-plane beam profiles for parallel and perpendicular orientation of a PTW 60019 synthetic single-crystal diamond detector in a 0.6 cm × 0.6 cm photon beam field size produced by an Elekta Versa HD LINAC.

The percentage difference between the in-plane beam profiles at distances +0.5 mm in the central region, shown in Figure 4.20, obtained using a PTW 60019 synthetic single-crystal diamond detector oriented parallel to the photon beam and perpendicular to the photon beam was found to be -13.4%. The percentage difference between the in-plane beam profiles at distances -4.25 mm and +6.75 mm in the penumbra was found to be 3.2% and 1.2%, respectively. Figure 4.20 shows that more current was collected in the central region when the chamber was orientated perpendicular to the beam than when it was orientated parallel to the beam. It also shows that a little more current was collected in the penumbra region when the chamber was orientated parallel to the beam than when it was orientated perpendicular to the beam.

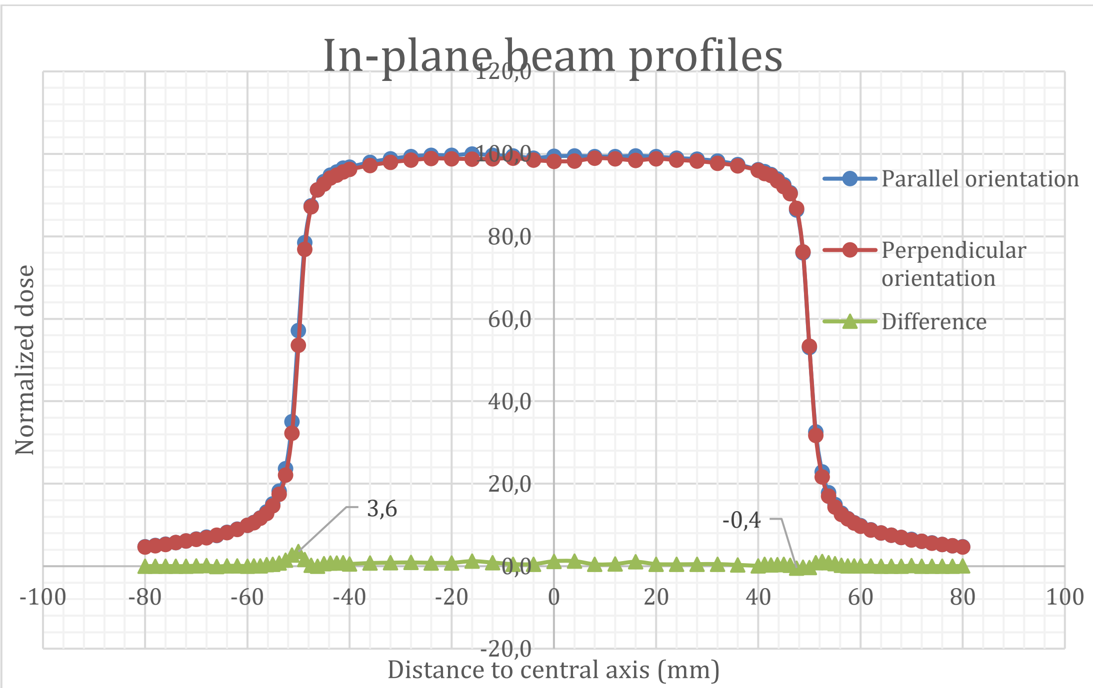

Figure 4.21 In-plane beam profiles for parallel and perpendicular orientation of a PTW 60019 synthetic single-crystal diamond detector in a 10 cm × 10 cm photon beam field size produced by an Elekta Versa HD LINAC.

The percentage difference between the in-plane beam profiles at distances -50 mm and +47.5 mm in the penumbra, shown in Figure 4.21, obtained using a PTW 60019 synthetic single-crystal diamond detector oriented parallel to the photon beam and perpendicular to the photon beam was found to be +3.6% and -0.4%, respectively.

Figure 4.21 shows that more current was collected in the central region when the detector was orientated parallel to the beam than when it was orientated perpendicular to the beam.

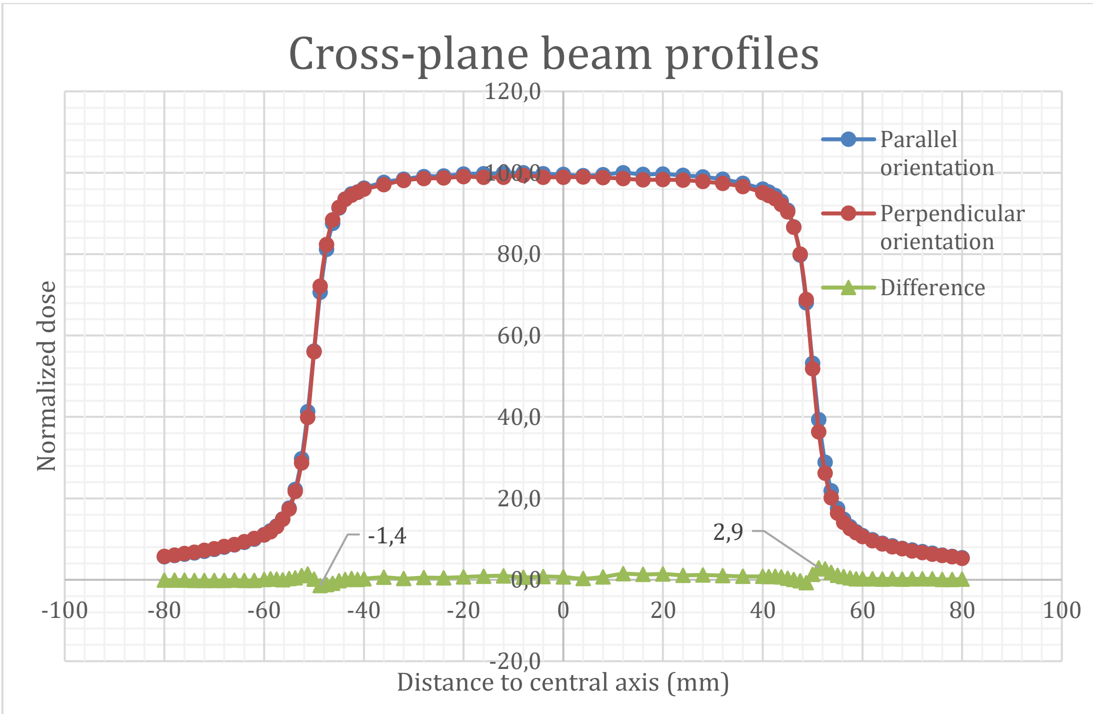

Figure 4.22 Cross-plane beam profiles for parallel and perpendicular orientation of a PTW 60019 synthetic single-crystal diamond detector in a 10 cm × 10 cm photon beam field size produced by an Elekta Versa HD LINAC.

The percentage difference between the in-plane beam profiles at distances -48.75 mm and +51.25 mm in the penumbra, shown in Figure 4.22, obtained using a PTW 60019 synthetic single-crystal diamond detector oriented parallel to the photon beam and perpendicular to the photon beam was found to be -1.4% and +2.9%, respectively. Figure 4.22 shows that more current was collected in the central region when the detector was orientated parallel to the beam than when it was orientated perpendicular to the beam.

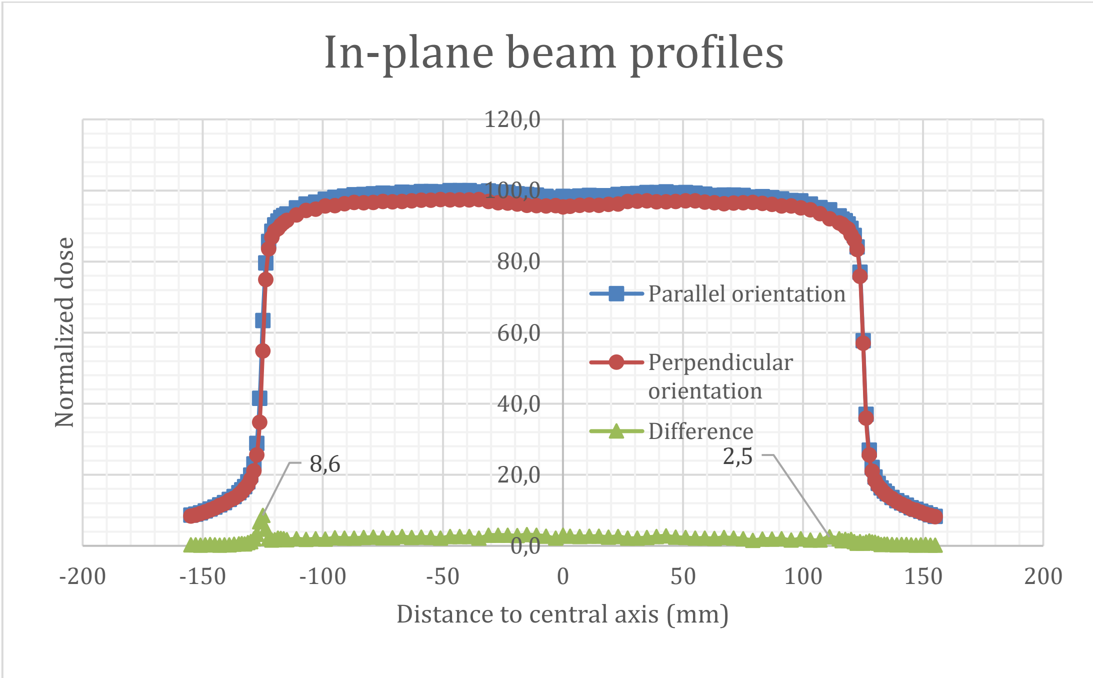

Figure 4.23 In-plane beam profiles for parallel and perpendicular orientation of a PTW 60019 synthetic single-crystal diamond detector in a 25 cm × 25 cm photon beam field size produced by an Elekta Versa HD LINAC.

The percentage difference between the in-plane beam profiles at distances -125 mm and +111 mm in the penumbra, shown in Figure 4.23, obtained using a PTW 60019 synthetic single-crystal diamond detector oriented parallel to the photon beam and perpendicular to the photon beam was found to be +8.6% and +2.5%, respectively. Figure 4.23 shows that more current was collected when the detector was orientated parallel to the beam than when it was orientated perpendicular to the beam.

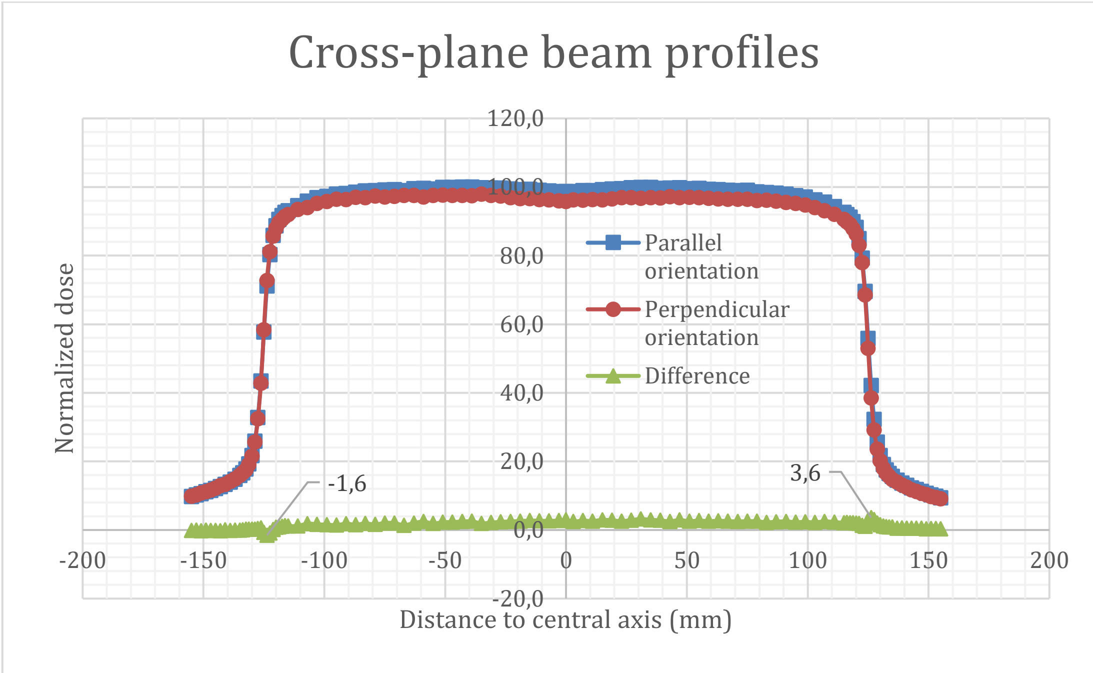

Figure 4.24 Cross-plane beam profiles for parallel and perpendicular orientation of a PTW 60019 synthetic single-crystal diamond detector in a 25 cm × 25 cm photon beam field size produced by an Elekta Versa HD LINAC.

The percentage difference between the in-plane beam profiles at distances -123.75 mm and +126.25 mm in the penumbra, shown in Figure 4.24, obtained using a PTW 60019 synthetic single-crystal diamond detector oriented parallel to the photon beam and perpendicular to the photon beam was found to be -1.6% and +3.6%, respectively. Figure 4.24 shows that more current was collected in the central region when the detector was orientated parallel to the beam than when it was orientated perpendicular to the beam.

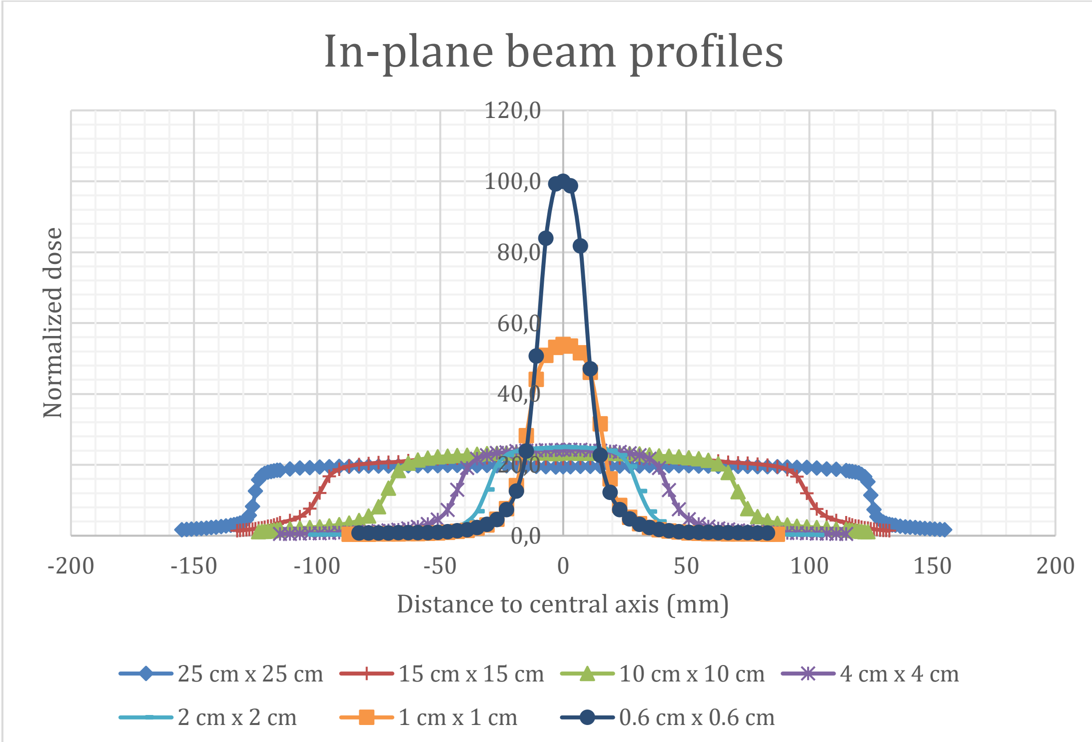

Figure 4.25 In-plane beam profiles for perpendicular orientation of a PTW 60019 synthetic single-crystal diamond detector in different field sizes produced by an Elekta Versa HD LINAC.

Figure 4.25 shows that the amount of current collected by a detector increases with decreasing field sizes.

4.3 Percentage depth dose results

Table 4.7 Depth of dose maximum obtained using a PTW 30013 Farmer ionisation chamber irradiated with a photon beam produced by an Elekta Versa HD LINAC.

Geometric field size (cm)	0.6	1	2	4	6	10	15	25
Depth of dose maximum (cm)	1.6	1.6	1.8	1.8	1.7	1.6	1.6	1.5

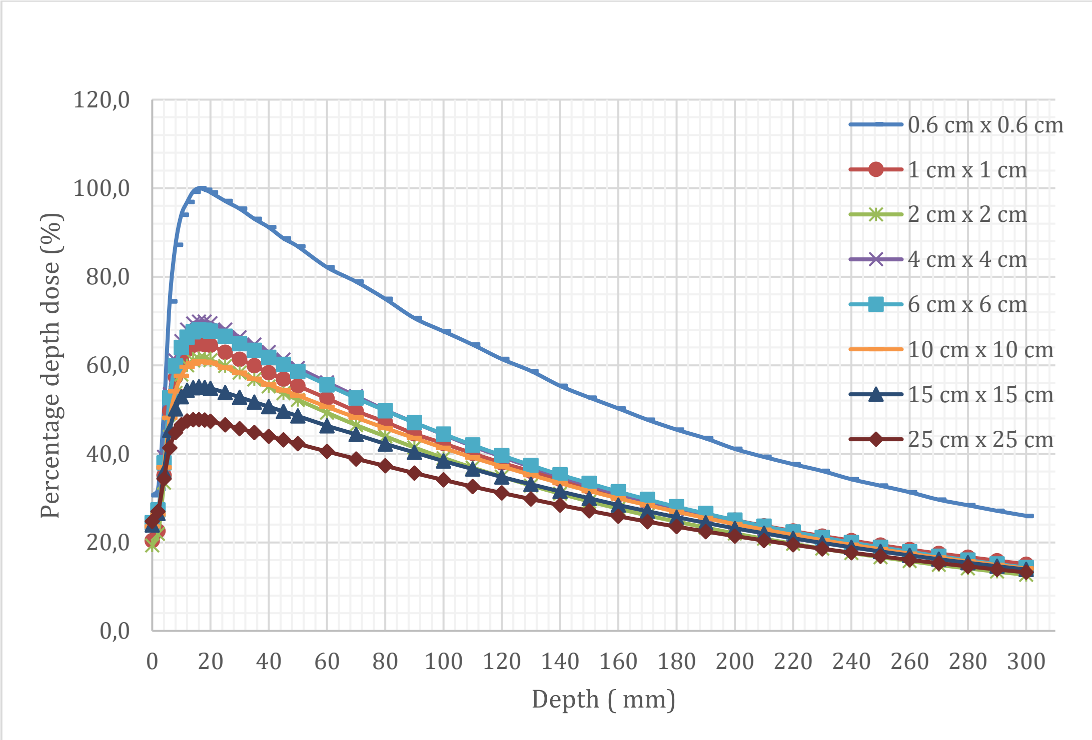

Figure 4.26 Percentage depth doses obtained using a PTW 30013 Farmer ionisation chamber irradiated with a photon beam produced by an Elekta Versa HD LINAC.

The percentage depth doses, shown in Figure 4.26, obtained are all different to each other. Figure 4.26 shows that the percentage depth dose obtained in a 0.6 cm x 0.6 cm field size is an outlier. Table 4.7 shows the depth of dose maximum for all the percentage depth doses.

Table 4.8 Depth of dose maximum obtained using a PTW 60019 synthetic single-crystal diamond detector irradiated with a photon beam produced by an Elekta Versa HD LINAC.

Geometric field size (cm)	2	4	6	10	15	25
Depth of dose maximum (cm)	1.5	1.6	1.5	1.5	1.4	1.3

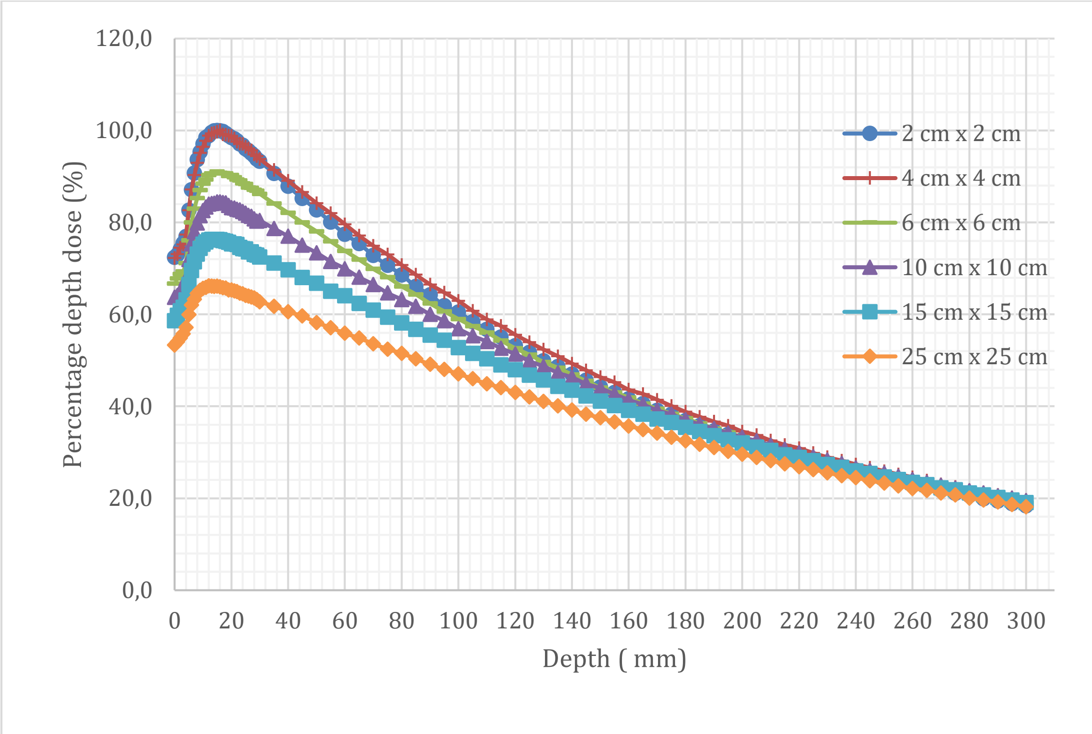

Figure 4.27 Percentage depth doses obtained using a PTW synthetic single-crystal diamond detector irradiated with a photon beam produced by an Elekta Versa HD LINAC.

The percentage depth doses, shown in Figure 4.27, obtained are all different to each other. Table 4.8 shows the depth of dose maximum for all the percentage depth doses.

4.4 Geometric field sizes and irradiation field sizes results

Table 4.9 Geometric field sizes and irradiation field sizes obtained using a PTW 31010 semi-flex ionisation chamber and a PTW 60019 synthetic single-crystal diamond detector irradiated with a photon beam produced by a Siemens Oncor LINAC.

Geometric field size (cm)			0.6	1	2	4	6	10	15	20	25
PTW 31010		Perpendicular orientation	1.05	1.37	2.33	4.32	6.32	10.15	15.19	20.31	25.22

semi-flex ionisation chamber	Irradiation field size (cm)	Parallel orientation	1.06	1.17	2.09	4.10	6.10	10.12	15.10	20.10	25.11
PTW 60019 synthetic single-crystal diamond detector	Irradiation field size (cm)	Perpendicular orientation	1.04	1.42	2.41	4.41	6.41	10.41	15.42	20.44	25.46
		Parallel orientation	0.77	1.12	2.08	4.09	6.08	10.07	15.08	20.07	25.10

The irradiation field sizes were calculated using equation (2.19). Table 4.9 shows that there is a difference between the geometric field sizes and the measured irradiation field sizes.

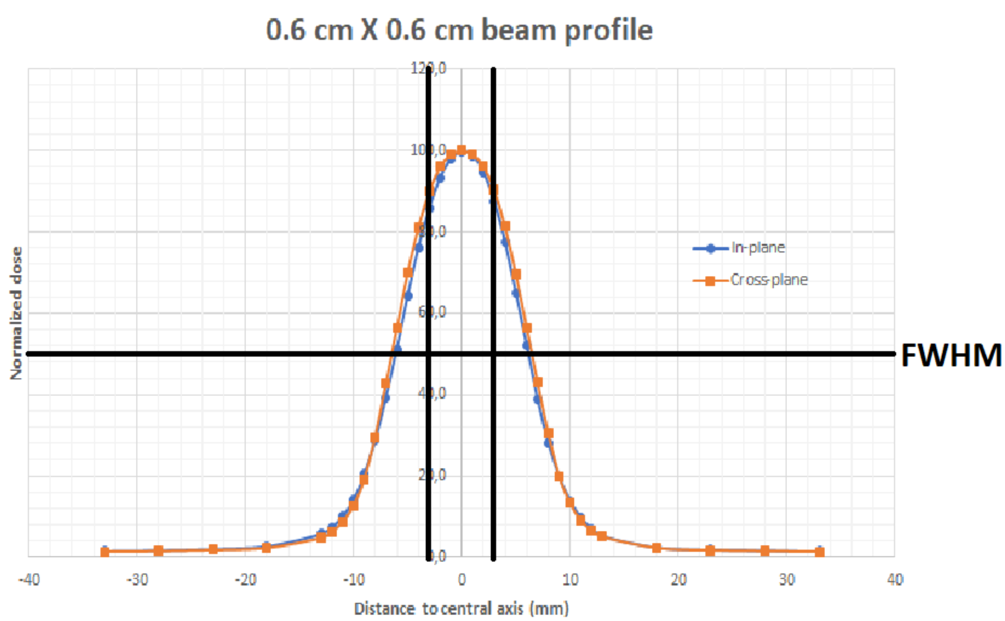

Figure 4.28 Comparison between a 0.6 cm X 0.6 cm geometric field size and an irradiation field size obtained using a PTW 31010 semi-flex ionisation chamber oriented parallel to the beam.

The two thick vertical lines, shown in Figure 4.28, represent the geometric field size and the thick horizontal line represent the FWHM of the beam profile. The points where the horizontal line intersect with the beam profiles were used to calculate the irradiation field size. Figure 4.28 shows that the geometric field size is smaller than the irradiation field size.

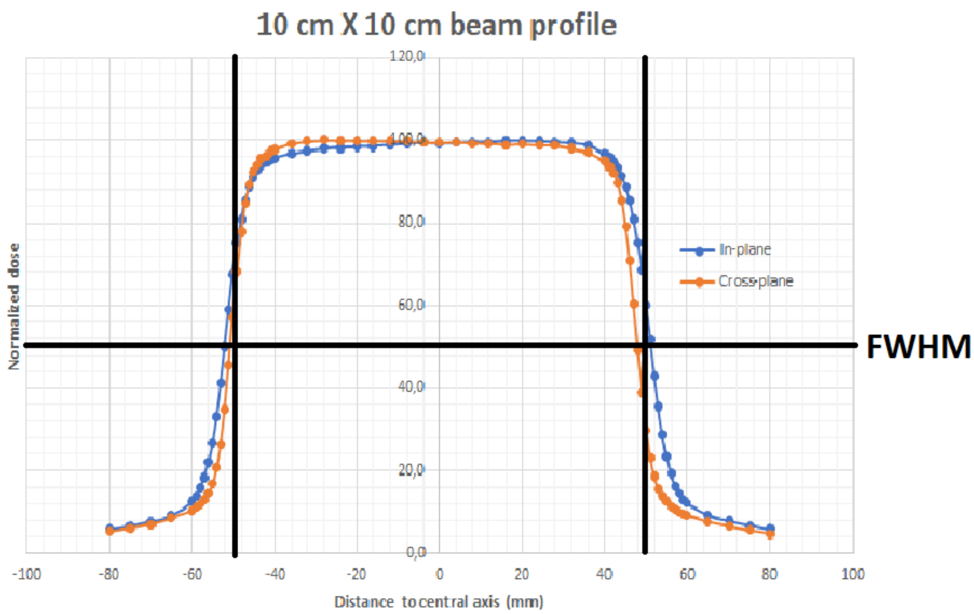

Figure 4.29 Comparison between a 10 cm X 10 cm geometric field size and an irradiation field size obtained using a PTW 31010 semi-flex ionisation chamber oriented parallel to the beam.

Figure 4.29 shows that there is a small difference between the geometric field size and irradiation field size. The length of the geometric field along the in-plane is smaller than the length of the irradiation field along the in-plane. Thus, the geometric field size is smaller than the irradiation field size. Similar results were observed for all larger field sizes and when using both the PTW 31010 semi-flex ionisation chamber and the PTW 60019 synthetic single-crystal diamond detector.

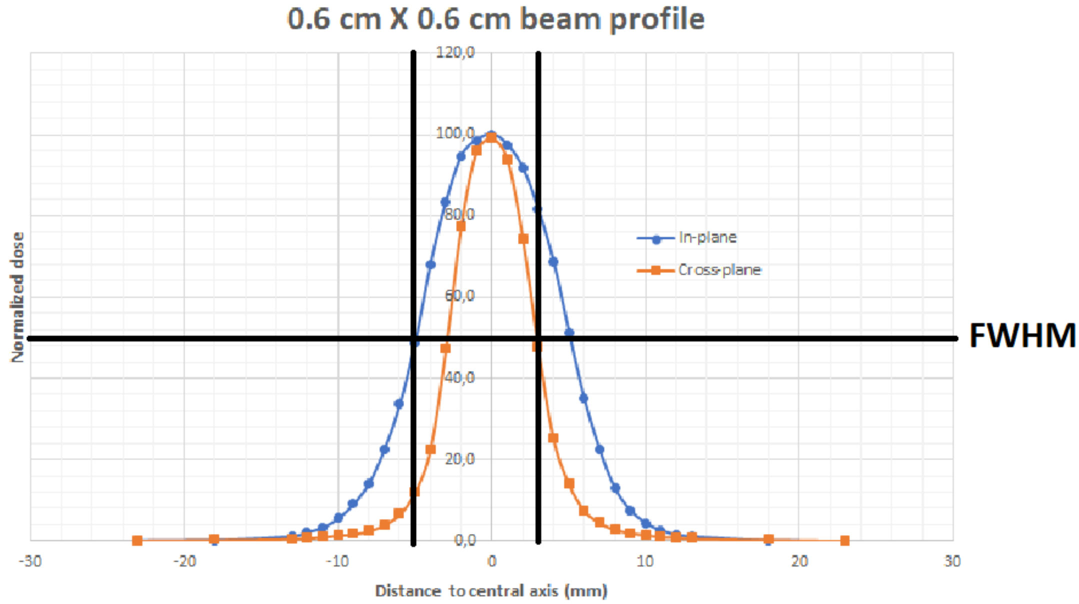

Figure 4.30 Comparison between a 0.6 cm X 0.6 cm geometric field size and an irradiation field size obtained using a PTW 60019 synthetic single-crystal diamond detector oriented parallel to the beam.

Figure 4.30 shows that there is a difference between the geometric field size and irradiation field size. The length of the geometric field along the cross-plane is larger than the length of the irradiation field along the cross-plane. However, the length of the geometric field along the in-plane is smaller than the length of the irradiation field along the in-plane. Thus, the geometric field size is smaller than the irradiation field size.

Table 4.10 Geometric field sizes and irradiation field sizes obtained using a PTW 60019 synthetic single-crystal diamond detector and a PTW 30013 Farmer ionisation chamber irradiated with a photon beam produced by an Elekta Versa HD LINAC.

	Geometric field size (cm)		0.6	1	2	4	10	15	25
PTW 60019		Perpendicular orientation	0.65	1.02	2.03	4.06	10.06	15.07	25.11

synthetic single-crystal diamond detector	Irradiation field size (cm)	Parallel orientation	0.68	1.08	2.04	4.06	10.07	15.08	25.13
PTW 30013 Farmer ionisation chamber	Irradiation field size (cm)	Perpendicular orientation	1.48	1.62	2.28	4.13	10.17	15.20	25.28

Table 4.10 shows that there is a difference between the geometric field sizes and measured irradiation field sizes.

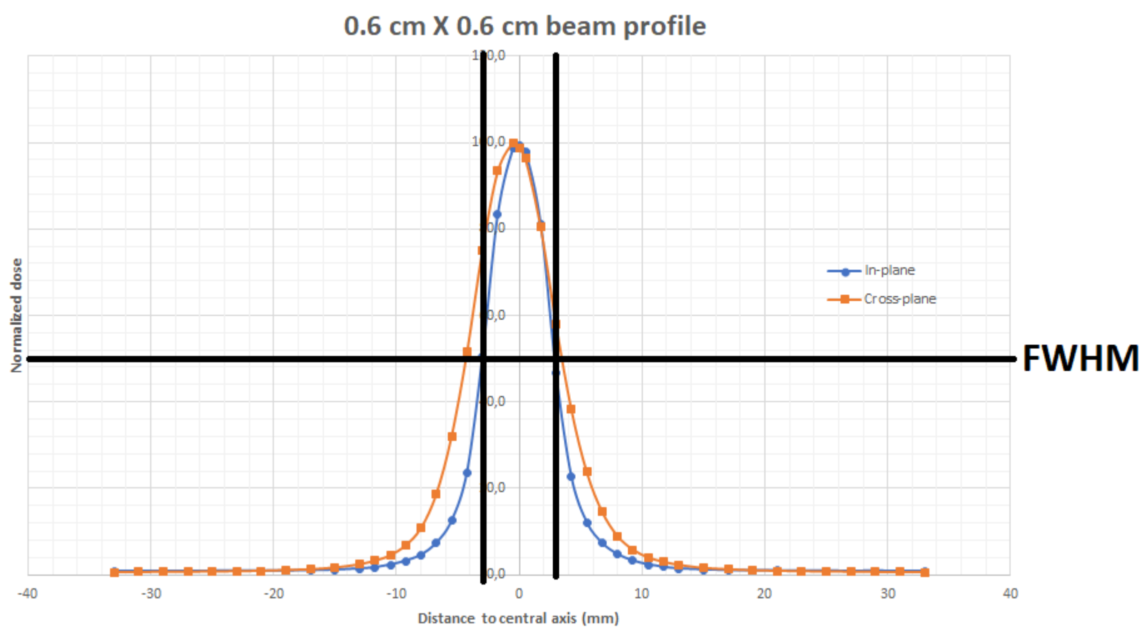

Figure 4.31 Comparison between a 0.6 cm X 0.6 cm geometric field size and an irradiation field size obtained using a PTW 60019 synthetic single-crystal diamond detector oriented parallel to the beam produced by an Elekta Versa HD LINAC.

Figure 4.31 shows that there is a small difference between the geometric field size and irradiation field size. The length of the geometric field along the in-plane is equal to the length of the irradiation field along the in-plane. However, the length of the geometric field along the cross-plane is smaller than the length of the irradiation field along the cross-plane. Thus, the geometric field size is smaller than the irradiation field size.

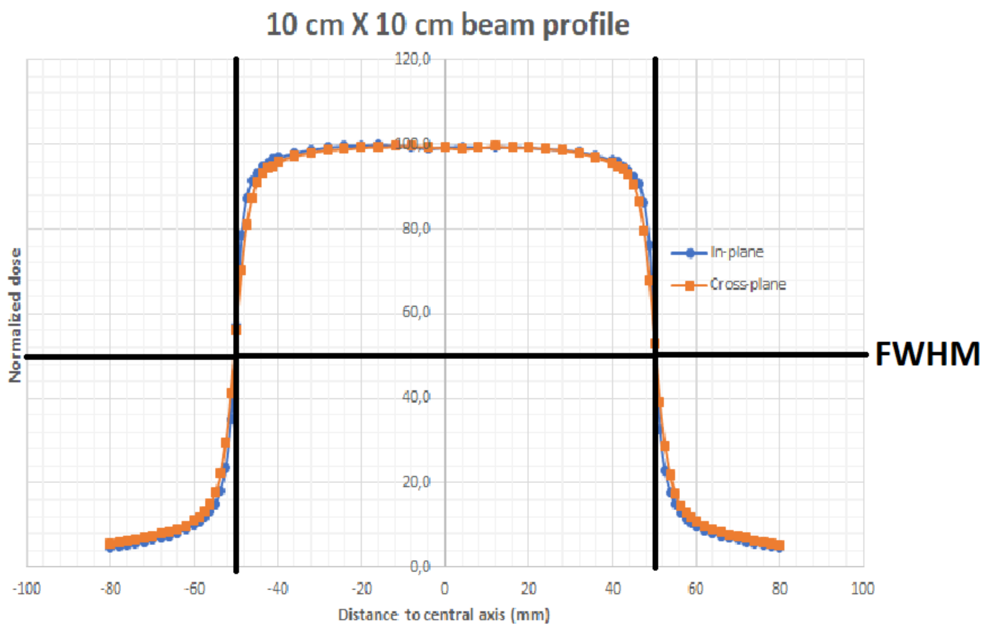

Figure 4.32 Comparison between a 10 cm X 10 cm geometric field size and an irradiation field size obtained using a PTW 60019 synthetic single-crystal diamond detector oriented parallel to the beam produced by an Elekta Versa HD LINAC.

Figure 4.32 does not show any difference between the geometric field size and the irradiation field size. However, Table 4.10 shows that there is a small difference between a 10 cm X 10 cm geometric field size and the irradiation field size. Similar results were observed for all larger field sizes.

4.5 Output factor results

Table 4.11 Output factors obtained using a PTW 30013 Farmer ionisation chamber, a PTW 31010 semi-flex ionisation chamber and a PTW 60019 synthetic single-crystal diamond detector irradiated with a photon beam produced by a Siemens Oncor LINAC.

Geometric field size (cm)		0.6	1	2	4	6	10	15	20	25
Irradiation field size (cm)		0.77	1.12	2.08	4.09	6.08	10.07	15.08	20.07	25.10
PTW 30013 Farmer ionisation chamber		0.26	0.43	0.73	0.86	0.92	1	1.06	1.10	1.13
PTW 31010 semi-flex ionisation chamber	Perpendicular orientation	0.51	0.66	0.78	0.85	0.91	1	1.06	1.10	1.13
	Parallel orientation	0.52	0.67	0.79	0.86	0.92	1	1.06	1.10	1.13
PTW 60019 synthetic single-crystal diamond detector	Perpendicular orientation	0.63	0.72	0.80	0.87	0.92	1	1.06	1.10	1.13
	Parallel orientation	0.62	0.72	0.80	0.86	0.92	1	1.06	1.10	1.13

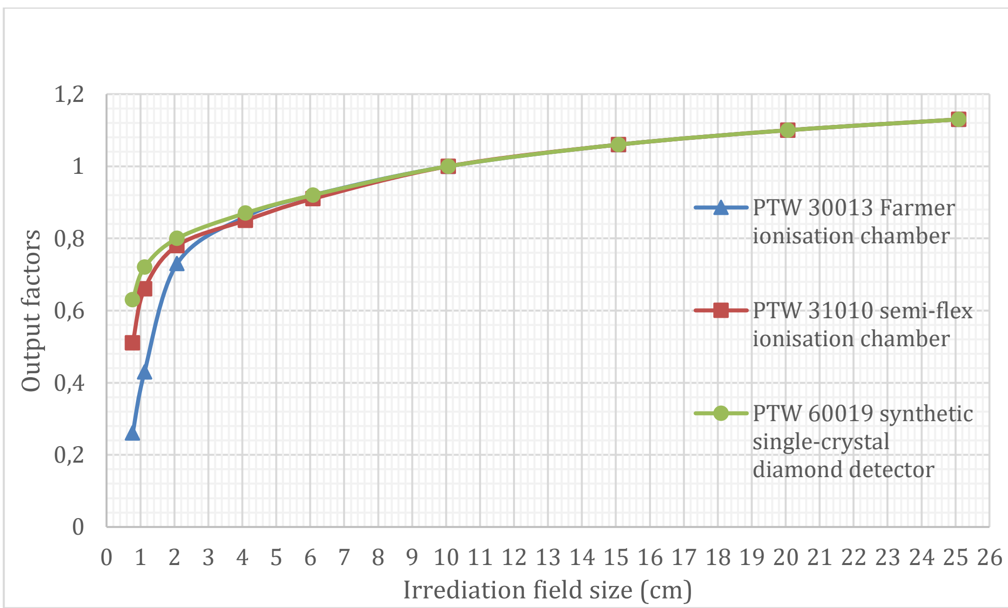

Figure 4.33 Output factors obtained using a PTW 30013 Farmer ionisation chamber, PTW 31010 semi-flex ionisation chamber and PTW 60019 synthetic single-crystal diamond detector orientated perpendicular to the beam produced by a Siemens Oncor LINAC.

Output factors were calculated using equation (2.22). Six charge values obtained at a depth of 10 cm were recorded for each field size. The average of charge readings for each field size was used to calculate the output factors. The output factors, shown in Table 4.11, increases with increasing field size. The PTW 30013 Farmer ionisation chamber obtained small output factors compared to output factors obtained by the PTW 31010 semi-flex ionisation chamber and the PTW 60019 synthetic single-crystal diamond detector. The PTW 60019 synthetic single-crystal diamond detector obtained large output factors compared to output factors obtained by the PTW 31010 semi-flex ionisation chamber and the 30013 Farmer ionisation chamber. Figure 4.33 shows that the output factors obtained by the chambers are the same for field sizes greater than 10 cm x 10 cm.

Table 4.12 Output factors obtained using a PTW 30013 Farmer ionisation chamber, a PTW 31010 semi-flex ionisation chamber and a PTW 60019 synthetic single-crystal diamond detector irradiated with a photon beam produced by an Elekta Versa HD LINAC.

Geometric field size (cm)		0.6	1	2	4	6	10	15	20	25
Irradiation field size (cm)		0.65	1.02	2.03	4.06	-	10.06	15.07	-	25.11
PTW 30013 Farmer ionisation chamber		0.14	0.31	0.65	0.87	0.93	1	1.06	1.10	1.12
PTW 31010 semi-flex ionisation chamber	Perpendicular orientation	0.29	0.56	0.79	0.88	0.93	1	1.06	1.10	1.12
	Parallel orientation	0.33	0.59	0.79	0.88	0.93	1	1.06	1.10	1.12
PTW 60019 synthetic single-crystal diamond detector	Perpendicular orientation	0.47	0.68	0.80	0.88	0.93	1	1.06	1.10	1.12
	Parallel orientation	0.48	0.68	0.80	0.88	0.93	1	1.06	1.10	1.12

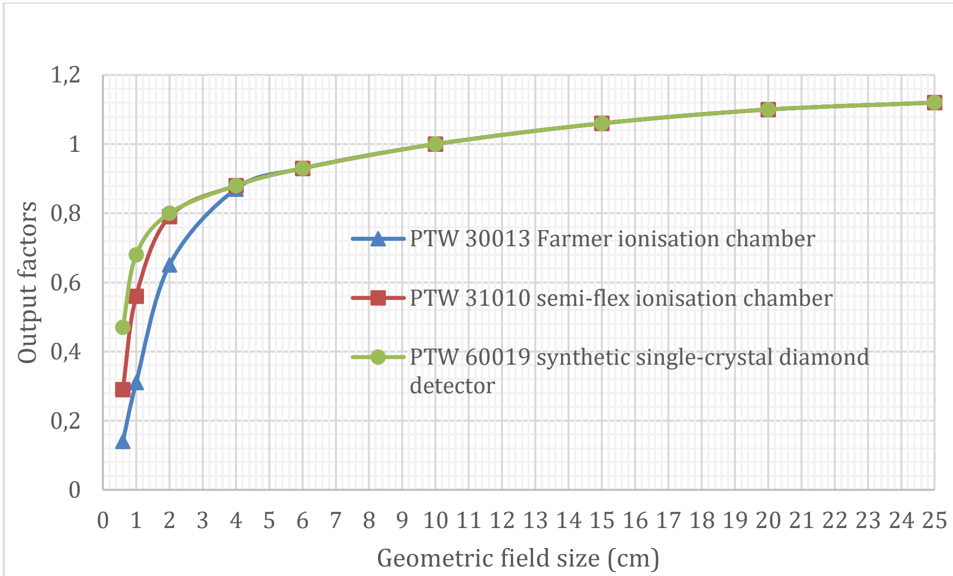

Figure 4.34 Output factors obtained using a PTW 30013 Farmer ionisation chamber, PTW 31010 semi-flex ionisation chamber and PTW 60019 synthetic single-crystal diamond detector orientated perpendicular to the beam produced by an Elekta Versa HD LINAC.

The output factors, shown in Table 4.12, increases with increasing field size. The PTW 30013 Farmer ionisation chamber obtained small output factors compared to output factors obtained by the PTW 31010 semi-flex ionisation chamber and the PTW 60019 synthetic single-crystal diamond detector. The PTW 60019 synthetic single-crystal diamond detector obtained large output factors compared to output factors obtained by the PTW 31010 semi-flex ionisation chamber and the PTW 30013 Farmer ionisation chamber. Figure 4.34 shows that the output factors obtained by the chambers are the same for field sizes greater than 4 cm x 4 cm.

CHAPTER 5
DISCUSSION

5.1 Introduction

This study investigates the dependence of the signal measured by a detector on the irradiation field size, orientation of the detector to the beam and material of the sensitive volume. The study also investigate which detector is suitable for small field dosimetry.

5.2 Range of charged particles results discussion

The range of charged particles results indicate that the signal measured by a detector depends on the orientation of a detector to the beam. The results obtained with detectors irradiated with a photon beam produced by a Siemens Oncor LINAC suggest that the tissue phantom ratio is 0.57. Whereas the results obtained with detectors irradiated with a photon beam produced by an Elekta Versa HD LINAC suggest that the tissue phantom ratio is 0.68. The findings of similar studies by (Diteko et al., 2020; Sharma, 2008) agrees with the results obtained with detectors irradiated with a photon beam produced by an Elekta Versa HD LINAC. The results suggest that the beam quality of the Siemens Oncor LINACs had deteriorated when the data was collected, eight months before the Siemens Oncor LINACs were replaced with Elekta Versa HD LINACs.

The results obtained with detectors irradiated with a photon beam produced by a Siemens Oncor LINAC indicate that the ranges of charged particles is 0.4 cm. Whereas, the results obtained with detectors irradiated with a photon beam produced by an Elekta Versa HD LINAC indicate that the ranges of charged particles is 1.3 cm. The definition of small fields described by (Alfonso et al., 2008; Das, Ding and Ahnesjö, 2007; International Atomic Energy Agency, 2017) implies that beam field sizes smaller than 0.4 cm x 0.4 cm produced by a Siemens Oncor LINAC are small fields. The definition of small fields also implies that beam field sizes smaller than 1.3 cm x 1.3 cm produced by an Elekta Versa HD LINAC are small fields

The results indicate that the ranges of charged particles obtained with detectors irradiated with a photon beam produced by a Siemens Oncor LINAC is smaller than the dimensions of the sensitive volume of a PTW 30013 Farmer ionisation chamber and a PTW 31010 semi-flex ionisation chamber. Whereas, the results indicate that the ranges of charged particles obtained with detectors irradiated with a photon beam produced by an Elekta Versa HD LINAC is smaller than the sensitive volume length of a PTW 30013 Farmer ionisation chamber but larger than the sensitive volume diameter of the detector. The Bragg-Gray cavity theory by (Bragg, 1912; Gray, 1936) suggest that a sensitive volume of a PTW 30013 Farmer ionisation chamber and a PTW 31010 semi-flex ionisation chamber does not behave as a Bragg-Gray cavity in a photon beam produced by a Siemens Oncor LINAC. This implies that these detectors are not suitable to be used in relative dosimetry if they are irradiated with a photon beam with a similar beam quality as the Siemens Oncor LINAC used in this study.

5.3 Beam profile results discussion

The beam profile results indicate that the signal measured by a detector depends on the orientation of a detector to the beam and the radiation beam field size. The results suggest that as field size are increased the detectors collect more current, thus resulting in beam profile getting larger. The 0.6 cm x 0.6 cm to 6 cm x 6 cm beam profiles obtained with a PTW 31010 semi-flex ionisation chamber irradiated with a photon beam produced by a Siemens Oncor LINAC indicate an underestimation of the signal at the CAX and overestimation of the signal at the penumbra. The analysis of the beam profiles and volume averaging effect of (Wuerfel, 2013) implies that as the detector averages the signal over its volume, the signal varies over the sensitive volume of the detector. Whereas beam profiles obtained with a PTW 60019 synthetic single-crystal diamond detector does not show volume averaging effect, this agrees with the claims of (Wuerfel, 2013) that a detector with a smaller sensitive volume yield a different signal. The comparison of beam profiles obtained with a PTW 60019 synthetic single-crystal diamond detector irradiated with a photon beam produced by a Siemens Oncor LINAC and irradiated with a photon beam produced by an Elekta Versa HD LINAC provides an insight that a detector would measure a different signal if the beam quality is not the same for the LINACs.

5.4 Percentage depth dose results discussion

The percentage depth dose results indicate that the signal measured by a detector depends on the radiation beam field size. The percentage depth dose results concur with the findings of (Pasquino et at., 2016; Ciancaglioni et at., 2012).

5.5 Output factor results discussion

The beam profile results indicate that the signal measured by a detector depends on the orientation of a detector to the beam, size of the sensitive volume and the radiation beam field size. Output factors obtained using a PTW 60019 synthetic single-crystal diamond detector are larger than output factors obtained using ionisation chambers, this suggest that output factors obtained with radiation detectors with smaller sensitive volume and tissue-equivalent sensitive material have high spatial resolution. The results suggest that a PTW 30013 Farmer ionisation chamber is not suitable for small field dosimetry. The results also show that this is independent of the beam quality of a LINAC. The findings of similar studies by (Pasquino et at., 2016; Ciancaglioni et at., 2012; Cranmer-Sargison et al, 2013; Das et al, 2000) agrees with the output factor results.

5.6 Limitations of the study

The choice of detectors used to investigate the behaviour of radiation detectors in various field sizes was limited to the radiation detectors available at Charlotte Maxeke Johannesburg Academic Hospital. There is no detector holder available that can hold a PTW 30013 Farmer ionisation chamber parallel to the beam, therefore the detector was not used to investigate whether a signal obtained depends on the orientation of a detector. Due to the lack of radiation detectors with the same sensitive volume size and different sensitive volume material, the results cannot confirm whether the signal measured by a detector depends on the material of the sensitive volume of a detector.

CHAPTER 6
CONCLUSION AND RECOMMENDATIONS

This research aimed to determine if the signal measured by a detector depends on the irradiation field size, orientation of the detector to the beam and material of the sensitive volume. The research also aimed to determine which detector is suitable for small field dosimetry. Based on the analysis of the results, it can be concluded that the signal of a detector depends on the orientation of the detector to the beam and irradiation field size. It can also be concluded that a PTW 60019 synthetic single-crystal diamond detector is suitable for performing small field dosimetry.

The research clearly illustrates that the beam quality influence the signal obtained by a detector and show that some detectors becomes unsuitable to be used in relative dosimetry if the beam quality has deteriorated to a low quality. This raises the question of whether a beam quality range should be considered as a factor that describes the suitability a detector for radiation dosimetry.

Based on this conclusions, Medical Physicists should consider using a PTW 60019 synthetic single-crystal diamond detector for small field dosimetry. They should consider using the detector oriented parallel to the beam. They should consider measuring the tissue phantom ratio when they are measuring the consistency of the beam output. They must compare the beam quality they get to the beam quality that is found in literature for the relevant beam energy.

Further research is needed to determine the effect of sensitive volume material on the response of the detector. The research should use detectors with the same detector sensitive volume.

REFERENCES

Abbas, Z. and Rehman, S., 2020. An Overview of Cancer Treatment Modalities. [online] Available at: http://dx.doi.org/10.5772/intechopen.76558 [Accessed 24 Jun 2020].

Alfonso, R., Andreo, P., Capote, R., Huq, M.S., Kilby, W., Kjäll, P., Mackie, T.R., Palmans, H., Rosser, K., Seuntjens, J. and Ullrich, W. 2008. A new formalism for reference dosimetry of small and nonstandard fields. Medical Physics, vol. 35, No. 11, pp. 5179-5186.

Almond, P.R., Biggs, P.J., Coursey, B.M., Hanson, W.E, Huq, M.S., Nath, R. and Rogers, D.W.O., 1999. AAPM's TG-51 protocol for clinical reference dosimetry of high-energy photon and electron beams. Medical Physics, vol. 26, No. 9, pp. 1847-1870.

Attix, F.H., De La Vergne, L., and Ritz, V.H., 1958. Cavity ionisation as a function of wall material. J. Res. NBS., vol. 60, no. 3, pp. 235.

Boutillon, M. and Perroche-Roux, A.M., 1987. Re-evaluation of the W value for electrons in dry air. Physics in Medicine and Biology, vol. 32, no. 2, pp. 213-219.

Bragg, W.H., 1912. Studies in radioactivity. New York: Macmillan.

Ciancaglioni, I., Marinelli, M., Milani, E., Prestopino, G., Verona, C., Verona-Rinati, G., Consorti, R., Petrucci, A., and De Notaristefani, F., 2012. Dosimetric characterization of a synthetic single-crystal diamond in clinical radiation therapy small photon beams. Medical Physics, vol. 40, No. 7, Part 1, pp. 4493 – 4501.

Cranmer-Sergison, G., Charles, P.H., Trapp, J.V., and Thwaites, D.I., 2013. A methological approach to reporting corrected small field relative outputs. Radiotherapy and Oncology, vol. 109, No. 3, pp. 350-355.

Das, I.J, Ding, G.X., and Ahnesjö, A., 2007. Small fields: Nonequilibrium radiation dosimetry. Medical Physics, vol. 35, No. 1, pp. 206-215.

Das, I.J, Downes, M.B, Kassaee, A, and Tochner, Z, 2000. Choice of Radiation Detector in Dosimetry of Stereotactic Radiosurgery-Radiotherapy. Journal of Radiosurgery, vol. 3, No. 4, pp. 177-186.

Diteko, K., Mkhize, T.D., and Mohlapholi M.S., 2020. Validating the percentage depth dose using two different phantom materials. Journal of Medical Physics and Applied Sciences, vol. 5, No. 1, pp. 7.

Di Venanzio, C., Marinelli, M., Milani, E., Prestopino, G., Verona, C., Verona-Rinati, G., Falco, M., Bagalà, P., Santoni, R. and Pimpinella, M., 2013. Characterization of a synthetic single-crystal diamond Schottky diode for radiotherapy electron beam dosimetry. Medical Physics, vol. 40, No. 2, p. 021712.

Eklund, K. and Ahnesjö, A., 2008. Fast modelling of spectra and stopping-power ratios using differentiated fluence pencil kernels. Physics in Medicine and Biology, vol. 53, No. 16, pp. 4231-4247.

Gray, L.H., 1936. An ionisation method for the absolute measurement of gamma-ray energy. Proc. R. Soc., vol. A156, pp 578.

Haryanto, F., Fippel, M., Laub, W., Dohm, O., and Nüsslin, F., 2002. Investigation of photon beam output factors for conformal radiation therapy—Monte Carlo simulations and measurements. Physics in Medicine and Biology, vol. 47, No. 11, pp. N133-N143.

Hei, L.F., Zhao, Y., Wei, J. J., Liu, J. L., Li, C. M., Tang, W. Z., and Lu, F.X., 2016. Interface features of the HPHT Ib substrate and homoepitaxial CVD diamond layer. Diamond and Related Materials, vol. 69, pp. 33-39.

International Atomic Energy Agency, 2017. Dosimetry of Small Static Fields Used in External Beam Radiotherapy: An IAEA-AAPM International Code of Practice For Reference And Relative Dose Determination / International Atomic Energy Agency. Technical Reports Series No. 483. Vienna: International Atomic Energy Agency.

International Atomic Energy Agency, 2000. Absorbed dose determination in external beam radiotherapy: An international code of practice for dosimetry based on standards of absorbed dose to water. Technical Reports Series No. 398. Vienna: International Atomic Energy Agency.

International Commission on Radiation Units and measurements, 2011. Fundamental quantities and units for ionizing radiation (Revised). International Commission on Radiation Units and measurements Report No. 85. Journal of the International Commission on Radiation Units and measurements, vol. 11, No. 1.

Khan, M.F., 1994. The Physics of Radiation Therapy. Baltimore: Williams and Wilkins.

Pasquino M., Cutaia C., Radici L., Valzano S., Gino E., Cavedon C., and Stasi M., 2016. Dosimetric characterization and behaviour in small X-ray fields of a microchamber and a plastic scintillator detector. [online] Available at: https://doi.org/10.1259/bjr.20160596 [Accessed 30 My 2018].

Patatoukas, G., Kalavrezos, P., Seimenis, I., Dilvoi, M., Kouloulias, V., Efstathopoulos, E. and Platoni, K., 2018. Determination of beam profile characteristics in radiation therapy using different dosimetry set ups. [online] Available at: https://jbuon.com/archive/23-5-1448.pdf [Accessed 21 July 2020].

Podgorsak, E.B., 2005. Radiation Oncology Physics. Vienna: International Atomic Energy Agency.

Ptw.de., 2018. Bl&aumltterkatalog. [online] Available at: https://ww.ptw.de/fileadmin/data/download/satalogviewer/DETECTORS_Cat_en_16522900_11/blaetterkatalog/index.html#page_24 [Accessed 9 Dec 2018].

Sharma, S., 2008. Quality of high-energy X-ray radiotherapy beams: Issues of adequacy of routine experimental verification. Journal of Medical Physics, vol. 33, No. 1, pp. 1.

Sánchez-Doblado, F., Andreo, P., Capote, R., Leal, A., Perucha, M., Arráns, R., Núñez, L., Mainegra, E., Lagares, J.I., and Carrasco, E. 2003. Ionisation chamber dosimetry of small photon fields: a Monte Carlo study on stopping-power ratios for radiosurgery and IMRT beams. Physics in Medicine and Biology, vol. 48, No. 14, pp. 2081-2099.

Spencer, L.V., and Attix, F.H., 1955. A theory of cavity ionisation. Radiation Research., vol. 3, no. 3. pp. 239-0254.

Wuerfel, J.U., 2013. Dose measurements in small fields. Medical Physics International Journal, vol. 1, No. 1, pp. 81-90.

Beam profiles obtained using a PTW 31010 semi-flex ionisation chamber irradiated by a photon beam produced a Siemens Oncor LINAC

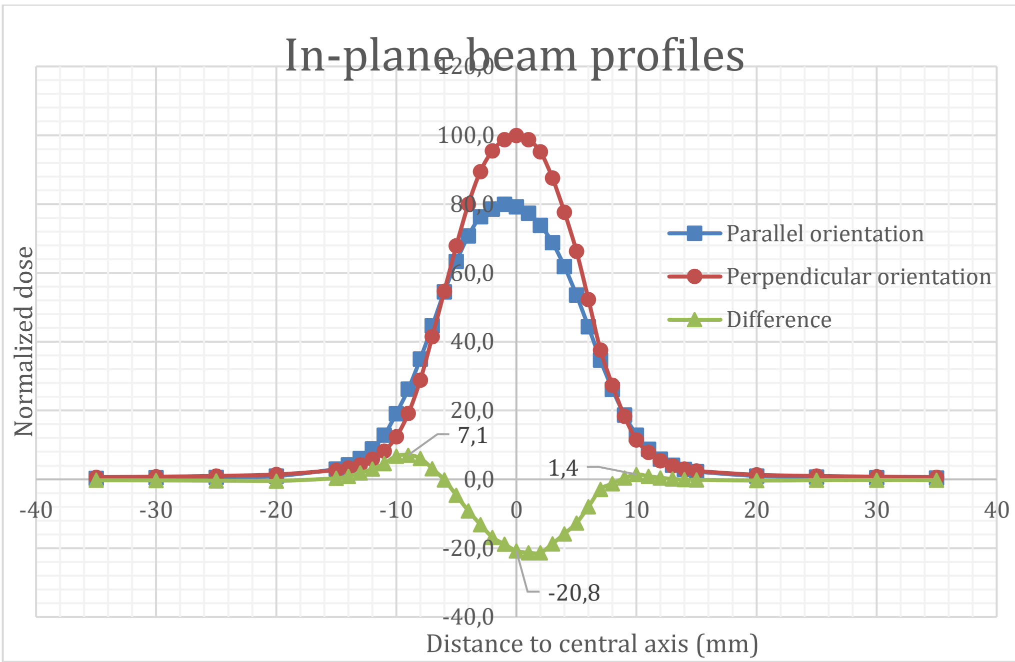

Figure A1 In-plane beam profiles for parallel and perpendicular orientation of a PTW 31010 semi-flex ionisation chamber in a 1 cm × 1 cm photon beam field size produced by a Siemens Oncor LINAC.

The percentage difference between the in-plane beam profiles at the CAX of the beam, shown in Figure A1, obtained using a PTW 31010 semi-flex ionisation chamber oriented parallel to the photon beam and perpendicular to the photon beam was found to be -20.8%. The percentage difference between the in-plane beam profiles at distances -9 mm and +10 mm in the penumbra was found to be 7.1% and 1.4%, respectively. Figure A1 shows that more current was collected in the central region when the chamber was orientated perpendicular to the beam than when it was orientated parallel to the beam. It also shows that more current was collected in the penumbra region when the chamber was orientated parallel to the beam than when it was orientated perpendicular to the beam.

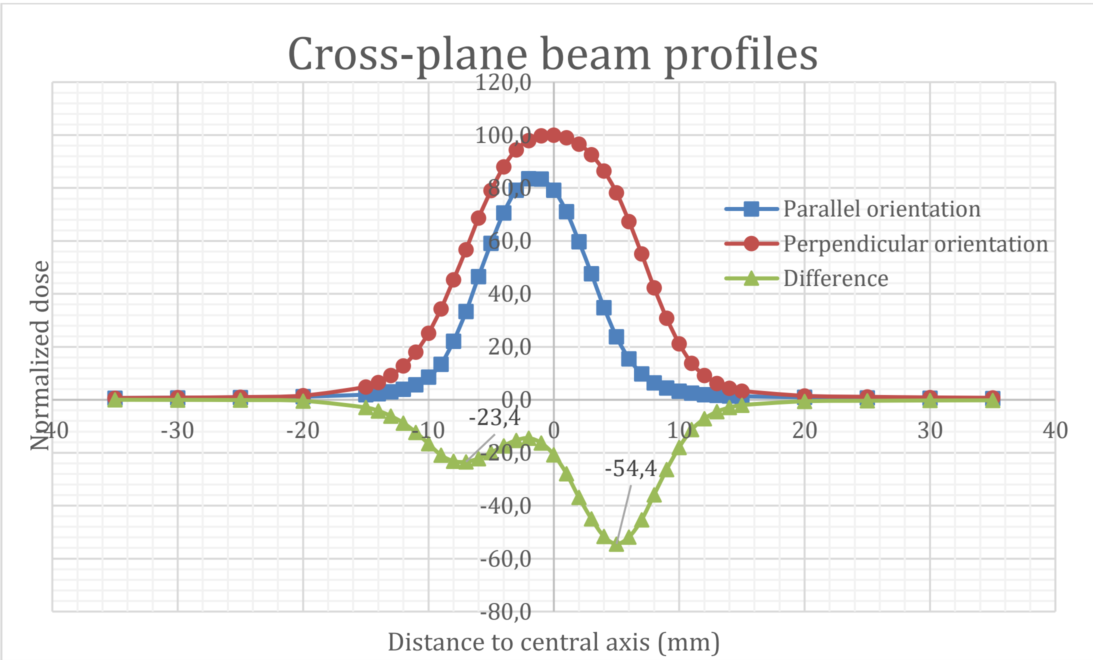

Figure A2 Cross-plane beam profiles for parallel and perpendicular orientation of a PTW 31010 semi-flex ionisation chamber in a 1 cm × 1 cm photon beam field size produced by a Siemens Oncor LINAC.

The percentage difference between the cross-plane beam profiles at distances -7 mm and +5 mm in the penumbra, shown in Figure A2, obtained using a PTW 31010 semi-flex ionisation chamber oriented parallel to the photon beam and perpendicular to the photon beam was found to be -23.4% and -54.4%, respectively. Figure A2 shows that more current was collected when the chamber was orientated perpendicular to the beam than when it was orientated parallel to the beam along the cross-plane.

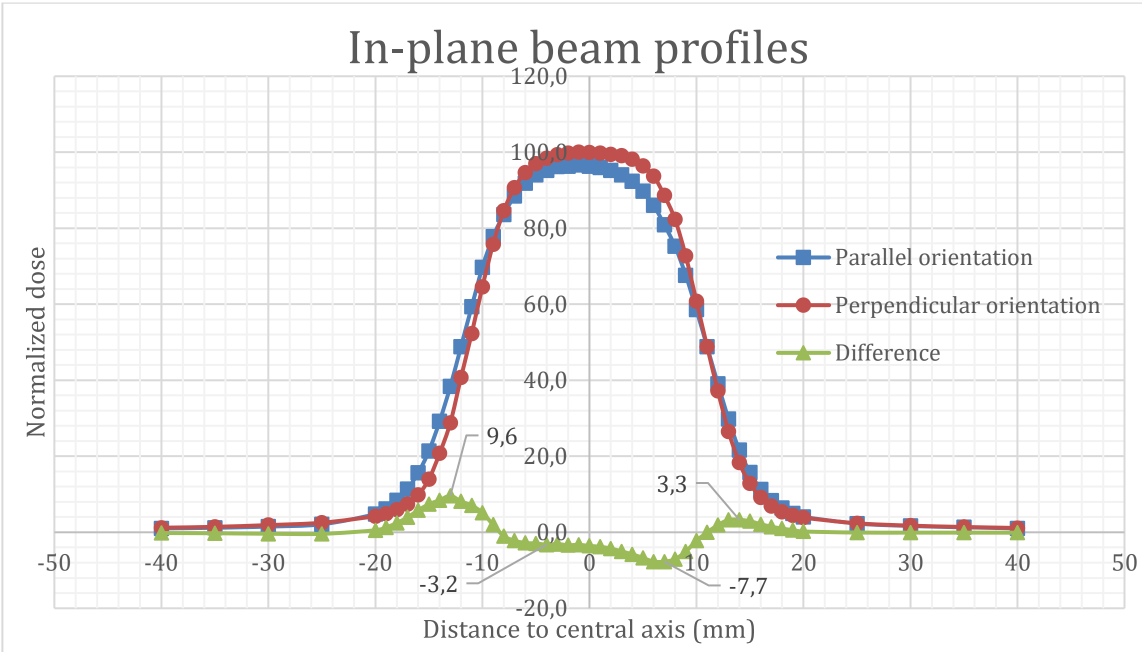

Figure A3 In-plane beam profiles for parallel and perpendicular orientation of a PTW 31010 semi-flex ionisation chamber in a 2 cm × 2 cm photon beam field size produced by a Siemens Oncor LINAC.

The percentage difference between the in-plane beam profiles at distances -4 mm and +7 mm in the central region, shown in Figure A3, obtained using a PTW 31010 semi-flex ionisation chamber oriented parallel to the photon beam and perpendicular to the photon beam was found to be -3.2% and -7.7%, respectively. The percentage difference between the in-plane beam profiles at distances -13 mm and +14 mm in the penumbra was found to be 9.6% and 3.3%, respectively. Figure A3 shows that more current was collected in the central region when the chamber was orientated perpendicular to the beam than when is orientated parallel to the beam. It also shows that more current was collected in the penumbra region when the chamber was orientated parallel to the beam than when it was orientated perpendicular to the beam.

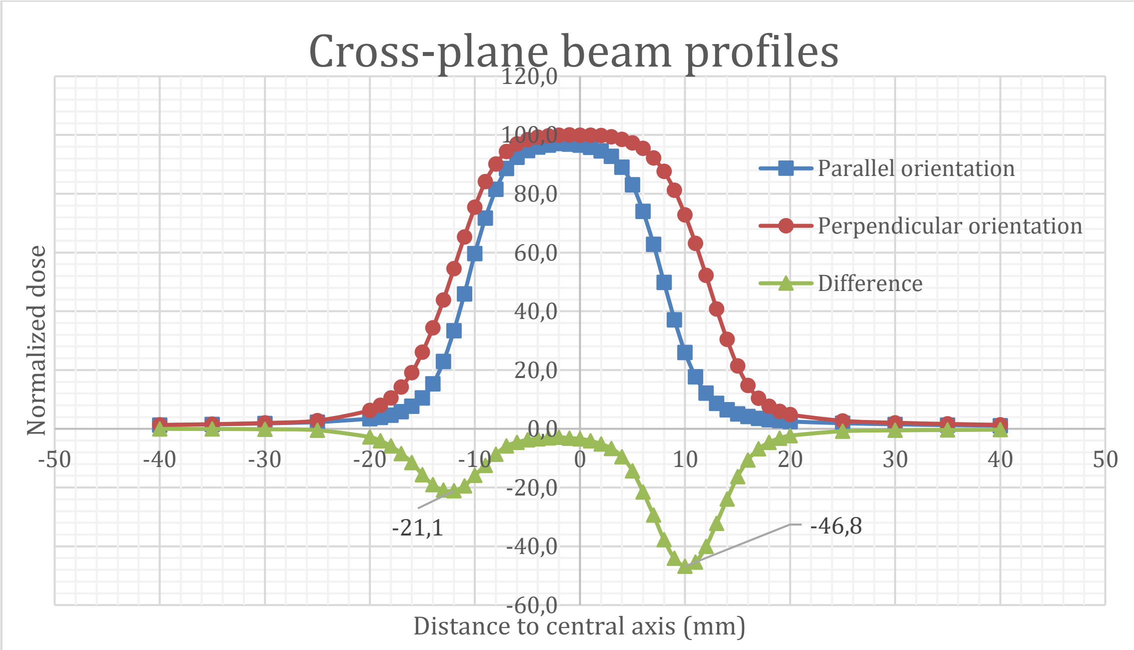

Figure A4 Cross-plane beam profiles for parallel and perpendicular orientation of a PTW 31010 semi-flex ionisation chamber in a 2 cm × 2 cm photon beam field size produced by a Siemens Oncor LINAC.

The percentage difference between the cross-plane beam profiles at distances -12 mm and +10 mm in the penumbra, shown in Figure A4, obtained using a PTW 31010 semi-flex ionisation chamber oriented parallel to the photon beam and perpendicular to the photon beam was found to be -21.1% and -46.8%, respectively. Figure A4 shows that more current was collected when the chamber was orientated perpendicular to the beam than when it was orientated parallel to the beam along the cross-plane.

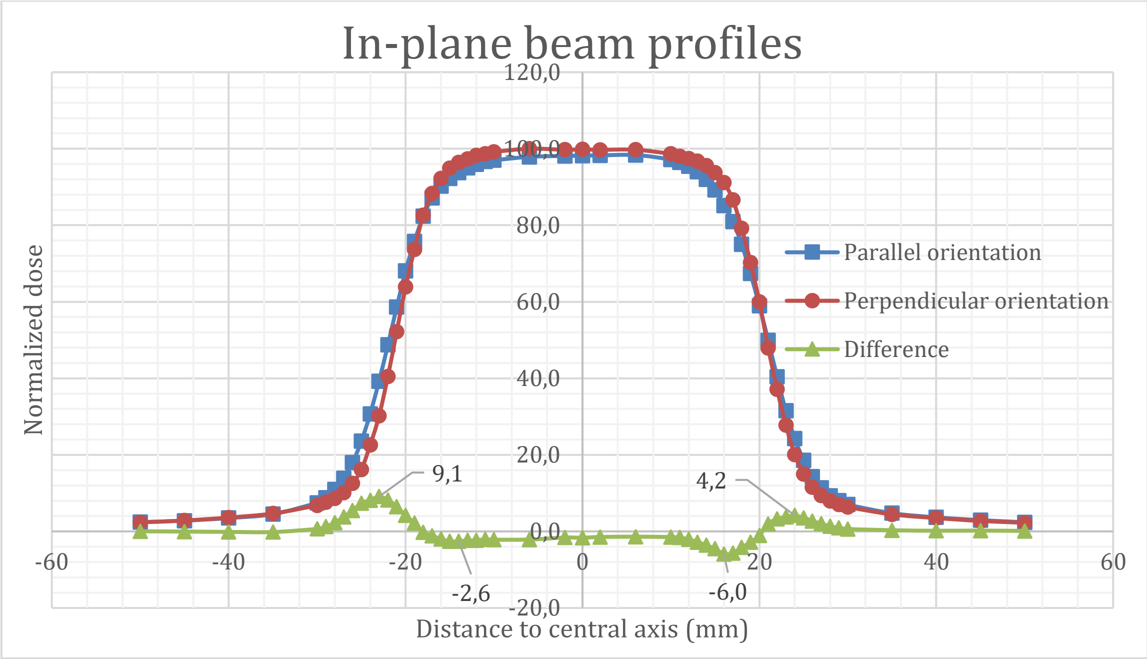

Figure A5 In-plane beam profiles for parallel and perpendicular orientation of a PTW 31010 semi-flex ionisation chamber in a 4 cm × 4 cm photon beam field size produced by a Siemens Oncor LINAC.

The percentage difference between the in-plane beam profiles at distances -14 mm and +16 mm in the central region, shown in Figure A5, obtained using a PTW 31010 semi-flex ionisation chamber oriented parallel to the photon beam and perpendicular to the photon beam was found to be -2.6% and -6.0%, respectively. The percentage difference between the in-plane beam profiles at distances -23 mm and +24 mm in the penumbra was found to be 9.1% and 4.2%, respectively. Figure A5 shows that more current was collected in the central region when the chamber was orientated perpendicular to the beam than when is orientated parallel to the beam. It also shows that more current was collected in the penumbra region when the chamber was orientated parallel to the beam than when it was orientated perpendicular to the beam.

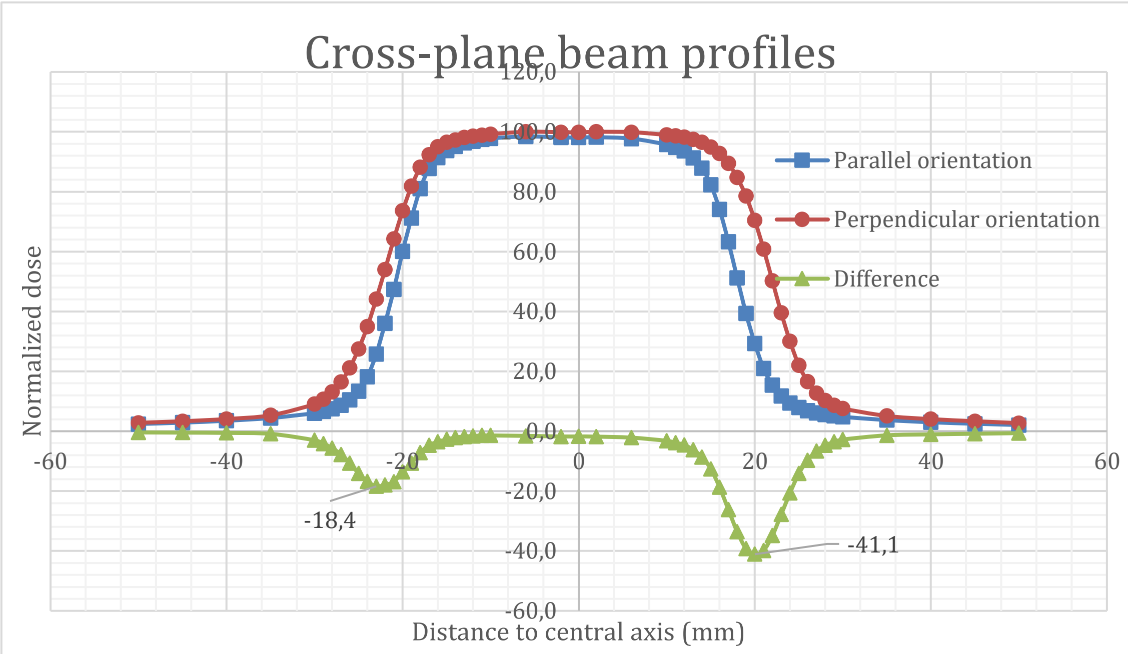

Figure A6 Cross-plane beam profiles for parallel and perpendicular orientation of a PTW 31010 semi-flex ionisation chamber in a 4 cm × 4 cm photon beam field size produced by a Siemens Oncor LINAC.

The percentage difference between the cross-plane beam profiles at distances -23 mm and +20 mm in the penumbra, shown in Figure A6, obtained using a PTW 31010 semi-flex ionisation chamber oriented parallel to the photon beam and perpendicular to the photon beam was found to be -18.4% and -41.1%, respectively. Figure A6 shows that more current was collected when the chamber was orientated perpendicular to the beam than when it was orientated parallel to the beam along the cross-plane.

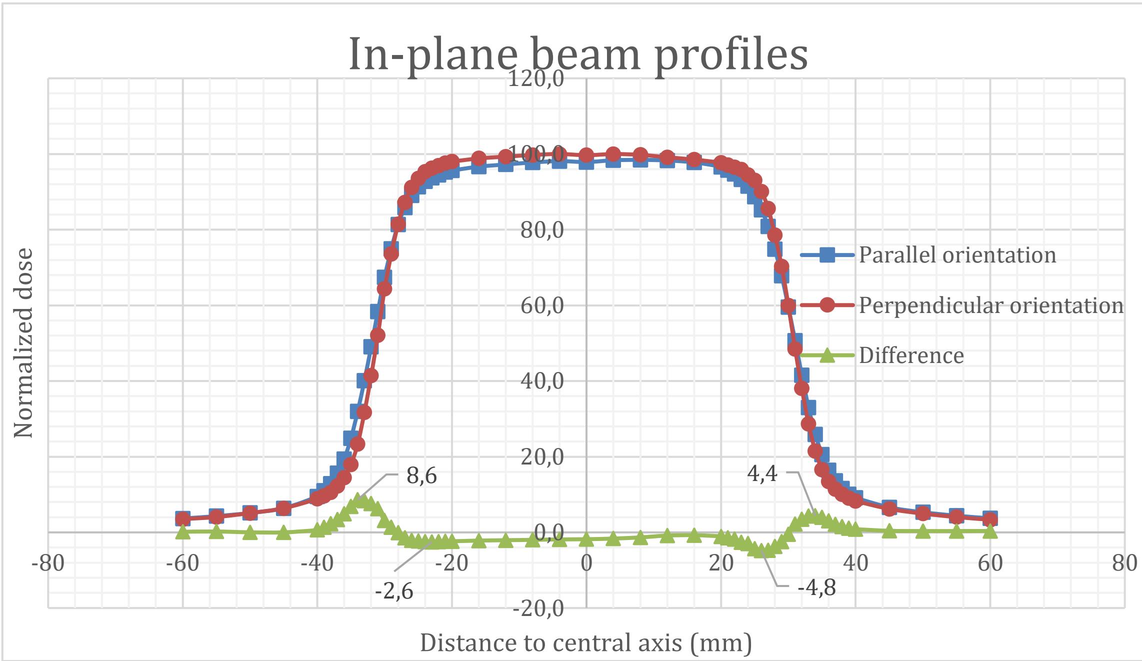

Figure A7 In-plane beam profiles for parallel and perpendicular orientation of a PTW 31010 semi-flex ionisation chamber in a 6 cm × 6 cm photon beam field size produced by a Siemens Oncor LINAC.

The percentage difference between the in-plane beam profiles at distances -23 mm and +26 mm in the central region, shown in Figure A7, obtained using a PTW 31010 semi-flex ionisation chamber oriented parallel to the photon beam and perpendicular to the photon beam was found to be -2.6% and -4.8%, respectively. The percentage difference between the in-plane beam profiles at distances -34 mm and +34 mm in the penumbra was found to be 8.6% and 4.4%, respectively. Figure A7 shows that more current was collected in the central region when the chamber was orientated perpendicular to the beam than when is orientated parallel to the beam. It also shows that more current was collected in the penumbra region when the chamber was orientated parallel to the beam than when it was orientated perpendicular to the beam.

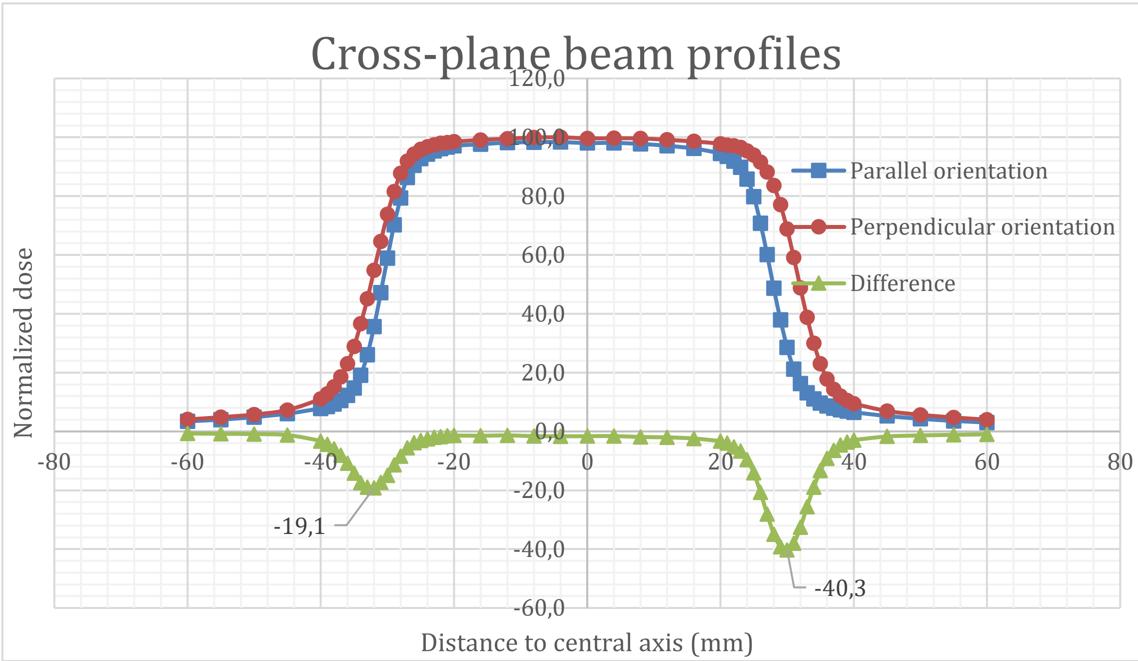

Figure A8 Cross-plane beam profiles for parallel and perpendicular orientation of a PTW 31010 semi-flex ionisation chamber in a 6 cm × 6 cm photon beam field size produced by a Siemens Oncor LINAC.

The percentage difference between the cross-plane beam profiles at distances -32 mm and +30 mm in the penumbra, shown in Figure A8, obtained using a PTW 31010 semi-flex ionisation chamber oriented parallel to the photon beam and perpendicular to the photon beam was found to be -19.1% and -40.3%, respectively. Figure A8 shows that more current was collected when the chamber was orientated perpendicular to the beam than when it was orientated parallel to the beam along the cross-plane.

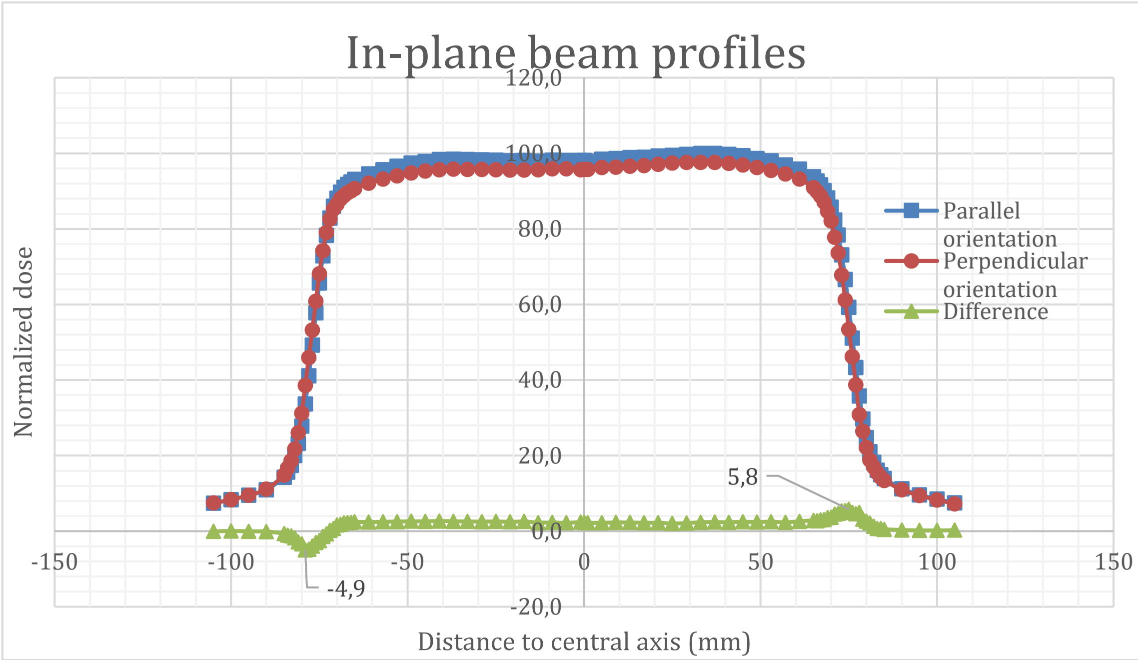

Figure A9 In-plane beam profiles for parallel and perpendicular orientation of a PTW 31010 semi-flex ionisation chamber in a 15 cm × 15 cm photon beam field size produced by a Siemens Oncor LINAC.

The percentage difference between the in-plane beam profiles at distances -79 mm and +75 mm in the penumbra, shown in Figure A9, obtained using a PTW 31010 semi-flex ionisation chamber oriented parallel to the photon beam and perpendicular to the photon beam was found to be -4.9% and +6.8%, respectively. Figure A9 shows that more current was collected in the central region when the chamber was orientated parallel to the beam than when it was orientated perpendicular to the beam.

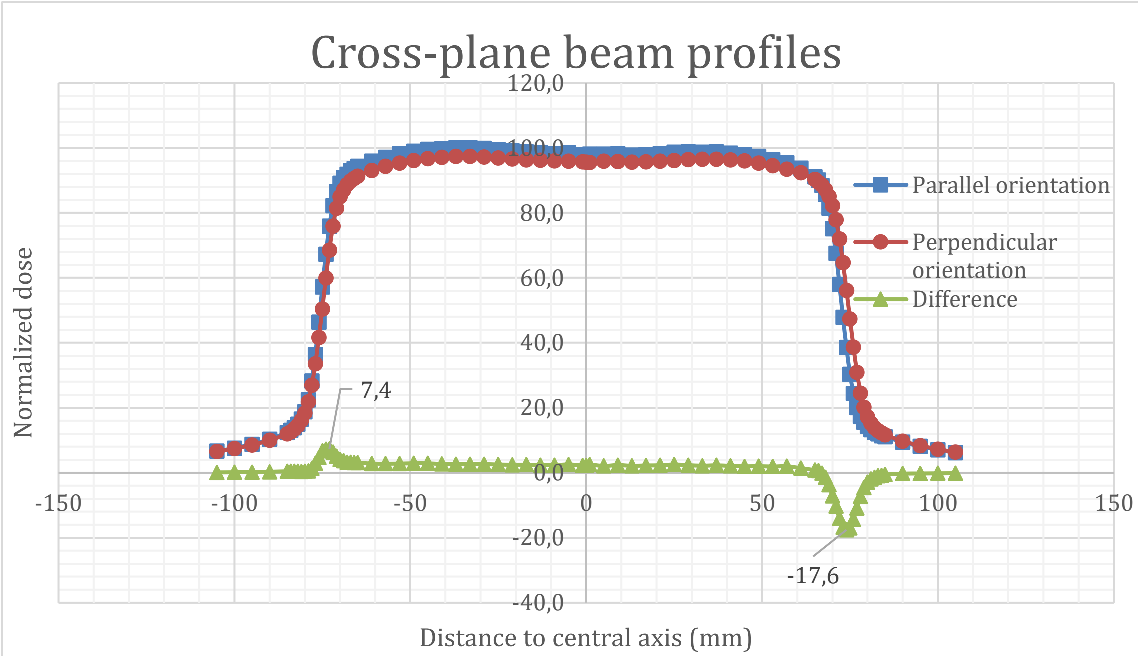

Figure A10 Cross-plane beam profiles for parallel and perpendicular orientation of a PTW 31010 semi-flex ionisation chamber in a 15 cm × 15 cm photon beam field size produced by a Siemens Oncor LINAC.

The percentage difference between the cross-plane beam profiles at distances -73 mm and +74 mm in the penumbra, shown in Figure A10, obtained using a PTW 31010 semi-flex ionisation chamber oriented parallel to the photon beam and perpendicular to the photon beam was found to be +7.4% and -17.6%, respectively. Figure A10 shows that more current was collected in the central region when the chamber was orientated parallel to the beam than when it was orientated perpendicular to the beam.

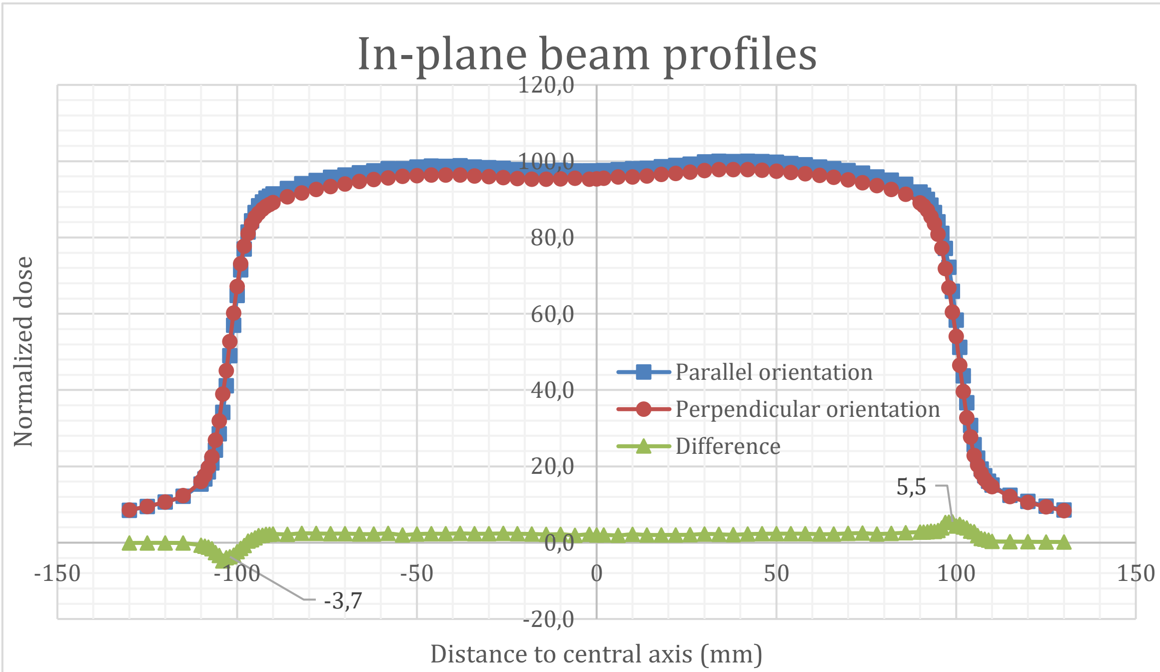

Figure A11 In-plane beam profiles for parallel and perpendicular orientation of a PTW 31010 semi-flex ionisation chamber in a 20 cm × 20 cm photon beam field size produced by a Siemens Oncor LINAC.

The percentage difference between the in-plane beam profiles at distances -102 mm and +99 mm in the penumbra, shown in Figure A11, obtained using a PTW 31010 semi-flex ionisation chamber oriented parallel to the photon beam and perpendicular to the photon beam was found to be -3.7% and +5.5%, respectively. Figure A11 shows that more current was collected in the central region when the chamber was orientated parallel to the beam than when it was orientated perpendicular to the beam.

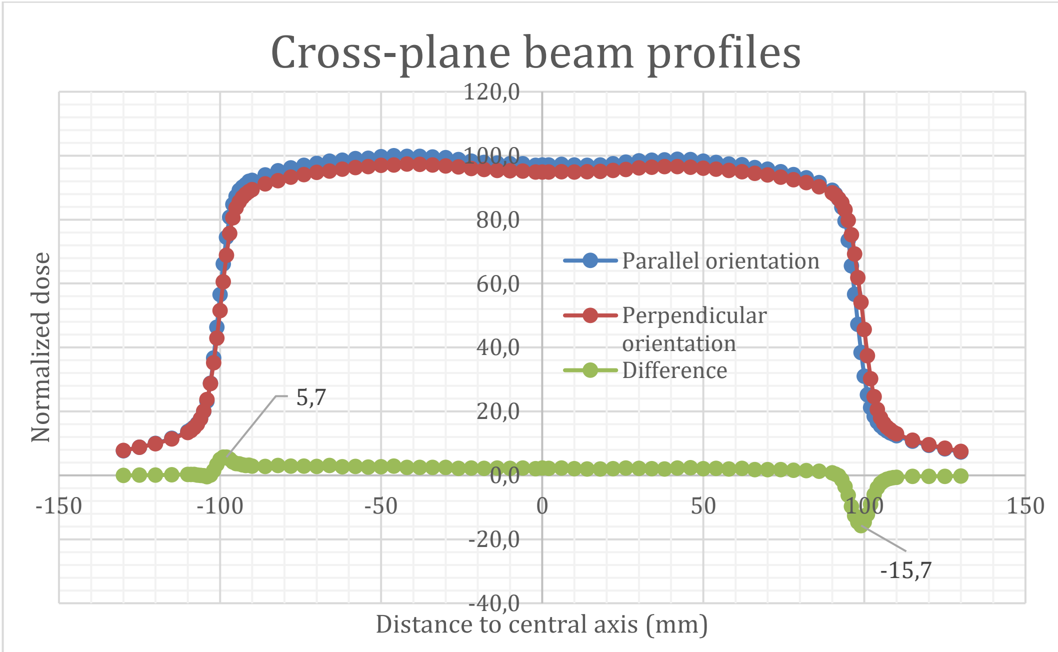

Figure A12 Cross-plane beam profiles for parallel and perpendicular orientation of a PTW 31010 semi-flex ionisation chamber in a 20 cm × 20 cm photon beam field size produced by a Siemens Oncor LINAC.

The percentage difference between the cross-plane beam profiles at distances -98 mm and +99 mm in the penumbra, shown in Figure A12, obtained using a PTW 31010 semi-flex ionisation chamber oriented parallel to the photon beam and perpendicular to the photon beam was found to be +5.7% and -15.7%, respectively. Figure A12 shows that more current was collected in the central region when the chamber was orientated parallel to the beam than when it was orientated perpendicular to the beam.

Beam profiles obtained using a PTW 60019 synthetic single-crystal diamond detector irradiated by a photon beam produced a Siemens Oncor LINAC

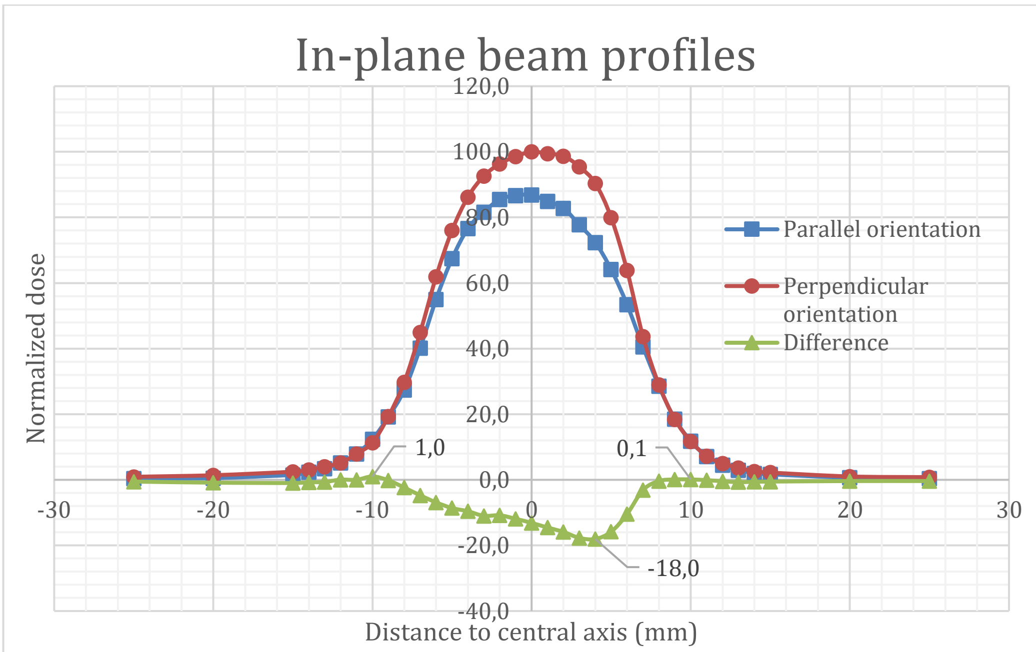

Figure B1 In-plane beam profiles for parallel and perpendicular orientation of a PTW 60019 synthetic single-crystal diamond detector in a 1 cm × 1 cm photon beam field size produced by a Siemens Oncor LINAC.

The percentage difference between the in-plane beam profiles at distances +4 mm in the central region, shown in Figure B1, obtained using a PTW 60019 synthetic single-crystal diamond detector oriented parallel to the photon beam and perpendicular to the photon beam was found to be -18.0%. The percentage difference between the in-plane beam profiles at distances -10 mm and +10 mm in the penumbra was found to be 1.0% and 0.1%, respectively. Figure B1 shows that more current was collected in the central region when the chamber was orientated perpendicular to the beam than when it was orientated parallel to the beam. It also shows that a little more current was collected in the penumbra region when the chamber was orientated parallel to the beam than when it was orientated perpendicular to the beam.

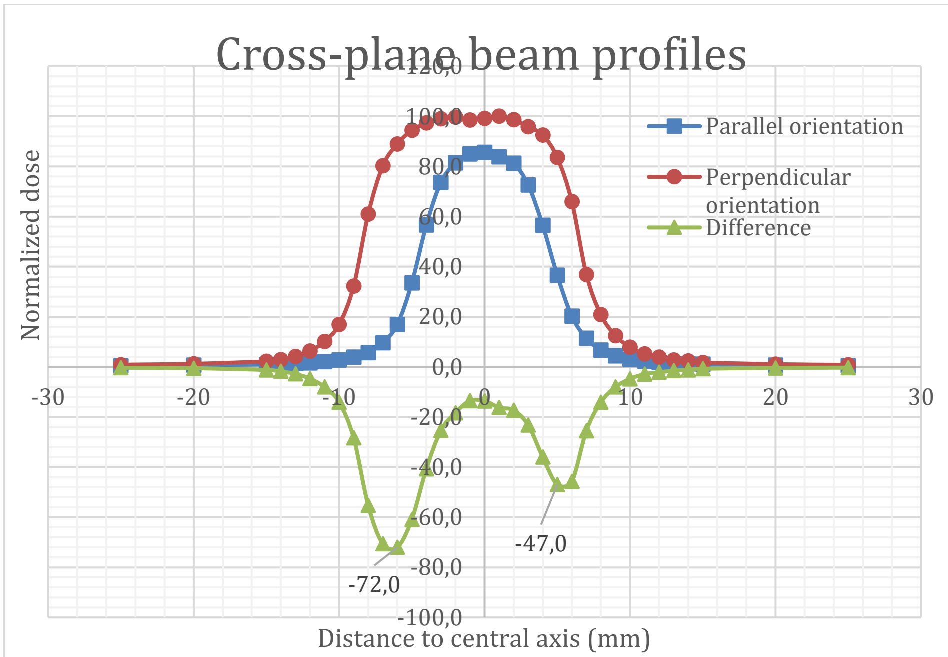

Figure B2 Cross-plane beam profiles for parallel and perpendicular orientation of a PTW 60019 synthetic single-crystal diamond detector in a 1 cm × 1 cm photon beam field size produced by a Siemens Oncor LINAC.

The percentage difference between the cross-plane beam profiles at distances -6 mm and +5 mm in the penumbra, shown in Figure B2, obtained using a PTW 60019 synthetic single-crystal diamond detector oriented parallel to the photon beam and perpendicular to the photon beam was found to be -72.0% and -47.0%, respectively. Figure B2 shows that more current was collected when the detector was orientated perpendicular to the beam than when it was orientated parallel to the beam.

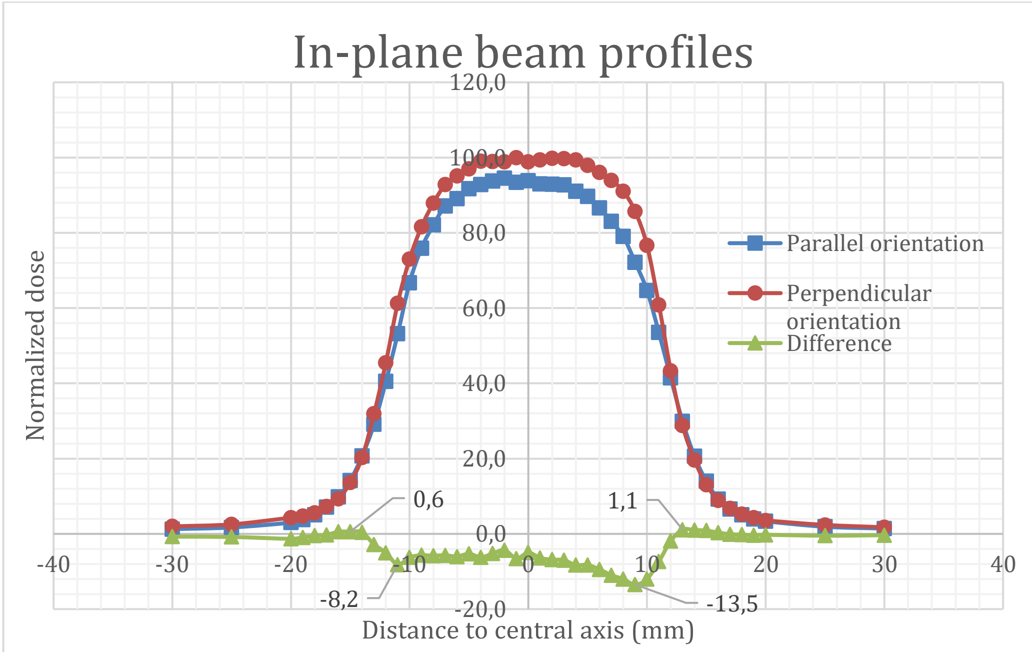

Figure B3 In-plane beam profiles for parallel and perpendicular orientation of a PTW 60019 synthetic single-crystal diamond detector in a 2 cm × 2 cm photon beam field size produced by a Siemens Oncor LINAC.

The percentage difference between the in-plane beam profiles at distances -11 mm and +9 mm in the central region, shown in Figure B3, obtained using a PTW 60019 synthetic single-crystal diamond detector oriented parallel to the photon beam and perpendicular to the photon beam was found to be -8.2% and -13.5%, respectively. The percentage difference between the in-plane beam profiles at distances -15 mm and +13 mm in the penumbra was found to be 0.6% and 1.1%, respectively. Figure B3 shows that more current was collected in the central region when the detector was orientated perpendicular to the beam than when is orientated parallel to the beam. It also shows that a little more current was collected in the penumbra region when the detector was orientated parallel to the beam than when it was orientated perpendicular to the beam.

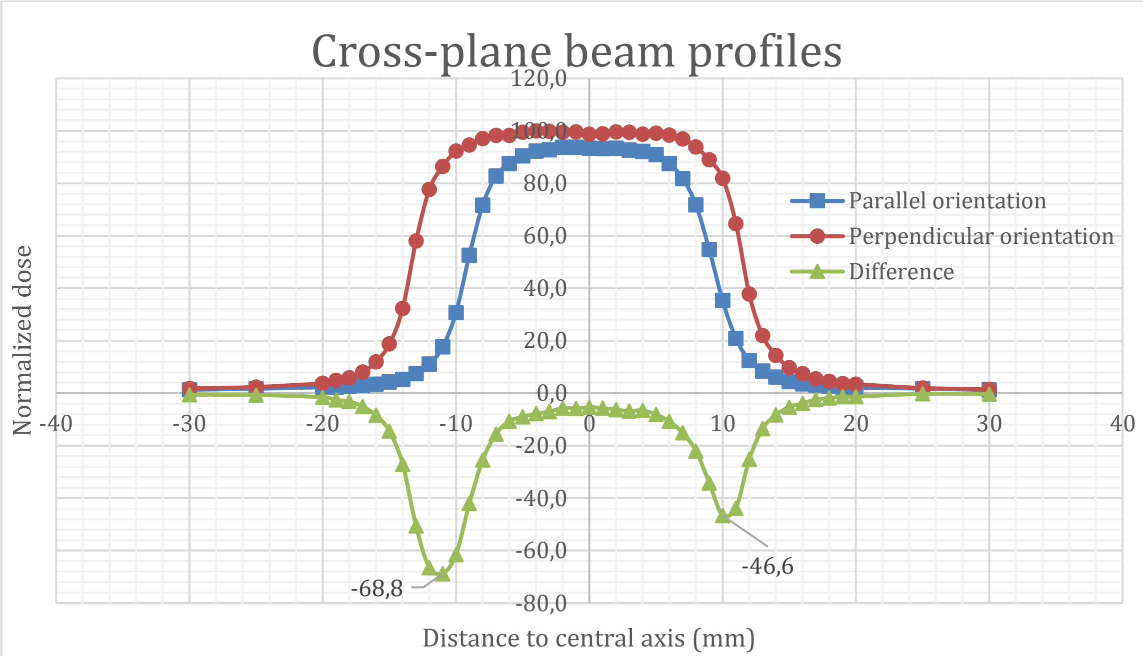

Figure B4 Cross-plane beam profiles for parallel and perpendicular orientation of a PTW 60019 synthetic single-crystal diamond detector in a 2 cm × 2 cm photon beam field size produced by a Siemens Oncor LINAC.

The percentage difference between the cross-plane beam profiles at distances -11 mm and +10 mm in the penumbra, shown in Figure B4, obtained using a PTW 60019 synthetic single-crystal diamond detector oriented parallel to the photon beam and perpendicular to the photon beam was found to be -68.8% and -46.6%, respectively. Figure B4 shows that more current was collected when the detector was orientated perpendicular to the beam than when it was orientated parallel to the beam.

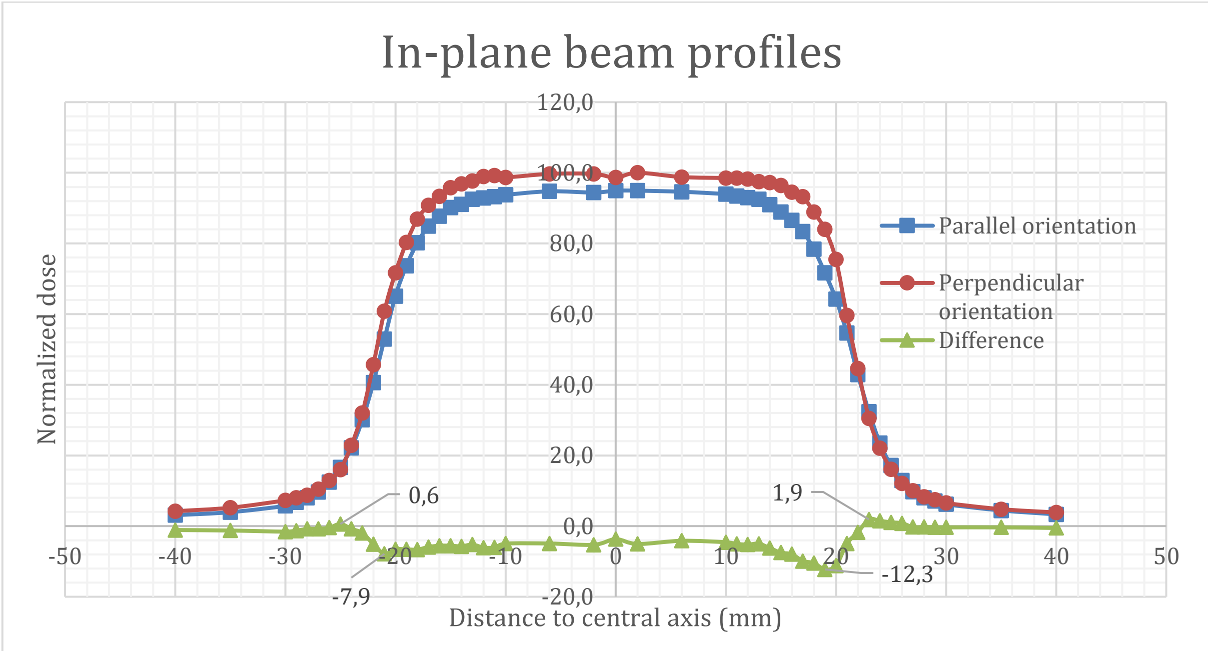

Figure B5 In-plane beam profiles for parallel and perpendicular orientation of a PTW 60019 synthetic single-crystal diamond detector in a 4 cm × 4 cm photon beam field size produced by a Siemens Oncor LINAC.

The percentage difference between the in-plane beam profiles at distances -21 mm and +19 mm in the central region, shown in Figure B5, obtained using a PTW 60019 synthetic single-crystal diamond detector oriented parallel to the photon beam and perpendicular to the photon beam was found to be -7.9% and -12.3%, respectively. The percentage difference between the in-plane beam profiles at distances -25 mm and +23 mm in the penumbra was found to be 0.6% and 1.9%, respectively. Figure B5 shows that more current was collected in the central region when the detector was orientated perpendicular to the beam than when is orientated parallel to the beam. It also shows that a little more current was collected in the penumbra region when the detector was orientated parallel to the beam than when it was orientated perpendicular to the beam.

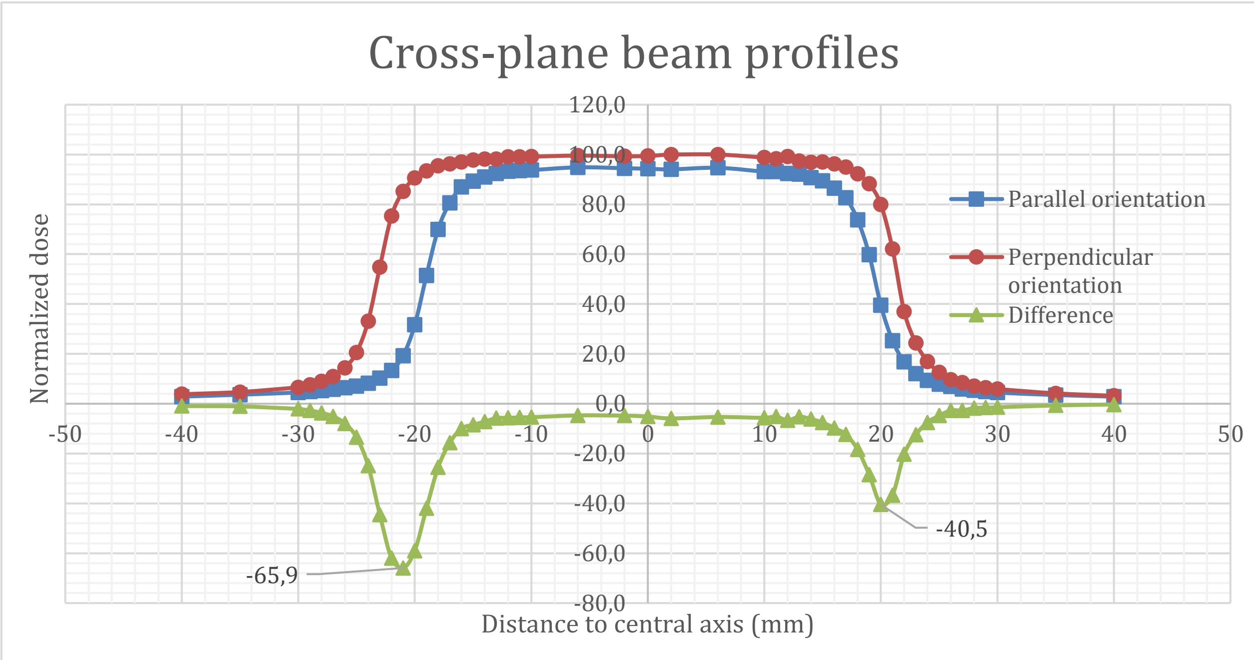

Figure B6 Cross-plane beam profiles for parallel and perpendicular orientation of a PTW 60019 synthetic single-crystal diamond detector in a 4 cm × 4 cm photon beam field size produced by a Siemens Oncor LINAC.

The percentage difference between the cross-plane beam profiles at distances -21 mm and +20 mm in the penumbra, shown in Figure B6, obtained using a PTW 60019 synthetic single-crystal diamond detector oriented parallel to the photon beam and perpendicular to the photon beam was found to be -65.9% and -40.5%, respectively. Figure B6 shows that more current was collected when the detector was orientated perpendicular to the beam than when it was orientated parallel to the beam.

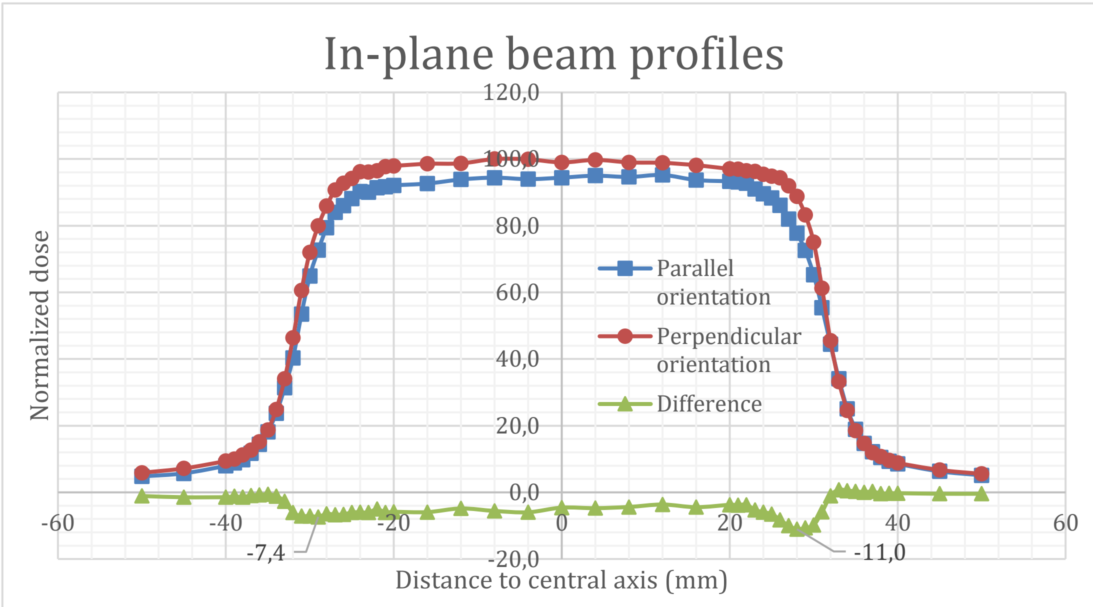

Figure B7 In-plane beam profiles for parallel and perpendicular orientation of a PTW 60019 synthetic single-crystal diamond detector in a 6 cm × 6 cm photon beam field size produced by a Siemens Oncor LINAC.

The percentage difference between the in-plane beam profiles at distances -29 mm and +28 mm in the penumbra, shown in Figure B7, obtained using a PTW 60019 synthetic single-crystal diamond detector oriented parallel to the photon beam and perpendicular to the photon beam was found to be -7.4% and -11.0%, respectively. Figure B7 shows that more current was collected in the central region when the chamber was orientated perpendicular to the beam than when it was orientated parallel to the beam.

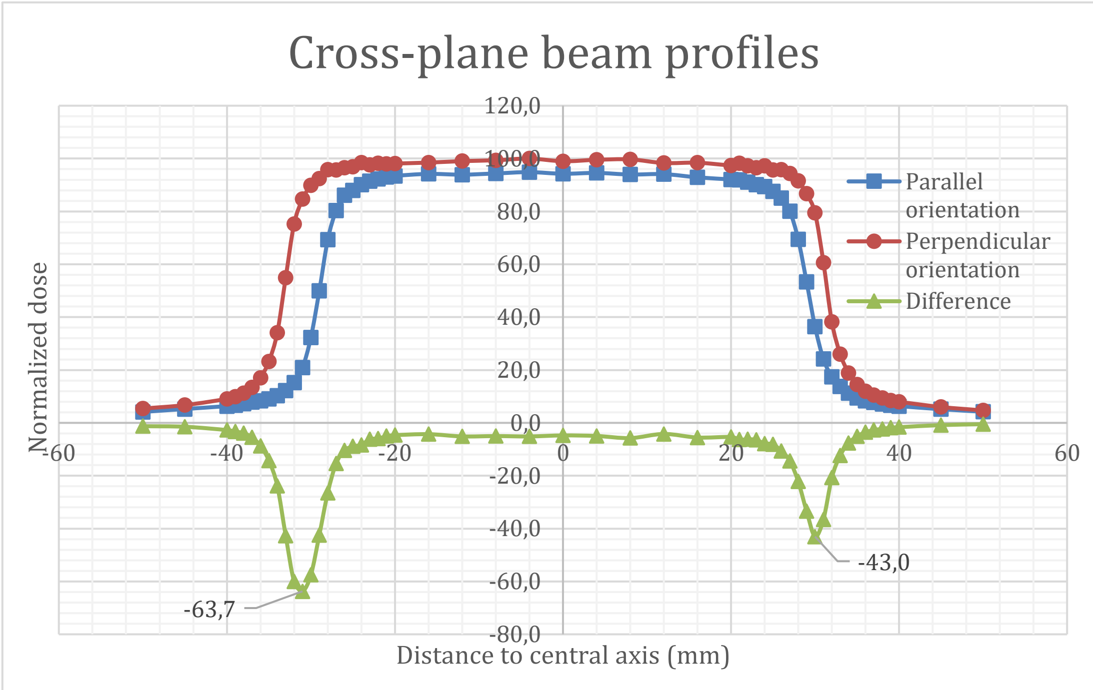

Figure B8 Cross-plane beam profiles for parallel and perpendicular orientation of a PTW 60019 synthetic single-crystal diamond detector in a 6 cm × 6 cm photon beam field size produced by a Siemens Oncor LINAC.

The percentage difference between the cross-plane beam profiles at distances -31 mm and +30 mm in the penumbra, shown in Figure B8, obtained using a PTW 60019 synthetic single-crystal diamond detector oriented parallel to the photon beam and perpendicular to the photon beam was found to be -63.7% and -43.0%, respectively. Figure B8 shows that more current was collected when the detector was orientated perpendicular to the beam than when it was orientated parallel to the beam.

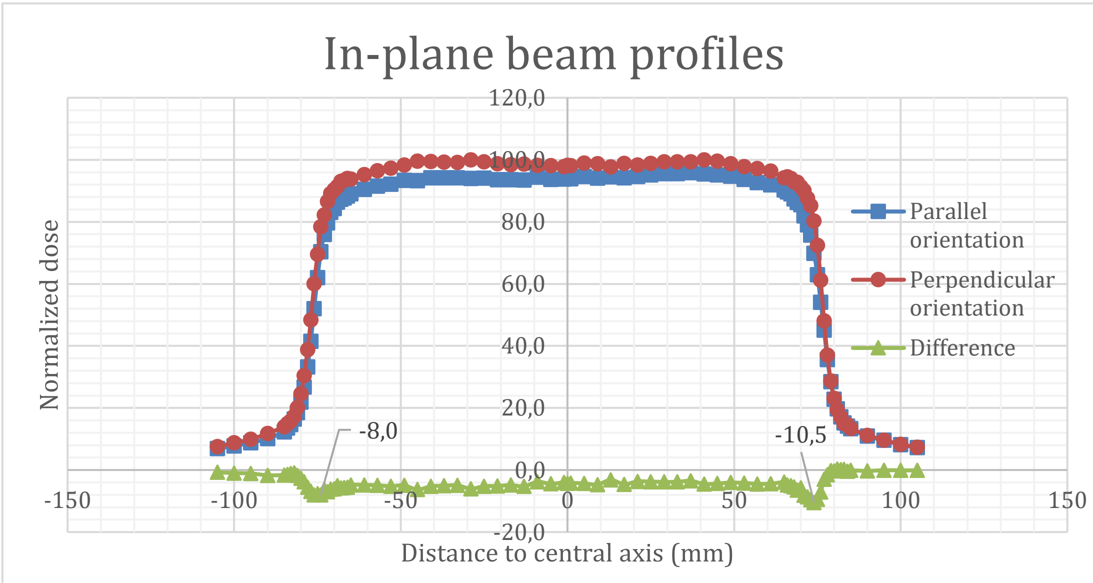

Figure B9 In-plane beam profiles for parallel and perpendicular orientation of a PTW 60019 synthetic single-crystal diamond detector in a 15 cm × 15 cm photon beam field size produced by a Siemens Oncor LINAC.

The percentage difference between the in-plane beam profiles at distances -74 mm and +74 mm in the penumbra, shown in Figure B9, obtained using a PTW 60019 synthetic single-crystal diamond detector oriented parallel to the photon beam and perpendicular to the photon beam was found to be -8.0% and -10.5%, respectively. Figure B9 shows that more current was collected in the central region when the chamber was orientated perpendicular to the beam than when it was orientated parallel to the beam.

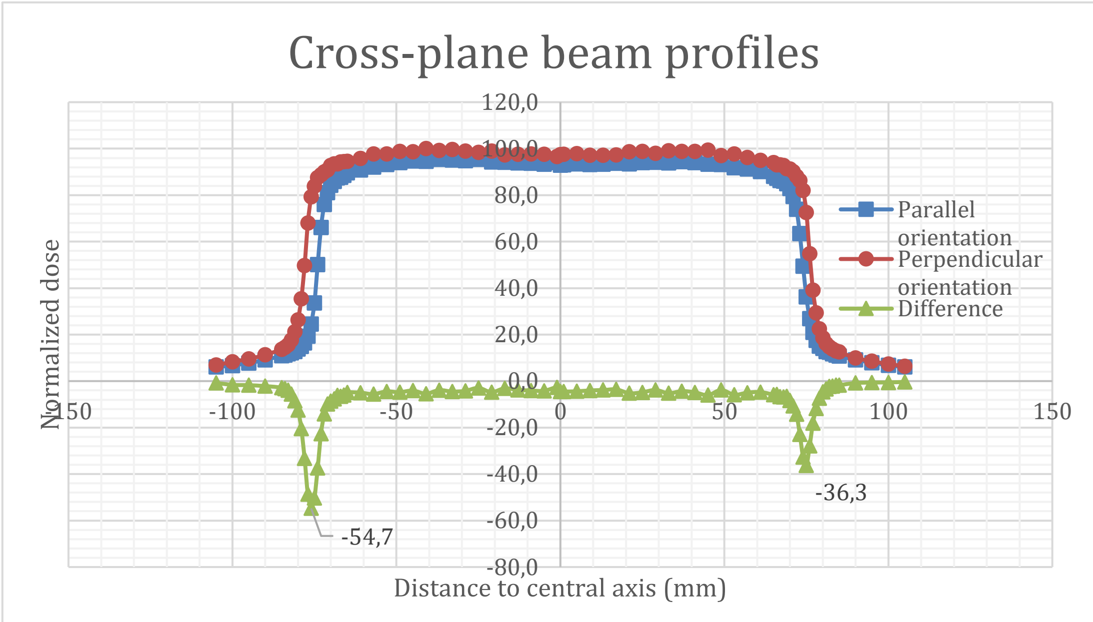

Figure B10 Cross-plane beam profiles for parallel and perpendicular orientation of a PTW 60019 synthetic single-crystal diamond detector in a 15 cm × 15 cm photon beam field size produced by a Siemens Oncor LINAC.

The percentage difference between the cross-plane beam profiles at distances -76 mm and +75 mm in the penumbra, shown in Figure B10, obtained using a PTW 60019 synthetic single-crystal diamond detector oriented parallel to the photon beam and perpendicular to the photon beam was found to be -54.7% and -36.3%, respectively. Figure B10 shows that more current was collected when the detector was orientated perpendicular to the beam than when it was orientated parallel to the beam.

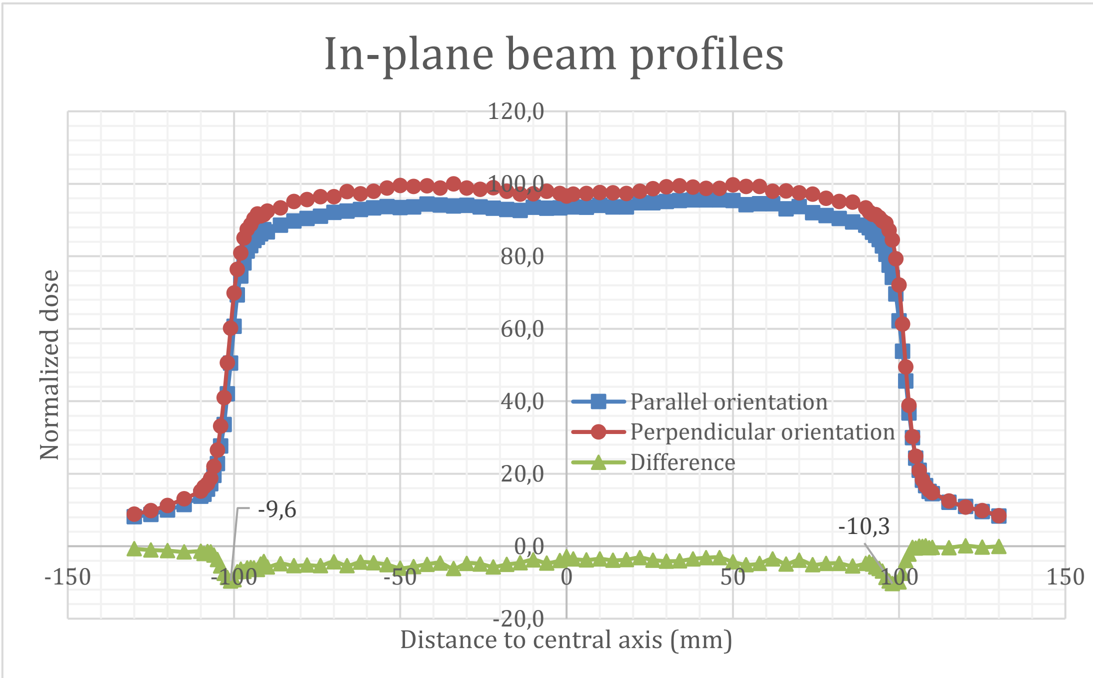

Figure B11 In-plane beam profiles for parallel and perpendicular orientation of a PTW 60019 synthetic single-crystal diamond detector in a 20 cm × 20 cm photon beam field size produced by a Siemens Oncor LINAC.

The percentage difference between the in-plane beam profiles at distances -101 mm and +98 mm in the penumbra, shown in Figure B11, obtained using a PTW 60019 synthetic single-crystal diamond detector oriented parallel to the photon beam and perpendicular to the photon beam was found to be -9.6% and -10.3%, respectively. Figure B11 shows that more current was collected in the central region when the chamber was orientated perpendicular to the beam than when it was orientated parallel to the beam.

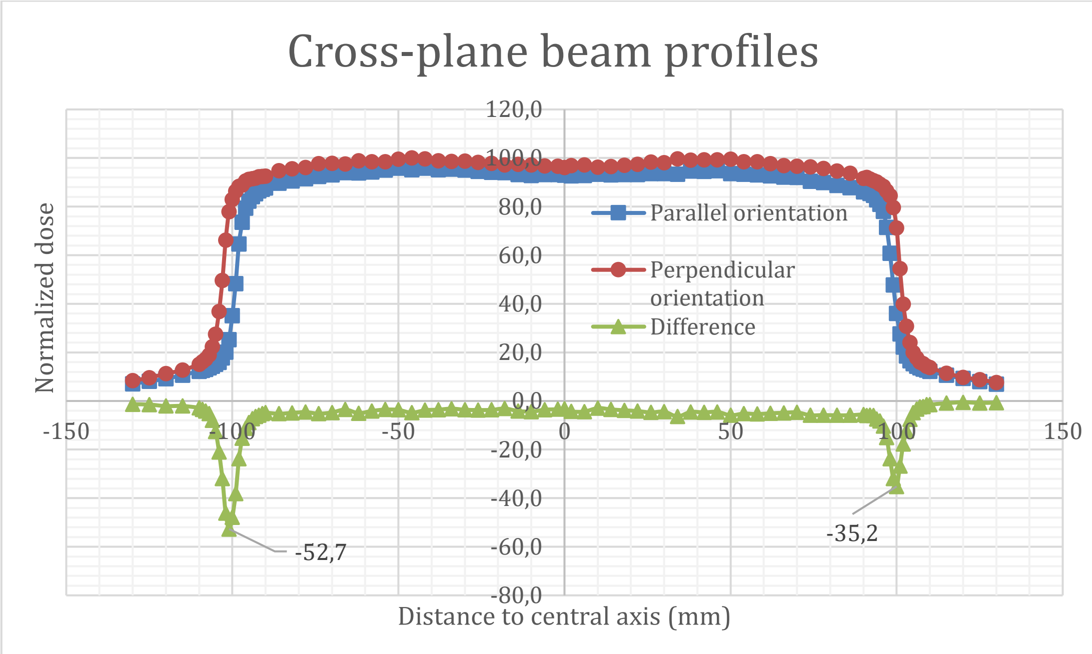

Figure B12 Cross-plane beam profiles for parallel and perpendicular orientation of a PTW 60019 synthetic single-crystal diamond detector in a 20 cm × 20 cm photon beam field size produced by a Siemens Oncor LINAC.

The percentage difference between the cross-plane beam profiles at distances -101 mm and +100 mm in the penumbra, shown in Figure B12, obtained using a PTW 60019 synthetic single-crystal diamond detector oriented parallel to the photon beam and perpendicular to the photon beam was found to be -52.7% and -35.2%, respectively. Figure B12 shows that more current was collected when the detector was orientated perpendicular to the beam than when it was orientated parallel to the beam.

Beam profiles obtained using a PTW 60019 synthetic single-crystal diamond detector irradiated by a photon beam produced an Elekta Versa HD LINAC.

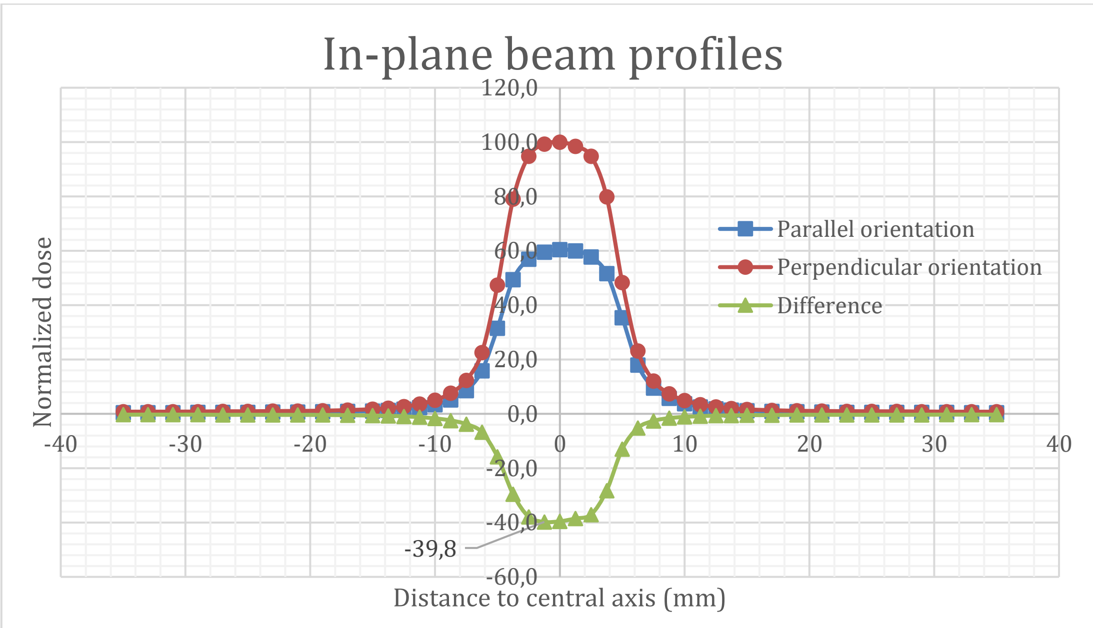

Figure C1 In-plane beam profiles for parallel and perpendicular orientation of a PTW 60019 synthetic single-crystal diamond detector in a 1 cm × 1 cm photon beam field size produced by an Elekta Versa HD LINAC.

The percentage difference between the in-plane beam profiles at distances -1.25 mm in the central region, shown in Figure C1, obtained using a PTW 60019 synthetic single-crystal diamond oriented parallel to the photon beam and perpendicular to the photon beam was found to be -39.8%. Figure C1 shows that more current was collected when the detector was orientated perpendicular to the beam than when it was orientated parallel to the beam.

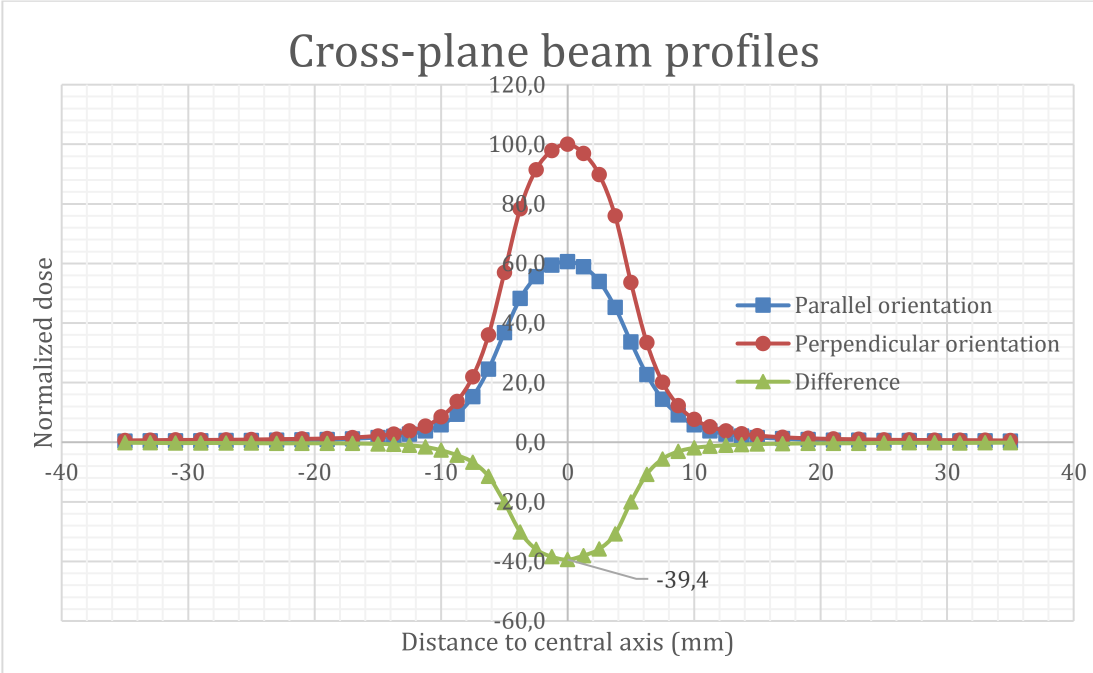

Figure C2 Cross-plane beam profiles for parallel and perpendicular orientation of a PTW 60019 synthetic single-crystal diamond detector in a 1 cm × 1 cm photon beam field size produced by an Elekta Versa HD LINAC.

The percentage difference between the in-plane beam profiles at the CAX, shown in Figure C2, obtained using a PTW 60019 synthetic single-crystal diamond oriented parallel to the photon beam and perpendicular to the photon beam was found to be -39.4%. Figure C2 shows that more current was collected when the detector was orientated perpendicular to the beam than when it was orientated parallel to the beam.

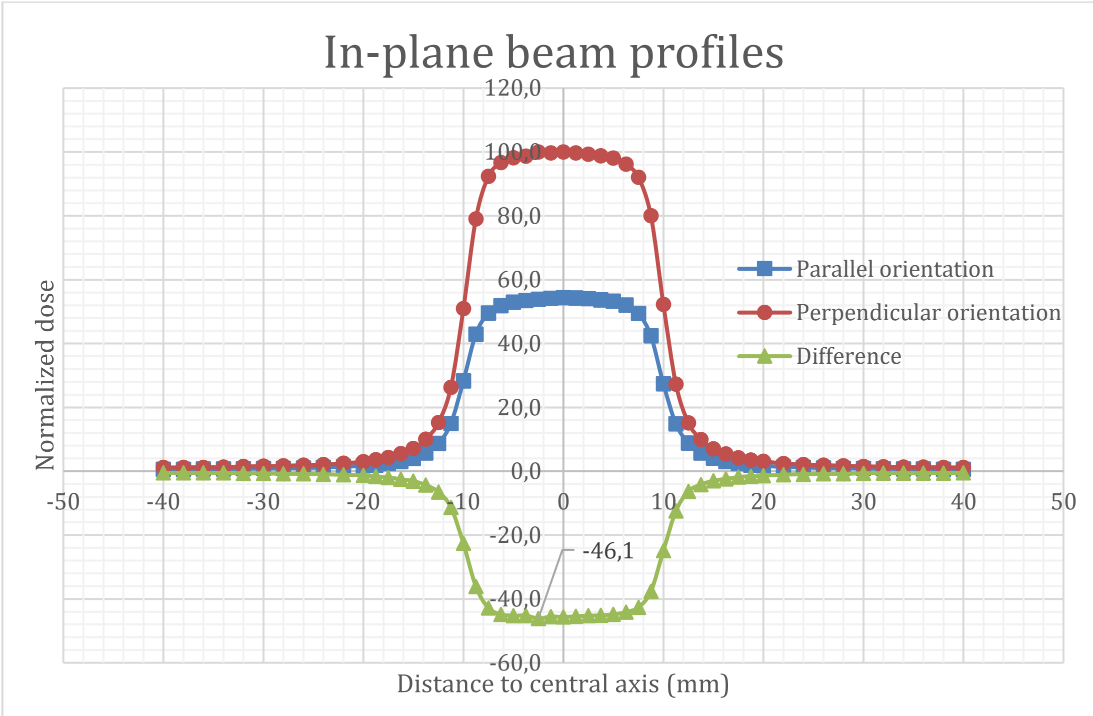

Figure C3 In-plane beam profiles for parallel and perpendicular orientation of a PTW 60019 synthetic single-crystal diamond detector in a 2 cm × 2 cm photon beam field size produced by an Elekta Versa HD LINAC.

The percentage difference between the in-plane beam profiles at distances -2.5 mm in the central region, shown in Figure C3, obtained using a PTW 60019 synthetic single-crystal diamond oriented parallel to the photon beam and perpendicular to the photon beam was found to be -46.1%. Figure C3 shows that more current was collected when the detector was orientated perpendicular to the beam than when it was orientated parallel to the beam.

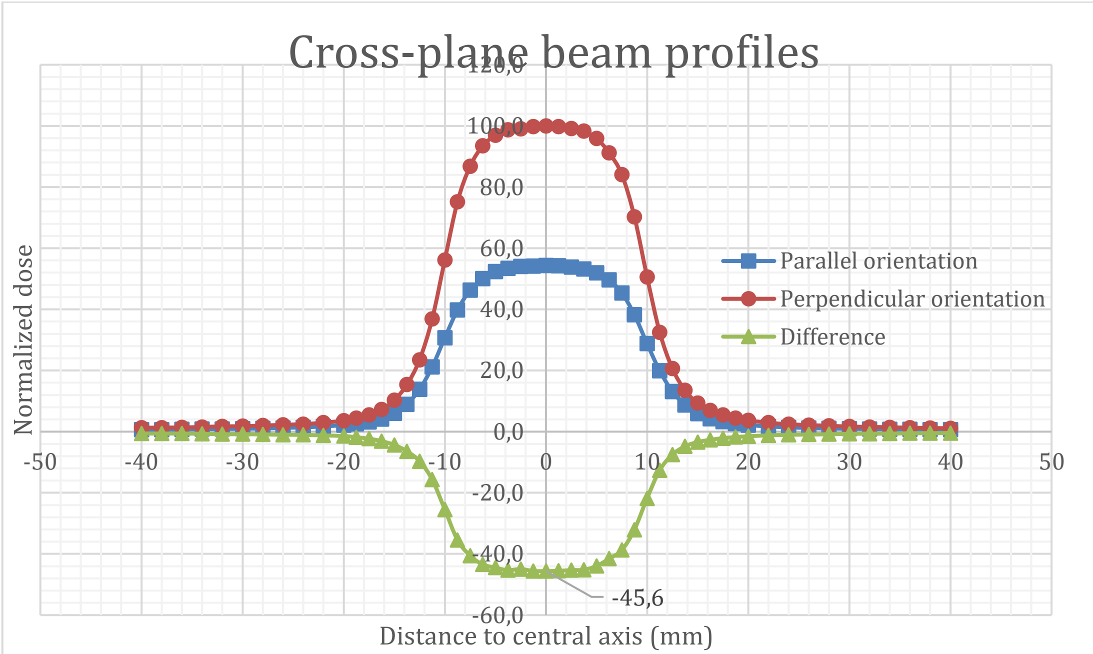

Figure C4 Cross-plane beam profiles for parallel and perpendicular orientation of a PTW 60019 synthetic single-crystal diamond detector in a 2 cm × 2 cm photon beam field size produced by an Elekta Versa HD LINAC.

The percentage difference between the in-plane beam profiles at the CAX, shown in Figure C4, obtained using a PTW 60019 synthetic single-crystal diamond oriented parallel to the photon beam and perpendicular to the photon beam was found to be -45.6%. Figure C4 shows that more current was collected when the detector was orientated perpendicular to the beam than when it was orientated parallel to the beam.

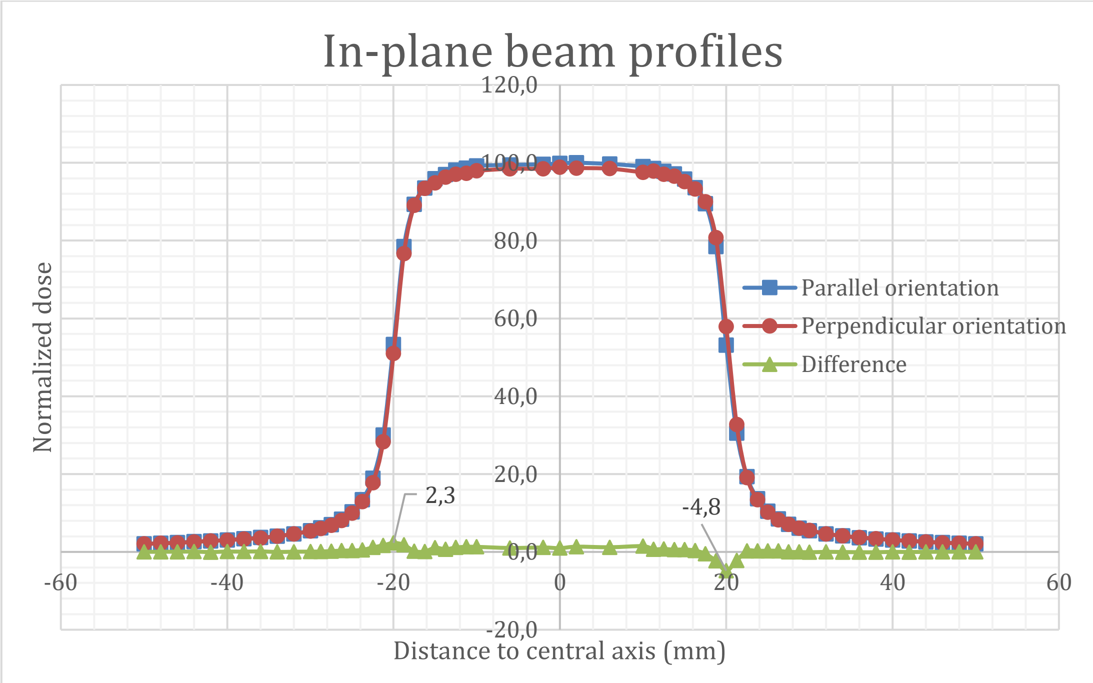

Figure C5 In-plane beam profiles for parallel and perpendicular orientation of a PTW 60019 synthetic single-crystal diamond detector in a 4 cm × 4 cm photon beam field size produced by an Elekta Versa HD LINAC.

The percentage difference between the in-plane beam profiles at distances -20 mm and +20 mm in the penumbra, shown in Figure C5, obtained using a PTW 60019 synthetic single-crystal diamond detector oriented parallel to the photon beam and perpendicular to the photon beam was found to be +2.3% and -4.8%, respectively. Figure C5 shows that more current was collected in the central region when the detector was orientated parallel to the beam than when it was orientated perpendicular to the beam.

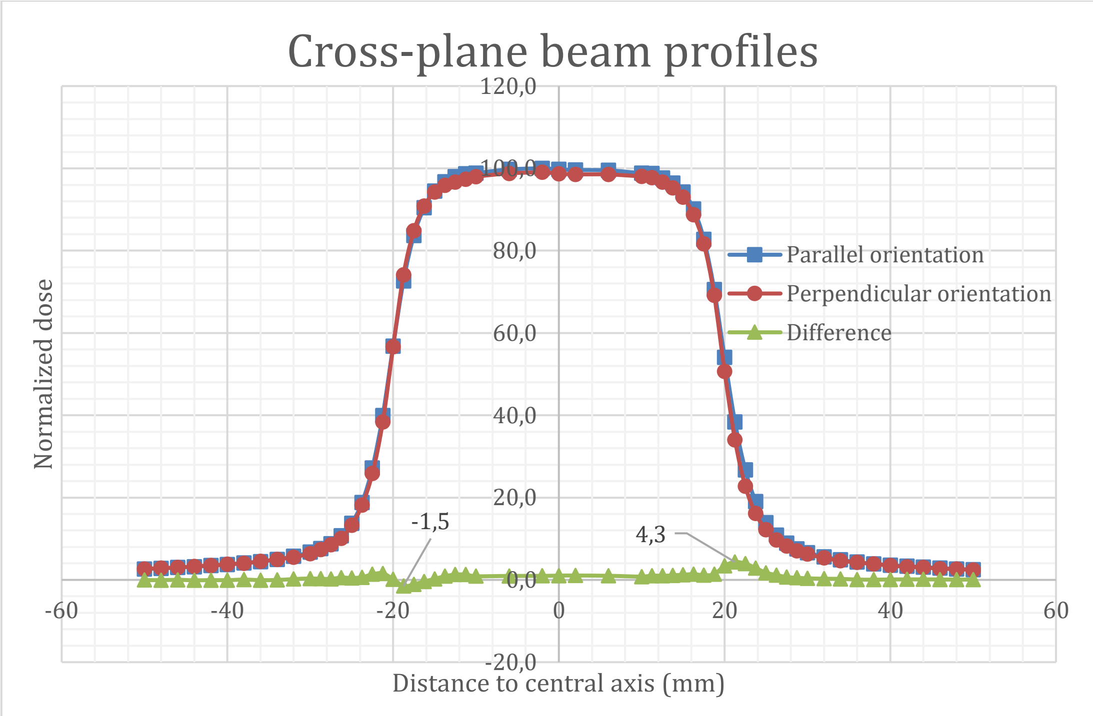

Figure C6 Cross-plane beam profiles for parallel and perpendicular orientation of a PTW 60019 synthetic single-crystal diamond detector in a 4 cm × 4 cm photon beam field size produced by an Elekta Versa HD LINAC.

The percentage difference between the in-plane beam profiles at distances -18.75 mm and +21.25 mm in the penumbra, shown in Figure C6, obtained using a PTW 60019 synthetic single-crystal diamond detector oriented parallel to the photon beam and perpendicular to the photon beam was found to be -1.5% and +4.3%, respectively. Figure C6 shows that more current was collected in the central region when the detector was orientated parallel to the beam than when it was orientated perpendicular to the beam.

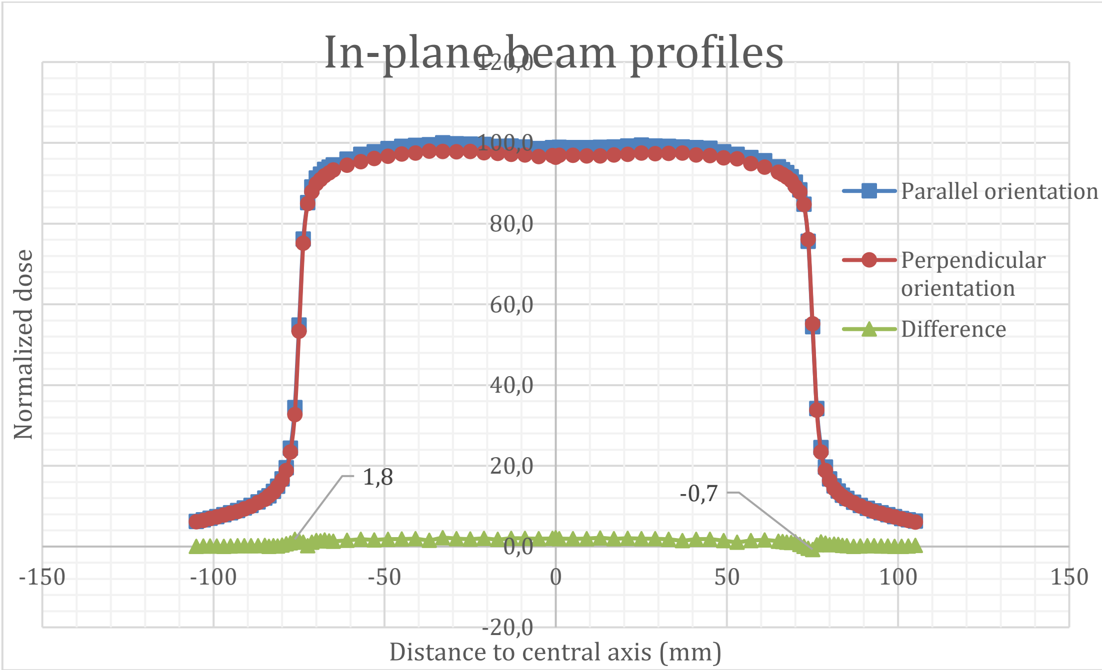

Figure C7 In-plane beam profiles for parallel and perpendicular orientation of a PTW 60019 synthetic single-crystal diamond detector in a 15 cm × 15 cm photon beam field size produced by an Elekta Versa HD LINAC.

The percentage difference between the in-plane beam profiles at distances -76.25 mm and +75 mm in the penumbra, shown in Figure C7, obtained using a PTW 60019 synthetic single-crystal diamond detector oriented parallel to the photon beam and perpendicular to the photon beam was found to be +1.8% and -0.7%, respectively. Figure C7 shows that more current was collected in the central region when the detector was orientated parallel to the beam than when it was orientated perpendicular to the beam.

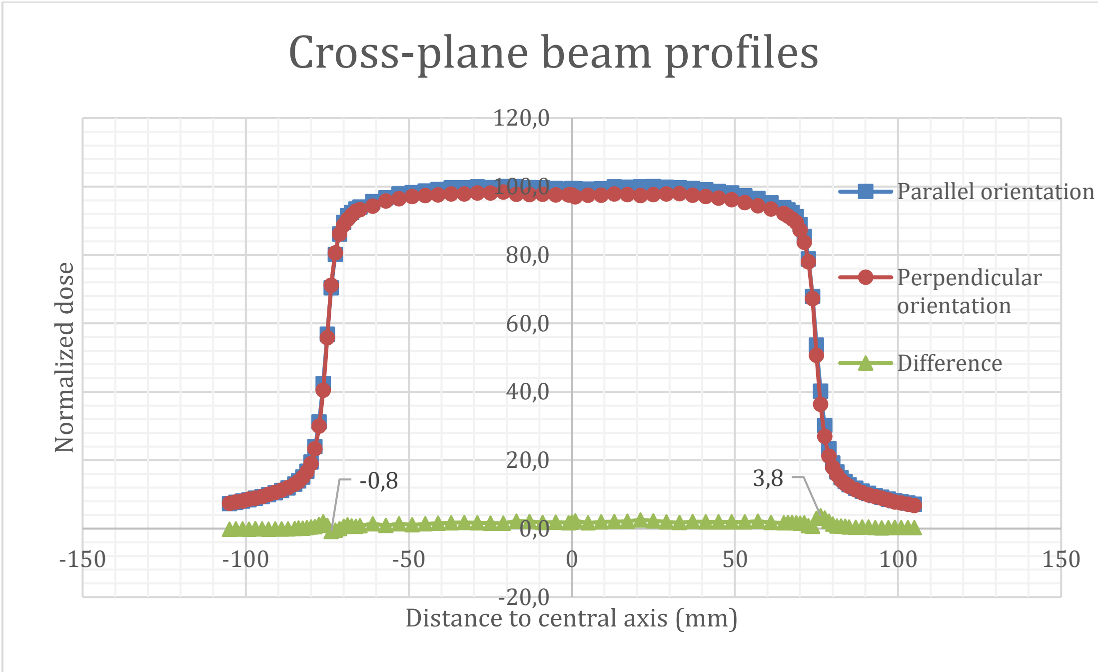

Figure C8 Cross-plane beam profiles for parallel and perpendicular orientation of a PTW 60019 synthetic single-crystal diamond detector in a 15 cm × 15 cm photon beam field size produced by an Elekta Versa HD LINAC.

The percentage difference between the in-plane beam profiles at distances -73.75 mm and +76.25 mm in the penumbra, shown in Figure C8, obtained using a PTW 60019 synthetic single-crystal diamond detector oriented parallel to the photon beam and perpendicular to the photon beam was found to be -0.8% and +3.8%, respectively. Figure C8 shows that more current was collected in the central region when the detector was orientated parallel to the beam than when it was orientated perpendicular to the beam.